

https://dspace.org/

Structuring light to improve laser brightness

Scholes, Stirling

2020
https://hdl.handle.net/10539/30979

Downloaded from a DSpace repository. https://dspace.org/

STRUCTURING LIGHT TO IMPROVE LASER BRIGHTNESS



Stirling Scholes

Faculty of Science

University of the Witwatersrand, Johannesburg

This dissertation is submitted for the degree of

Master of Science

School of Physics

November 2020

Declaration

I declare that this dissertation is my own, unaided work. It is being submitted for the Degree of Master of Science at the University of the Witwatersrand, Johannesburg. It has not been submitted before for any degree or examination at any other University.



Stirling Scholes
17 November 2020

Abstract

The ability to create 'structured' light with precisely controlled amplitude, phase and polarisation profiles has led to many new applications of light, including high-energy lasers in the defence sector. Laser systems which simultaneously produce high energy yet low divergence ('bright') beams have remained elusive. In particular, solid-state lasers suffer deleterious thermally-induced optical and stress effects, limiting the total energy which can be added to the system. Additionally, performing safe and accurate characterisations of high energy beams has proved challenging. Here, the theoretical and experimental tools of structured light are applied to develop brighter laser systems and characterise them. Specifically, this work derives and experimentally demonstrates a lossless phase-only reshaping method which significantly enhances the brightness of a beam for a given power by reducing its divergence. Further, this work shows that using a beam with an annular intensity profile mitigates the deleterious thermal effects in solid state lasers, raising the energy limit. When used together, these approaches can enhance brightness by four orders of magnitude. A low energy physical simulator for high energy laser sources, built around a Digital Micro-mirror Device is demonstrated, allowing for the safe characterisation of high-energy sources at lower cost and complexity.

I would like to dedicate this dissertation to my parents, friends and colleagues.

Acknowledgements

I would like to thank my supervisor Professor Andrew Forbes for his consistent and wise guidance without which this work would not have been possible.

I would like to acknowledge the Council for Scientific and Industrial Research (CSIR) in collaboration with the Department of Science and Technology (DST) for the funding provided through the CSIR-DST Interbursary Incentive Scheme.

Table of contents

List of figures **xii**

List of tables **xx**

List of publications **xxi**

1 Introduction **1**
1.1 Structured light . . . 3
1.1.1 Theoretical tools . . . 5
1.1.2 Experimental tools . . . 11
1.2 Laser brightness . . . 15
1.2.1 Effects of structured light on brightness . . . 17
1.3 Simulating high energy laser sources . . . 19
1.4 Outline of the dissertation . . . 20
References . . . 21

2 Creating structured light with Digital Micro-mirror Devices **37**
2.1 Digital Micro-mirror Devices . . . 37
2.2 Diffractive properties of DMDs . . . 39
2.2.1 The DMD as a blaze grating . . . 39
2.2.2 The DMD as a modified amplitude grating . . . 41
2.2.3 DMD efficiency measured experimentally . . . 47
2.3 Generating high fidelity modes with the DMD . . . 49
2.3.1 Amplitude profile correction . . . 50
2.3.2 Phase profile correction . . . 53
2.4 Summary of chapter 2 . . . 57
References . . . 57

3 Manipulating structured light using LCoS Spatial Light Modulators **61**
3.1 Lossless reshaping of light . . . 61

3.2 Theoretical outline . . . 63
3.2.1 Derivation of equations . . . 64
3.2.2 Properties of the $\alpha(x)$ function . . . 66
3.2.3 Deriving the second phase element . . . 68
3.3 Experimental implementation I . . . 69
3.4 Experimental results I . . . 70
3.5 Improving the M^2 . . . 73
3.6 Experimental implementation II . . . 74
3.7 Experimental results II . . . 77
3.8 Summary of chapter 3 . . . 78
References . . . 79

4 Structured light and thermal effects **85**
4.1 A central heat source . . . 88
4.1.1 The temperature profile u(r,t) . . . 88
4.1.2 Thermal phase aberrations . . . 95
4.1.3 Stress resulting from a central heat source . . . 97
4.2 An annular heat source . . . 100
4.2.1 Annular sources and stress . . . 100
4.2.2 The local action . . . 101
4.2.3 The global action . . . 105
4.3 Experimental setup . . . 106
4.4 Results for a central source . . . 108
4.5 Results for an annular source . . . 109
4.5.1 The local action . . . 109
4.5.2 The global action . . . 110
4.6 Discussion . . . 113
4.6.1 Effects on brightness . . . 115
4.7 Summary of chapter 4 . . . 116
References . . . 117

5 Conclusion **121**

List of figures

1.1 Left, intensities of LG beams for $\ell \in [0,1]$ and $p \in [0,2]$. Right, intensities of HG beams for $n \in [0,1]$ and $m \in [0,2]$. For $\ell = p = m = n = 0$ both the HG beams and LG beams reduce to a Gaussian beam. 4

1.2 Left, an amplitude-only transformation using an aperture which resizes a beam in the near field. Right, a phase-only transformation using a lens which resizes the beam in the far field. 6

1.3 Top, the transmission function derived by Eq. 1.29. The azimuthal phase $\varphi(x,y)$ is combined with a diffraction grating $g(x,y)$ yielding a characteristic 'forked' (i.e. bifurcating) grating. The inclusion of the $J_1^{-1}[A(x,y,z_0)]$ component modulates the transmission function by the amplitude $A(x,y)$. Bottom, the effect of the transmission function on a uniform initial field $E_0(x,y,z_0)$. The desired LG_1^0 beam forms in the first order diffraction T_1. The conjugate order T_{-1} creates a beam with the conjugate of the desired phase, in this case producing a LG_{-1}^0. 9

1.4 A conceptual cross section of a LCoS SLM. For an incident beam with polarisation components e_0 and e_n a spatially variable phase delay $\phi(x,y)$ can be imparted to one polarisation component of the beam by rotating the liquid crystals. 12

1.5 The structure of the mirror array of a DMD. Panel 2 and 3, micrographs courtesy of University of Rochester/URnano. 14

1.6 A conceptual representation of the three possible mirror states: on; parked; and off. 14

1.7 The transmission function derived by Eq. 1.41 for an LG_1^0 beam. Note how in comparison to Fig. 1.3 the transmission function is binarised, i.e. equals either 0 or 1. 15

2.1 A comparison between a blaze grating (left) and a DMD with the mirrors in the on state (right). The tilt angle θ_B and the incident angle θ_i are measured relative to the screen normal of the DMD with counter-clockwise as the positive direction. 40

2.2 The incident wavelength required to blaze the 1st, 2nd and 3rd order diffractions as a function of incident angle for a mirror tilt angle of $\theta_B = \pi/15$ and $N = 1/7.6 \times 10^{-3}$. 40

2.3 (a) The set of diffraction peaks allowed by the second sinc factor in each summation. (b) Shows how the envelope function (in red) defined by $\text{sinc}(w\frac{m}{\Delta})$ modulates the intensity of the allowed peaks to produce the observed diffraction pattern. 43

2.4 The observed diffraction pattern for the TI 3000 DMD aligned at an incident angle of 0 rad with all mirrors in the on state. Note that the diffraction orders labelled $(-1,1)$ and $(-1,-1)$ are brighter than those labelled $(1,1)$ and $(1,-1)$. 44

2.5 (a) The relationship between the envelope function (in red) and the allowed diffraction orders for a pure amplitude grating. Note how in (a) the envelope function is fixed around the zero order diffraction peak. (b) The effect of decoupling the envelope function from the zero order. Energy can now be moved into the first order diffraction without changing the relative positions of the orders in space. 45

2.6 The experimental setup used to verify the treatment of the DMD presented in Sec. 2.2.2. An expanded and collimated beam was incident onto a DMD and the power of the relevant diffraction order was measured by a power meter. 47

2.7 Efficiency of the first order holographic diffraction as a function of aperture radius. The black line is predicted by Eq. 2.19 based on the number of mirrors in the on state in the hologram. The red diamonds are the experimentally measured values. 48

2.8 To determine the mode quality, an expanded and collimated beam was incident on a 3000 series DMD. The holographic first order diffraction was then imaged, via a 4f system to a camera. 49

2.9 (a) the computed hologram as displayed on the DMD screen. (b) the measured beam with the DMD aligned at 0 rad. (c) the measured beam with the DMD aligned at $\pi/15$ rad, when using the initial encoding scheme. (d), (e) and (f) show the same but using the optimised encoding. 50

2.10 Correlation between the theoretical (green solid) and experimental (blue dots) LG_5^5 beam for both alignments and encoding schemes. The inset shows a side by side comparison of the beams with the ideal beam on the left and the measured beam on the right. (a) the initial encoding scheme at an angle of 0 rad. (b) the initial encoding scheme at an angle of $\pi/15$ rad. (c) the optimised encoding scheme at an angle of 0 rad. (d) the optimised encoding scheme at an angle of $\pi/15$ rad. 52

2.11 The setup to demonstrate the efficacy of the wavefront correction method. An expanded and collimated beam was incident on a DMD. The first order holographic diffraction was then focused through a lens. A camera was placed at the focal plane of the lens. 54

2.12 The effect of the aberration correction procedure for the 3000 series DMD. The top row shows: (a) an LG_5^0; (b) an LG_0^5; and (c) a superposition of an LG_5^5 and LG_{-5}^5 beam. The bottom row shows the beams after correction. The colourmap is the same as that used in Fig. 2.9. 54

2.13 Experimental aberration correction of the 6500 DMD. (b) The initial beam aberration is too large for the algorithm to handle, the first order astigmatism was manually corrected for. (c) The partially corrected beam after the manual aberration correction. After this, the intermediate beam can be fed through the G-S algorithm to find the remaining phase distortions. (d) The corrected beam. 55

2.14 (a), (b), (c) and (d) show the computed holograms to generate: the text "DMD" using amplitude only modulation; a phase singularity at the focal plane of a lens; an HG_8^8 mode using complex amplitude modulation; and a superposition of an HG_3^7 and an HG_7^3 mode using complex amplitude modulation. Note the apparent elongation of the holograms, this is a result of the optimised encoding scheme used to generate the holograms. When displayed on the DMD, the pixel arrangement of the screen causes the holograms to be drawn out to the correct aspect ratio. (e), (f), (g) and (h) show the intended intensity profiles of the beams generated by the holograms in the first row. (i), (j), (k) and (l) show the experimentally measured beams. 56

3.1 The different approaches to creating structured light. Panel (a) shows how lossless single-step shaping can be achieved using a phase-only element, but requires the phase at the target plane to be left as a free DoF, requiring a second element for correction. Panel (b) shows how a single step in which the amplitude of the beam is also controlled can produce ideal structured light, but now the process is lossy. 62

3.2 The mapping function α for a truncated Gaussian input to an annular polynomial output. The insets show the intensities of the input and output beams while the panels show the beam profiles. 67

3.3 Conceptual design of the experimental setup used to implement the method. A well expanded and collimated beam from a HeNe source was incident on the SLM. The beam from the SLM passed through lens f1 forming the desired profile $|Q(x)|^2$ at the plane of the black aperture A1. The plane of A1 was imaged to camera by a 4f system (lenses f2 and f3) . Here, the second beam shaping element described in Sec. 3.2.3 would be placed at the plane of the black aperture A1. 69

3.4 Measured modes and profiles for (a) beams with radial symmetry and (b) beams with Cartesian symmetry. Each row of the figure shows, from left to right, the phase of the first shaping element, the experimentally measured beam, and a comparison of the profiles of the simulated and measured beams as a black dashed line and blue solid line respectively. The profile cross-sections are plotted on a transverse axis in millimetres. The insets in each experimental result show the simulated beam. 71

3.5 The 'double bar' and 'cross hair' profiles. These profiles are the result of superpositions of modes at right angles to each other in a Cartesian symmetry. 72

3.6 The beam quality of structured light fields decreases with increasing mode index (see Table. 1.1), resulting in an increase in the beam quality factor, M^2, shown here for the examples of Hermite-Gaussian, Laguerre-Gaussian and Super-Gaussian beams, with the mode index plotted as $2m+2n+1$, $2p+|\ell|+1$ and k, respectively. By using the lossless reshaping technique presented in the first part of the chapter it is possible to move 'down the curve' towards a Gaussian ($M^2 = 1$) using an optical system with two phase-only elements, thus enhancing the brightness, shown here conceptually. . 73

3.7 (a) A step-wise depiction of the two-step approach corresponding to the subsequent panels. (b) The experimental setup consisted (conceptually) of two SLMs to implement the desired phase transformations. SLM 1 acted as the second phase element creating a beam of amplitude $Q(x,y)$ with phase $-\psi$. The beam passed through a lens f1 and was imaged (f2 and f3) onto the first phase element (SLM 2) with phase ϕ. The final beam, having a Gaussian amplitude $A(x,y)$ and a flat phase front was imaged by a camera. (c) The phase profiles $-\psi$ and ϕ encoded on SLM 1 and SLM 2 respectively. The elements match the case depicted in panels (a) and (b) and are plotted on a shared transverse axis in millimetres. 75

3.8 Input beams shown as an intensity and profile, each with a flat phase, and the measured Gaussian output beam, shown for the four tested cases: (a) radial Super-Gaussian, (b) radial annulus, (c) Cartesian Super-Gaussian and (d) Cartesian linear, a beam with a linear intensity gradient. The examples cover Radial and Cartesian symmetry in high M^2 initial beams. The Gaussian beams are shown as cross-sectional profiles for x (blue dashed) and y (red solid), with the black dotted profiles as the theoretical prediction. The insets show the measured camera intensities. All profiles are plotted on an axis in millimetres. 76

3.9 The 2^{nd} moment width for the Gaussian beam as a function of propagation distance from the focusing lens, shown as measured data and fitted curves. Fitting the data to the equation $W^2(z) = W_0^2 + \left(M^2\right)^2 \times [\lambda/(\pi W_0)]^2 (z-z_0)^2$ allows the unknown parameters to be inferred, including the M^2. This example plot is for the radial Super-Gaussian to Gaussian case and shows a beam quality factor improvement from $M^2 = 3.64$ to $M^2 = 1.06 \pm 0.05$ . . . 77

4.1 The cases this chapter examines. The analysis makes use of an abstract heat source $Q(r,t)$ and probe beams. The heat source is separated into two categories, central and annular. The annular case is further divided into two sub categories, the local action and the global action. The local action refers to an examination of the thermal phase-only within the annular region under heating, while the global action refers to the examination of the thermal phase for the entire optic. The red circles indicate the location of the heat source relative to the probe beam while the dotted black line indicates the circumference of the optic. The central heat source is probed with an HG beam. The local action of the annular source is probed with an LG beam. The global action of the annular source is probed with both superpositions of LG and HG beams. 86

4.2 The spatial and temporal temperature profile of a Tm:YLF rod with a central quasi-continuous uniform-intensity source, where each pulse lasts 0.01 s with a 0.09 s cooling period. The raised panels at the boundaries of the surface plots show line plots of the on axis temperature over time for the uniform-intensity source together with the structure of the heat source (red dotted). 93

4.3 The values of the $A_{\tilde{2},0}$ and $A_{\tilde{4},0}$ Zernike coefficients over time. The insets show the intensity (at the focal plane of a lens) and the aberrating phase $\phi(r,t)$ for: (a) The unaberrated HG mode; (b) The $A_{\tilde{2},0}$ aberration on the HG mode; (c) The $A_{\tilde{4},0}$ aberration on the HG mode, and (d) The cumulative effect of all $A_{\tilde{n},0}$ coefficients. 96

4.4 The stress experienced by a rod when heated by a central (red dashed) and annular (solid red) source. The insets show: the temperature profile of the rod at 0.25 s and 0.75 s; the concentric circles indicate the boundary of the rod and the location of the heat source; and the line plots show the radial stress profile. 101

4.5 The temperature $u(r,t)$ and phase $\phi(r,t)$ profiles for a rod in an annular heating regime. As the source approaches an annular ring at the radius of the rod, an area of constant phase develops in the centre of the rod, reducing aberrations. 102

4.6 A convergent lens embedded in the centre of a divergent lens. The global curvature over the radius for which the Radial Zernike polynomials are defined is flat. The annular region $[\epsilon,1]$ over which the Annular Zernike polynomials are defined retains its local curvature. 102

4.7 (a),(b) and (c), input LG beams spatially matched to annular heat sources with an outer boundary at $\omega = 0.3\times$, $0.5\times$, and $0.83 \times R$ of a rod. (d),(e) and (f), the phase profiles associated with the heat sources as described by the Annular Zernike polynomials. (g),(h) and (i), the intensities of the aberatted input beams at the focal plane of a lens, the inset line plots show the unaberrated and aberrated profiles as black dashed and orange solid lines respectively. Note that the output beams have been independently normalised to aid in the visualisation. 104

4.8 (a) and (b), the aberrating phase $\phi(r,t)$ and corresponding temperature $u(r,t)$ for a heat source with $\omega = 0.86 \times R$. The outermost black dashed circle indicates the radius of the rod. The annular heat source is indicated by the two innermost red circles. (c) and (e), the super-positions of HG and LG beams respectively. (d) and (f) the intensities of the beams at the focal plane of a lens. The inset line plots show the unaberrated and aberrated profiles as black dashed and orange solid lines respectively. 106

4.9 The experimental setup shown conceptually. The DMD was used as though it was an old film projector, i.e. dynamically simulating the heated optic by displaying an ordered set of holograms corresponding to the temperature profile of the optic. Each hologram encodes an amplitude $A(x,y)$ and a phase, where the total phase $\Omega(x,y)$ is made up of three components: the phase inherent to the desired mode $\varphi(x,y)$; the phase of the thermal aberration $\phi(r,t)$, and the corrective phase accounting for the deformations to the DMD $\psi(x,y)$. A well expanded and collimated beam from a HeNe source was incident on the DMD. The beams created by the holograms were recorded at the focal plane of a lens by a camera. 107

4.10 The self action of a central heat source on an HG beam over time. The upper insets show the temperature $u(r,t)$ of the modelled rod and the aberrating phase $\phi(r,t)$ of the hologram. The main panels show the measured beam at four points in time, (a) at $t = 0$, (b) at $t = 3$, (c) at $t = 6$, and (d) at $t = 10$ ms respectively. The line plots show the profiles of the simulated beam and the measured beams as black dashed and orange solid lines respectively. . 108

4.11 The self action of an annular heat source on an LG beam. The upper insets show the temperature of the rod $u(r,t)$ and aberrating phase $\phi(r,t)$ of the hologram. Panels (a) through (d) show the measured beams for an annular source with its outer edge at $\omega = 0.31\times$, $\omega = 0.47\times$, $\omega = 0.64\times$ and $\omega = 0.81 \times R$ respectively. The insets in these panels show the input beams. The line plots show the profiles of an unaberrated beam and the measured beams as black dashed and orange solid lines respectively. Panel (e) shows the correlation between the measured beam and the simulation of an unaberrated beam as a function of heat source position. The red dashed line indicates the line of best fit for the experimental data with the shaded region indicating the 95% confidence interval. The blue solid line is the theoretical prediction. 110

4.12 The intensity through an aperture for a Gaussian beam passing through the modelled rod: over time on the left, and as the annular source moves outward on the right. The red dashed line indicates the line of best fit for the experimental data with the shaded region indicating the 95% confidence interval. The blue solid line is the theoretical prediction. The panels (a) through (d) show the measured beams at the positions indicated by the arrows with the corresponding temperature $u(r,t)$ and aberrating phase $\phi(r,t)$ profiles shown below. Note that each measured beam has been independently normalised to aid in visualisation. 111

4.13 The global action of an annular source on superpositions of HG (c) and LG (d) beams. (a) the temperature $u(r,t)$ of the rod for an annular heat source at its radius. (b) the aberrating phase $\phi(r,t)$ of the hologram. The insets in (c) and (d) show the input beams. The line plots show the profiles of unaberrated beams and the measured beams as black dashed and orange solid lines respectively. 112

4.14 The relationship between total aberration strength calculated as wavefront variance ζ and the outer boundary of the heat source for the Radial (a) and Annular (d) Zernike polynomials respectively. The phase panels (b), (c), (e) and (f) show the phase aberration in each basis at the points indicated by the arrows. ω_0 represents the minimum outer boundary for a heat source of width ω_0. 114

List of tables

1.1 The M^2 values of common beam types with the mode indices shown in braces. 17

2.1 Diffraction efficiency of the TI 3000 DMD. 48

3.1 The cameras, Gaussian and output profile waists used for the experiment. 70
3.2 The correlations between the simulated and measured beams. 71
3.3 The M^2 values of the initial beam profiles used in the experiment, and the predicted brightness enhancement factor, η. 77

4.1 Material constants used in the simulation for a Tm:YLF rod 94

List of publications

1 **S. Scholes**, R. Kara, J. Pinnell, V. Rodríguez-Fajardo, and A. Forbes, "Structured light with digital micromirror devices: a guide to best practice," *Optical Engineering,* 59(4), p.041202, 2019.

2 **S. Scholes**, V. Rodríguez-Fajardo, and A. Forbes, "Lossless reshaping of structured light," *Journal of the Optical Society of America A,* 37, p.C80-C85, 2020.

3 **S. Scholes**, and A. Forbes, "Improving the beam quality factor (M^2) by phase-only reshaping of structured light," *Optics Letters,* 45, p.3753-3756, 2020.

4 **S. Scholes**, and A. Forbes, "Thermal aberrations and structured light I: Analytical model for structured pumps and probes," Submitted to *Applied Physics B* at the time of writing.

5 **S. Scholes**, and A. Forbes, "Thermal aberrations and structured light II: Experimental simulation with DMDs," Submitted to *Applied Physics B* at the time of writing.

Chapter 1

Introduction

Ever since the invention of the laser in 1959 [1.1;1.2], researchers have worked to develop lasing systems which produce brighter beams; i.e. beams which deliver a high energy to a small area over a long propagation distance. High brightness laser sources have become ubiquitous in industrial manufacturing [1.3;1.4] and have seen growing use in the defence sector. While the idea of using high brightness lasers in defence can be traced back to 1984 and U.S. President Ronald Reagan's Strategic Defence Initiative [1.5] it is recent programmes such as Reinmetal Defence's Oerlikon sky shield®, Raytheon Technologies High Energy Laser Weapons System (HELWS®), and the U.S. Navy's Laser Weapons System (LaWS) which have seen the idea implemented. As of 2019, the U.S. Army had pledged an additional $203 million to the ongoing development of high brightness lasers for defence [1.6]. The need for the continued improvement of laser brightness creates the context for this work.

Soon after the invention of lasers it was found that at high input energies, the beams they produced became distorted [1.7]. These distortions were initially characterised in terms of a change in optical path length [1.8] and were attributed to a build up of heat within the gain medium of the laser [1.9]. In 1968 it was shown that by adjusting the temperature of the coolant in a lasing system, the distortions could be partially compensated for [1.10]. This confirmed that the distortions were primarily thermally induced and that the further enhancement of laser brightness required analysis of the thermal properties of lasers [1.11;1.12]. To overcome these thermal effects, many other high brightness laser sources have been developed such as: gas and excimer lasers [1.13]; chemical lasers [1.14;1.15]; dye lasers [1.16]; and fibre lasers [1.17;1.18]. While these systems exhibit superior thermal properties they each have associated limitations. For instance high-energy gas (commonly CO_2 [1.19;1.20]) and excimer [1.21] lasers produce beams with relatively high divergence [1.20;1.22;1.23], chemical

and dye lasers require the use of exotic molecules which introduce problems of chemical handling, depletion and replacement[1.24;1.25], and fibre lasers encounter stimulated Brillouin scattering[1.26;1.27] and mode instabilities[1.28;1.29] which limit their power outputs. For these reasons so called 'solid-state lasers' have remained a viable configuration for high brightness applications. In particular, 'end-pumped' lasing systems are known for their high pump-mode overlap which improves energy extraction and mode discrimination[1.30;1.31]. Subsequent research has sought to overcome the thermally-induced distortions in a number of ways, including interferometric beam correction[1.32], the use of correction optics[1.33;1.34;1.35;1.36;1.37] and custom laser cavities[1.31;1.38;1.39;1.40;1.41]. Despite these advances, the deleterious thermal effects experienced by solid-state lasers remain a topic of active research and are considered the principle limitation of such systems[1.42;1.43;1.44;1.45;1.46].

In addition to the development of laser sources, a broad area of research directed at controlling the properties of beams independent of their source has developed. This area was originally termed[1.47] 'laser beam shaping' and is now referred to as 'structured light'. It concerns the control of light in all its degrees of freedom[1.48]: usually in the structuring of spatial properties, notably polarization, phase and amplitude, but also time or frequency structuring in the context of ultra-fast lasers. Structured light is a highly topical field[1.49] and has driven the use of light in a wide range of applications including simulating quantum states with spin-orbit coupling[1.50;1.51], structured illumination microscopy[1.52] , optical trapping[1.53;1.54], metrology[1.55;1.56], optical communications[1.57;1.58] and many more[1.59;1.51]. Further, laser materials synthesis and[1.60;1.61] processing has been advanced by the use of beams which have specifically designed intensity profiles. For instance laser annealing[1.62], pulsed laser deposition[1.63] and photolithography[1.64] all benefit from beams with a uniform intensity profile, so called 'flattop beams'. The use of structured beams in industrial processes has recently created a confluence between the fields of structured light and high brightness sources particularly around the generation of structured beams directly from laser sources[1.65] at high powers. Such systems have been demonstrated with Laguerre-Gaussian (LG) beams[1.66;1.67;1.68], Hermite-Gaussian (HG) beams[1.69] and beams with non-linear polarisations[1.70;1.71;1.72] termed 'vector beams'. Currently, how these structured beams impact solid-state lasers in terms of heat generation and brightness is not well researched. This work examines these topics and investigates whether structured light can be used to enhance laser brightness. The remainder of this introductory chapter presents overviews of the topics of structured light and laser brightness, as well as establishing their relationship.

1.1 Structured light

The earliest examinations of structured light were performed using LG[1.73;1.74;1.75;1.76] and HG[1.77;1.78] beams. These beams are solutions to the Helmholtz wave equation under the paraxial approximation. The Helmholtz wave equation is given by

$$(\nabla^2 + k^2)E(x,y,z) = 0, \tag{1.1}$$

where k^2 is the wavevector magnitude and ∇^2 is the Laplacian in Cartesian coordinates

$$\nabla^2 = \frac{\partial^2}{\partial x^2} + \frac{\partial^2}{\partial y^2} + \frac{\partial^2}{\partial z^2}. \tag{1.2}$$

The scalar beam $E(x,y,z)$ is defined

$$E(x,y,z) = A(x,y,z)\exp(ikz), \tag{1.3}$$

where $\exp(ikz)$ represents a plane wave travelling in the z direction and $A(x,y,z)$ is the spatially variable complex amplitude. The paraxial approximation assumes $A(x,y,z)$ is a slowly diverging function in z. Consequently, the z component of the Laplacian on $E(x,y,z)$ is negligible

$$|\frac{\partial^2}{\partial z^2}E(x,y,z)| << |k\frac{\partial}{\partial z}E(x,y,z)|. \tag{1.4}$$

Here || represents the magnitude. Under this approximation Eq. 1.1 reduces to

$$\nabla_\perp^2 E(x,y,z) + 2ik\frac{\partial E(x,y,z)}{\partial z} = 0, \tag{1.5}$$

where $\nabla_\perp^2$ is the transverse Laplacian given by

$$\nabla_\perp^2 = \frac{\partial^2}{\partial x^2} + \frac{\partial^2}{\partial y^2}. \tag{1.6}$$

In Cartesian symmetry the HG solution to Eq. 1.5 is given by

$$HG_m^n(x,y,z) = E_m^n(x,y,z) = \frac{1}{\omega(z)}H_m\left[\frac{\sqrt{2}x}{\omega(z)}\right]H_n\left[\frac{\sqrt{2}y}{\omega(z)}\right]\exp\left[-\frac{x^2+y^2}{\omega(z)^2}\right]\exp\left[-i\frac{k(x^2+y^2)}{2R(z)}\right] \times \exp[\psi(m,n,z)]\exp(-ikz), \tag{1.7}$$

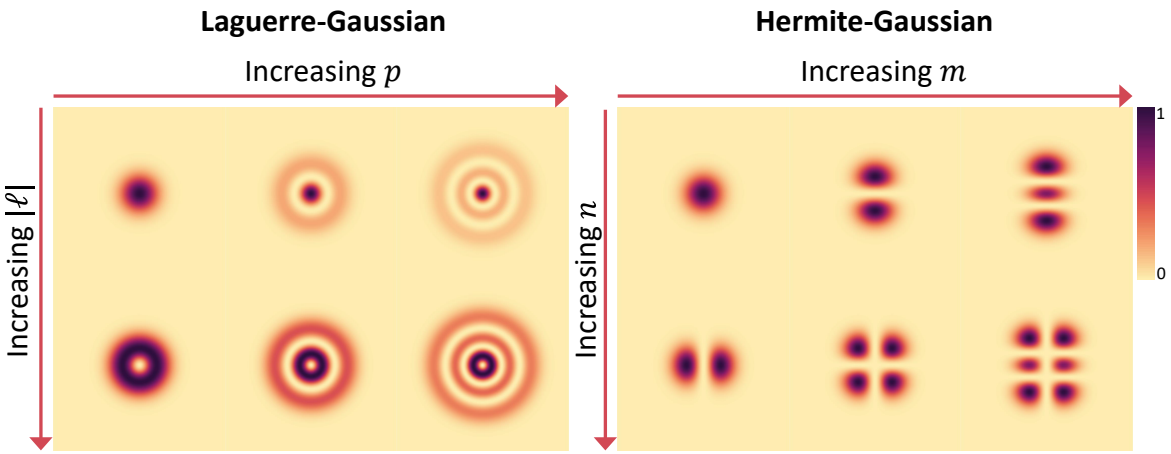


Fig. 1.1 Left, intensities of LG beams for $\ell \in [0,1]$ and $p \in [0,2]$. Right, intensities of HG beams for $n \in [0,1]$ and $m \in [0,2]$. For $\ell = p = m = n = 0$ both the HG beams and LG beams reduce to a Gaussian beam.

where $n, m \in \mathbb{Z} \geq 0$ are the indices of the Hermite polynomials H_n and H_m respectively. In radial symmetry the LG solution to Eq. 1.5 is

$$LG_\ell^p = E_\ell^p(r,\theta,z) = \frac{1}{\omega(z)}\sqrt{\frac{2p!}{\pi(|\ell|+p)!}}\left[\frac{\sqrt{2}r}{\omega(z)}\right]^{|\ell|} L_\ell^p\left[\frac{2r^2}{\omega(z)^2}\right]\exp\left[-\frac{r^2}{\omega(z)^2}\right]\exp\left[\frac{-ikr}{2R(z)}\right] \times \exp(i\ell\theta)\exp[i\psi(p,\ell,z)], \tag{1.8}$$

where L_ℓ^p is the Laguerre polynomial of azimuthal index ℓ and radial index p, for $\ell \in \mathbb{Z}$ and $p \in \mathbb{Z} \geq 0$. The $\exp[i\ell\theta]$ term in Eq. 1.8 is often termed a 'vortex' phase due to its azimuthal (θ) dependence. This phase results in a helical twisting of the wavefront and so imparts orbital angular momentum (OAM) to the beams with which it is associated. Figure. 1.1 shows the intensities for a selection of HG and LG modes. In Eqs. 1.7 and 1.8 $\omega(z)$ is the beam size at a plane z and is defined by

$$\omega(z) = \omega_0\sqrt{1+\left(\frac{z}{z_R}\right)^2}. \tag{1.9}$$

ω_0 is the waist of the beam and z_R is the Rayleigh range given by

$$z_R = \frac{\pi\omega_0^2}{\lambda}. \tag{1.10}$$

$R(z)$ is the radius of curvature defined by

$$R(z) = z\left(1 + \frac{z_R^2}{z^2}\right). \tag{1.11}$$

$\psi(m,n,z)$ and $\psi(p,\ell,z)$ are the Gouy phases given by

$$\psi(m,n,z) = (m+n+1)\arctan\left(\frac{z}{z_R}\right), \tag{1.12}$$

and

$$\psi(p,\ell,z) = (2p+|\ell|+1)\arctan\left(\frac{z}{z_R}\right), \tag{1.13}$$

for the HG and LG beams respectively.

Many other solutions to Eq. 1.5 are known, including Bessel-Gaussian beams [1.79], Ince-Gaussian beams [1.80;1.81], Mathieu-Gaussian beams [1.82;1.83;1.84] and Airy beams [1.85;1.86;1.87]. Beams derived from Eq. 1.5 are termed 'propagation-invariant'. This is because although the beams diverge (get larger) as they propagate their relative amplitude and phase profiles do not change, even when focused by a lens. Conversely, 'non-propagation-invariant' beams do not represent solutions to Eq. 1.5 and so change their amplitude and phase profiles as they propagate. Although non-propagation-invariant beams do not retain their structure in z, they are still of great interest. For instance the flattop beams already mentioned are not a solution to Eq. 1.5 and are thus non-propagation-invariant. They can nevertheless be understood in the context of structured light. Further, by making use of the tools of structured light both propagation-invariant and non-propagation-invariant beams may be created at will. These tools are the focus of the remainder of this section.

1.1.1 Theoretical tools

To create structured light a transformation $T(x,y)$ acts on an initial beam $E_0(x,y,z_0)$ at the plane z_0 to give the desired beam $E_1(x,y,z_1)$ at the plane z_1. A beam $E(x,y,z_0)$ may be defined

$$E_0(x,y,z_0) = A(x,y,z_0)\exp[i\varphi(x,y,z_0)], \tag{1.14}$$

where $A(x,y,z_0)$ is the initial amplitude of the beam and $\varphi(x,y,z_0)$ is the initial transverse phase. In this formalism the transformation $T(x,y)$ may be classified in one of three groups: amplitude-only modulation; phase-only modulation; and complex amplitude modulation. Amplitude- and phase-only modulations each only change one component

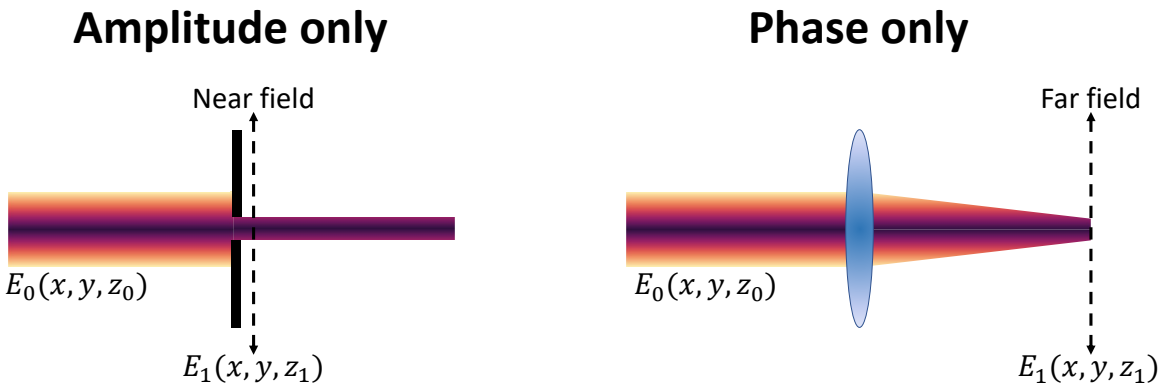


Fig. 1.2 Left, an amplitude-only transformation using an aperture which resizes a beam in the near field. Right, a phase-only transformation using a lens which resizes the beam in the far field.

(either amplitude or phase) of the beam at a given plane. Complex amplitude modulations are a class of transformations which act on only a single component of the beam but change both the amplitude and the phase simultaneously. To illustrate the conceptual differences between phase-only and amplitude-only modulation consider the simplest beam shaping problem, changing the size of a beam of wavelength λ. The beam has an initial size $\omega(z_0)$ at the plane z_0. The transformation acts such that $\omega(z_1) < \omega(z_0)$ for $z_0 < z_1$. This case is depicted for amplitude-only and phase-only transformations in Fig. 1.2. Amplitude modulation achieves this with the following operation

$$E_1(x,y,z_1) = A(x,y,z_0)\exp[i\varphi(x,y,z_0)] \times \text{aperture}(x,y), \tag{1.15}$$

where the aperture(x,y) is defined by

$$\text{aperture}(x,y) = \left\{ \begin{array}{ll} 1, & \text{for } x \text{ and } y < \omega(z_0) \\ 0, & \text{otherwise} \end{array} \right\}. \tag{1.16}$$

By aperturing the beam at the plane z_0, the beam is immediately resized. When a transformation creates the desired beam $E(x,y,z_1)$ at the plane at which the transformation is applied, the transformation is said to act in the 'near field'. The limitation of amplitude modulation is that the total energy of the beam is not preserved. Hence, it is referred to as a 'lossy' transformation. To resize a beam, phase-only modulation imparts the beam with an additional phase such that

$$E_1(x,y,z_1) = A(x,y,z_0)\exp[i\varphi(x,y,z_0)]\exp\left[\frac{-i2\pi}{\lambda z_1}(x^2+y^2)\right]. \tag{1.17}$$

This operation is identical to passing the beam through a lens of focal length z_1. As the beam propagates from z_0 to z_1 it will reduce in size. Although the phase of the beam is altered at the plane z_0 the effect this has on the amplitude of the beam is only observed as the beam propagates, hence, phase-only modulation is said to affect the amplitude in the 'far field'. Phase-only modulation is said to be a 'lossless' transformation because it preserves the total energy of the beam.

To extend both phase-only and amplitude-only modulation to controlling both the amplitude and phase of a field, the transmission function $T(x,y)$ is expressed in terms of a periodic spatial function. To control both the amplitude and phase of a beam, phase-only modulation is extended to complex amplitude modulation as follows. The transmission function $T(x,y)$ is a phase-only function of the form [1.88]

$$T(x,y) = \exp\{i\phi[A(x,y,z_0),\varphi(x,y,z_0)]\}. \tag{1.18}$$

Written as a Fourier series the function becomes

$$T(x,y) = \sum_{m=-\infty}^{m=\infty} T_m[A(x,y,z_0)]\exp[im\varphi(x,y,z_0)], \tag{1.19}$$

with

$$T_m = \frac{1}{2\pi}\int_{-\pi}^{\pi} \exp\{i\phi[A(x,y,z_0),\varphi(x,y,z_0)]\}\exp[-im\varphi(x,y,z_0)]d\varphi. \tag{1.20}$$

For a desired beam

$$E_1(x,y,z_1) = A(x,y,z_1)\exp[i\varphi(x,y,z_1)], \tag{1.21}$$

normalised such that $A(x,y,z_1) \in [0,1]$ and $\varphi(x,y,z_1) \in [-\pi,\pi]$ it is possible to determine an expression which causes the field to form in the first term of Eq. 1.19. This occurs if the following relationship is satisfied

$$T_1(x,y) = A(x,y,z_1). \tag{1.22}$$

For a function F, take as an Ansatz

$$\phi[A(x,y,z_1),\varphi(x,y,z_1)] = F[A(x,y,z_1)]\sin[\varphi(x,y,z_1)]. \tag{1.23}$$

The Jacobi-Anger identity [1.89] states

$$\exp\{iF[A(x,y,z_1)]\sin[\varphi(x,y,z_1)]\} = \sum_{m=-\infty}^{m=\infty} J_m\{F[A(x,y,z_1)]\}\exp[im\varphi(x,y,z_1)]. \tag{1.24}$$

J_m represents the m$^{\text{th}}$ order Bessel function. Hence

$$\begin{aligned} T_1 &= \frac{1}{2\pi}\int_{-\pi}^{\pi} J_1\{F[A(x,y,z_1)]\}\exp[i\varphi(x,y,z_1)]\exp[-i\varphi(x,y,z_1)]d\varphi, \\ T_1 &= J_1\{F[A(x,y,z_1)]\}. \end{aligned} \tag{1.25}$$

Meaning

$$T_1 = A(x,y,z_1), \tag{1.26}$$

for

$$F(x,y,z_1) = J_1^{-1}[A(x,y,z_1)]. \tag{1.27}$$

J_1^{-1} represents the inverse of the 1$^{\text{st}}$ order Bessel function. The transmission function of the hologram which modulates both the amplitude and the phase is

$$T(x,y) = J_1^{-1}[A(x,y,z_1)]\sin[\varphi(x,y,z_1)]. \tag{1.28}$$

To use Eq. 1.28 in practice, it must be modified to include an additional 2-dimensional diffraction grating $g(x,y)$, defined using a grating number to specify its periodicity in lines per millimetre. Including this grating Eq. 1.28 becomes

$$T(x,y) = J_1^{-1}[A(x,y,z_0)]\sin[2\pi g(x,y) + \varphi(x,y,z_0)]. \tag{1.29}$$

This is because although T_1 will create the beam $E_1(x,y,z_1)$, the other terms in the expansion of Eq. 1.19 given by T_m for $m \in [-\infty,\infty]$, $m \neq 1$ will also create beams which propagate collinearly with T_1. The desired beam created by T_1 can be separated out by adding to the phase $\varphi(x,y,z_1)$ the grating function $g(x,y)$. In this way, complex amplitude modulation can be thought of in terms of a diffraction grating. It is well understood from the wave nature of light that when a beam of wavelength λ illuminates an object which has a spatial periodicity in either phase or amplitude on the order of λ, it separates into many independent diffraction orders. Within each of these diffracted beams, the structure is governed by the interference effects of the diffracted waves. The interference of these waves is in turn governed by the spatial periodicity of the object. Hence, by designing a diffractive structure which has a spatially variable amplitude or phase it is possible to engineer the interference of the resulting waves to yield a beam with a specific amplitude and phase structure in the 1$^{\text{st}}$ order diffraction. Consider an LG_1^0 beam, Fig. 1.3 illustrates the transmission function which creates this beam as given by Eq. 1.29. The figure also shows

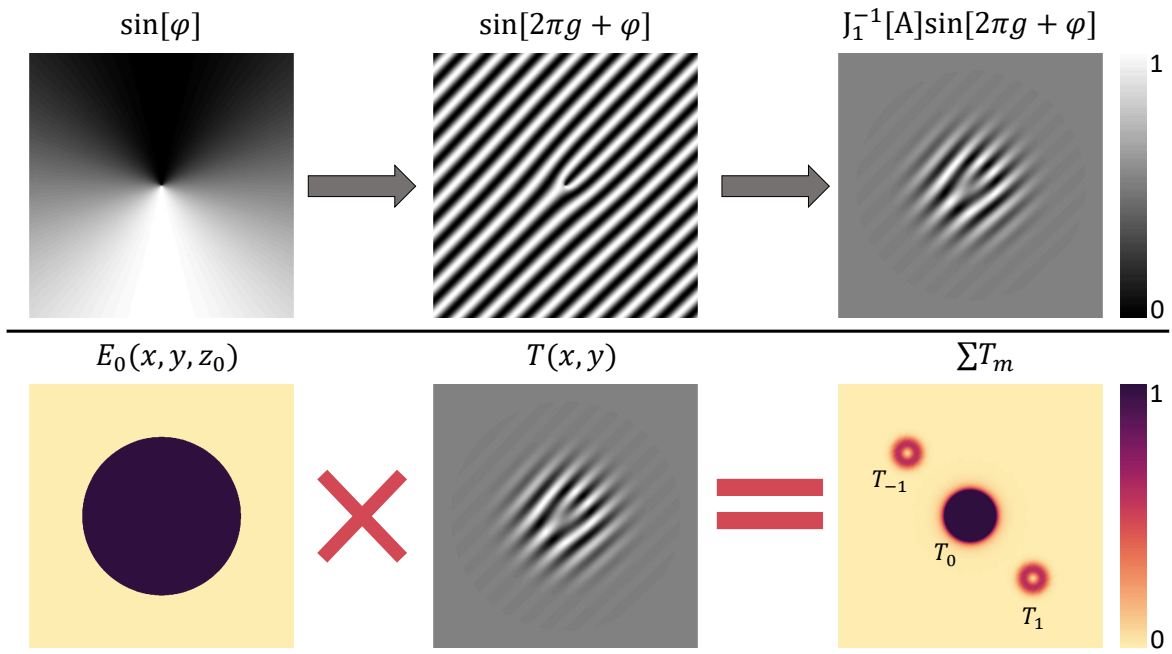


Fig. 1.3 Top, the transmission function derived by Eq. 1.29. The azimuthal phase $\varphi(x,y)$ is combined with a diffraction grating $g(x,y)$ yielding a characteristic 'forked' (i.e. bifurcating) grating. The inclusion of the $J_1^{-1}[A(x,y,z_0)]$ component modulates the transmission function by the amplitude $A(x,y)$. Bottom, the effect of the transmission function on a uniform initial field $E_0(x,y,z_0)$. The desired LG_1^0 beam forms in the first order diffraction T_1. The conjugate order T_{-1} creates a beam with the conjugate of the desired phase, in this case producing a LG_{-1}^0.

the effect of the transmission function on a uniform initial field $E_0(x,y,z_0)$. To extend amplitude-only modulation to complex amplitude modulation, consider a 1-dimensional pulse train of the form

$$T(x) = \sum_{m=-\infty}^{m=\infty} \text{rect}\left[\frac{x-(m+p_x)\bar{\Delta}_x}{\bar{\omega}_x\bar{\Delta}_x}\right], \tag{1.30}$$

where $\text{rect}(x,\bar{\omega_x},p_x,\bar{\Delta}_x)$ is defined as

$$\text{rect}(x,\bar{\omega_x},p_x,\bar{\Delta}_x) = \left\{\begin{array}{ll} 1, & \text{for } |\frac{x-(m+p_x)\bar{\Delta}_x}{\bar{\omega}_x\bar{\Delta}_x}| < \frac{1}{2} \\ \frac{1}{2}, & \text{for } |\frac{x-(m+p_x)\bar{\Delta}_x}{\bar{\omega}_x\bar{\Delta}_x}| = \frac{1}{2} \\ 0, & \text{otherwise} \end{array}\right\}. \tag{1.31}$$

Here $\bar{\Delta}_x$ is the period, with p_x and $\bar{\omega}_x$ determining the position and the width respectively. This pulse train can be written as a Fourier series

$$T(x) = \sum_{m=-\infty}^{m=\infty} T_m \text{Exp}\left[i2\pi m\left(\frac{x}{\bar{\Delta}_x}\right)\right]. \tag{1.32}$$

The m$^{\text{th}}$ coefficient is given by

$$T_m = \frac{1}{\bar{\Delta}_x}\int_{\bar{\Delta}_x\omega_x\left(\frac{p_x}{\omega_x}-\frac{1}{2}\right)}^{\bar{\Delta}_x\omega_x\left(\frac{p_x}{\omega_x}+\frac{1}{2}\right)} \text{Exp}\left[i2\pi m\left(\frac{x}{\bar{\Delta}_x}\right)\right] dx, \tag{1.33}$$

where the bounds of the integral reflect the region of non-zero values for the pulse train. Hence,

$$T_m = \frac{e^{2i\pi m p_x}\sin(m\pi\bar{\omega}_x)}{m\pi}. \tag{1.34}$$

For a properly normalised field

$$E_1(x,z_1) = A(x,z_1)\exp[i\varphi(x,z_1)], \tag{1.35}$$

where $A(x,z_1) \in [0,1]$ and $\varphi(x) \in [0,2\pi]$, it is possible to determine expressions for $\bar{\omega}_x$ and p_x such that the field forms in the first term of Eq. 1.30

$$\frac{1}{\pi}E_1(x,z_1) = \frac{1}{\pi}A(x,z_1)\exp[i\varphi(x,z_1)] = T_1(x) = \frac{1}{\pi}\sin[\pi\bar{\omega}(x)]\exp[i2\pi p(x)]. \tag{1.36}$$

This gives

$$\begin{aligned} \bar{\omega}(x) &= \frac{1}{\pi}\arcsin[A(x,z_1)], \\ p(x) &= \frac{1}{2\pi}\varphi(x,z_1). \end{aligned} \tag{1.37}$$

Again, to separate the beam created in T_1 the phase function $p(x)$ becomes

$$p(x) = \frac{1}{2\pi}\varphi(x,z_1) + g(x,y), \tag{1.38}$$

where $g(x,y)$ is a 2-dimensional diffraction grating. Since the 1$^{\text{st}}$ order diffracted beam (T_1) forms at the plane of the grating, complex amplitude modulation acts in the near field. Further, the incident energy of the illuminating beam is divided amongst the diffraction orders, as seen in Fig. 1.3, meaning complex amplitude modulation is a lossy transformation. Equations 1.28 and 1.36 show that if a device can impart a spatially varying phase or amplitude to a beam, that device can create structured light. These devices are

known collectively as Spatial Light Modulators (SLMs) and are the experimental tools of structured light.

1.1.2 Experimental tools

From Sec. 1.1.1, it is clear that to create structured light the amplitude and the phase of a beam must be controlled. Historically, this was achieved by fabricating custom diffractive or refractive optics. Since these optics were physically manufactured from an optical medium (such as glass), each one had to be designed to perform a single, specific transformation. Today, the structuring of light is achieved with the use of electro-optical devices called Spatial Light Modulators and Computer Generated Holograms (GCHs). SLM is a general term for any device which can spatially modulate the phase or amplitude of a field, but normally refers to Liquid Crystal on Silicon SLMs (LCoS SLMs) for phase modulation, and Digital Micro-mirror Devices (DMDs) for amplitude modulation. These devices are based on digital display technology and so have pixellated screens on which images can be shown. To 'shape' light, i.e. impart structure to it, the devices display a hologram. This is an image which when displayed on the SLM's screen causes it to take on a spatially-varying amplitude (for DMDs) or phase (for LCos SLMs). Hence, when illuminated, these devices impart this amplitude and phase information to the incident beam, resulting in structured light. The principle advantage of the SLM approach over the classical optics approach is that it is dynamic. By changing the hologram which an SLM is displaying, the structure of the beam it creates can be changed at rates ranging from Hz (for LCoS SLMs) to kHz (for DMDs).

The creation of structured light using SLMs is hindered by two of their inherent properties. First, since the screens of SLMs are made up of discrete pixels ranging in size from 4.4 μm for DMDs to 8 μm for SLMs, the screens themselves act as diffraction gratings for visible wavelength light. This causes an incident beam to diffract into many independent beams, resulting in roughly 40% and 75% of the incident light being lost for SLMs and DMDs respectively. In the case of DMDs this loss can be reduced to 50% by optimising the angle at which light is incident on the device. The reason for this is explored in depth in Chp. 3. The diffractive effects of the SLM are entirely separate to those of the diffraction grating $g(x, y)$ which is deliberately introduced in Eq. 1.29 and 1.38. The second limitation is that any displayed hologram is a discretised approximation to the continuous true transformation given by Eq. 1.29 and 1.38. The validity of this approximation is dependent on the spatial rate of change (the gradient) of the transformation. If a large change in

amplitude or phase is required over a distance comparable to the size of the pixels, the SLM cannot accurately create the desired structure of light.

Liquid Crystal on Silicon Spatial Light Modulators

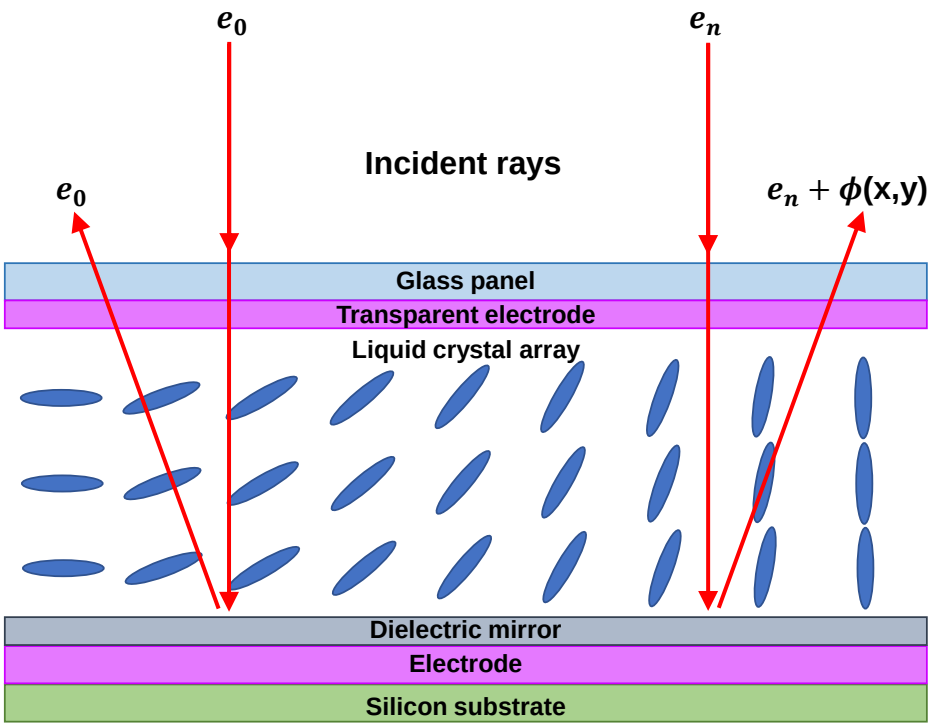


Fig. 1.4 A conceptual cross section of a LCoS SLM. For an incident beam with polarisation components e_0 and e_n a spatially variable phase delay $\phi(x,y)$ can be imparted to one polarisation component of the beam by rotating the liquid crystals.

Dynamic control of the structure of light has been extensively demonstrated through the use of LCoS SLMs; thus the devices are considered ubiquitous in the field of structured light [1.90;1.91]. These devices are analogous to the conventional Liquid Crystal Display (LCD) panels found in digital screens. Specifically, LCoS SLMs consist of an array of nematic birefringent liquid crystals [1.92] layered between a set of electrodes, as shown in Fig. 1.4. The term 'nematic' defines the liquid crystals as having a consistent orientation, which is characterised as the optical axis. As a consequence of the birefringence of the liquid crystals, the screen as a whole exhibits a polarisation- and orientation-dependent refractive index: n_0 for polarisations parallel to the optical axis, and n_e for polarisations perpendicular to it. By applying a bias voltage across the electrodes, the liquid crystals can be rotated and the effective refractive index of the screen changed for a specific

linear polarisation of light. This change in effective refractive index imparts a spatially variable phase $\phi(x,y)$ to the beam incident on the LCoS SLM. For a beam comprised of the polarisation components e_0 and e_n, the screen imparts [1.93] a spatially variable phase

$$\phi(x,y) = \frac{2\pi}{\lambda}[n_e(\theta_{xy}) - n_0(\theta_{xy})]d. \tag{1.39}$$

Here λ is the wavelength and d is the thickness of the screen. The relationship between the effective refractive index of the screen for each polarisation component and the angle θ_{xy} of a liquid crystal at the position (x,y) is [1.92;1.93;1.94]

$$\frac{1}{n_e^2(\theta_{xy})} = \left[\frac{\cos(\theta_{xy})}{n_e}\right]^2 + \left[\frac{\sin(\theta_{xy})}{n_0}\right]^2. \tag{1.40}$$

Due to the birefringent nature of the liquid crystals, the phase $\phi(x,y)$ given by Eq. 1.39 is only applied to the polarisation component of the beam which is perpendicular to the specific optical axis of the screen. To create structured light using an LCoS SLM, the transmission function $T(x,y)$ from Eq. 1.29 is converted to a greyscale image, with pixel values ranging $0-255$. This image is displayed on the screen of the LCoS SLM. The grayscale values correspond to a set of calibrated voltages, and so to specific phases, such that $0 \rightarrow \phi = 0$ and $255 \rightarrow \phi = 2\pi$. Hence, by using a hologram with the correct complex amplitude transmission function $T(x,y)$, a beam with a desired amplitude and phase profile can be created.

Despite advances in LCoS SLM technology, a number of inherent drawbacks remain: their polarisation sensitivity, high costs and slow refresh rates, i.e. how many times the hologram can be changed on the screen, per second. These limitations can be addressed by using a Digital Micro-mirror Device (DMD) in place of an LCoS SLM.

Digital Micro-mirror Devices

DMDs have been used to create vector beams [1.95;1.96;1.97], HG beams [1.98], LG beams [1.99], Ince-Gaussian beams [1.100] and Super-Gaussian beams [1.101], amongst others [1.102]. DMDs have also been used to detect [1.103;1.104;1.105] structured light fields. They have also been integrated into laser cavities to provide dynamic control of lasing modes [1.106;1.107;1.108]. DMDs are constructed from two assemblies. The first is the array of Micro-mirrors itself, referred to as the screen. The second is the driver unit for the screen. The driver unit hosts the electronics that operate the screen and facilitate communication between the DMD and external devices such as computers. The screen consists of an array of individually-

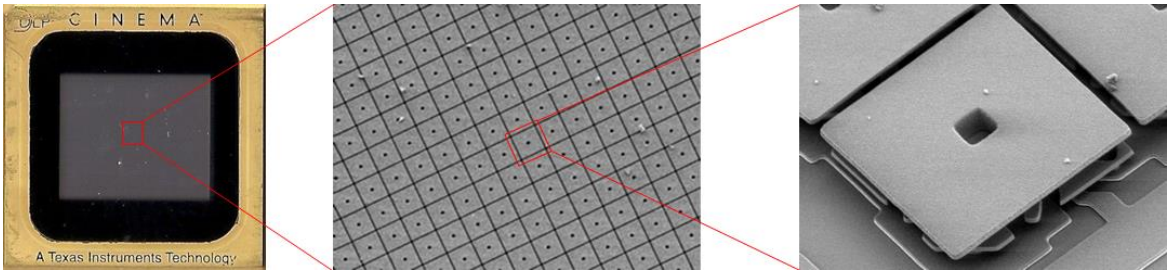


Fig. 1.5 The structure of the mirror array of a DMD. Panel 2 and 3, micrographs courtesy of University of Rochester/URnano.

addressable square Micro-mirrors behind a protective glass sheet. Each square mirror pivots about a hinge mounted along its diagonal allowing it to occupy one of three states: the 'on state', in which the mirrors are tilted to direct light in a desired direction; the 'off state', in which the mirrors tilt the opposite way, reflecting light away from the desired direction; and the 'parked state' where the mirrors are parallel relative to the plane of the protective glass sheet. When the DMD displays an image (such as a hologram), the mirrors may only be instructed to occupy the on or off states. In this way the DMD is a binary amplitude modulator. The mirrors only occupy the parked state when the device is

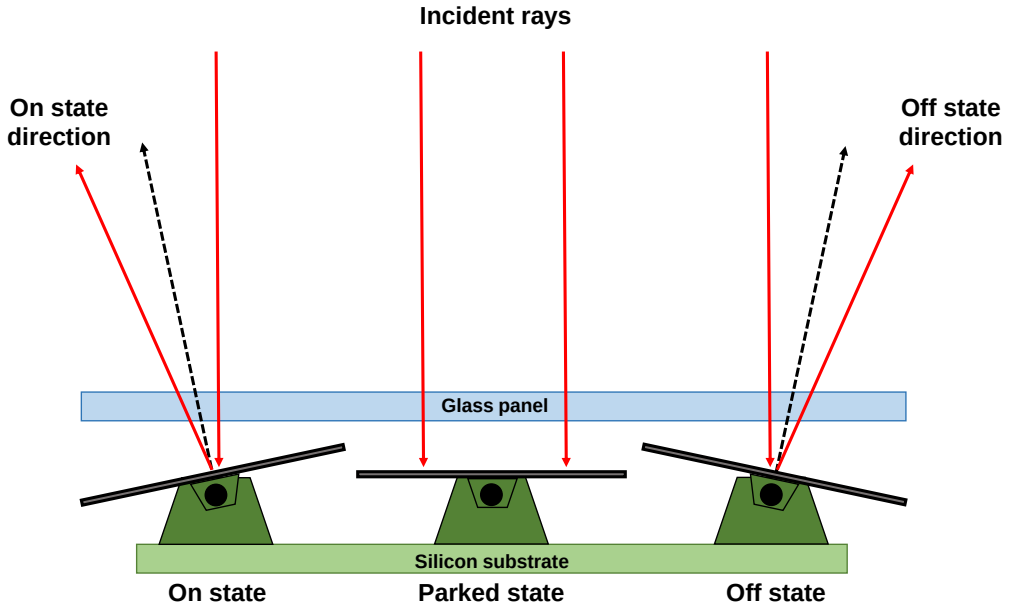


Fig. 1.6 A conceptual representation of the three possible mirror states: on; parked; and off.

powered off. Since the mirrors cannot be instructed to occupy the parked state as part of normal operation, mirrors in this state are not held at a specific angle. Thus the tilt angle of the mirrors in the parked state is only nominally parallel to the protective glass sheet. Figure 1.5 shows electron microscope images of the structure of a DMD screen[1.109;1.110], while Fig. 1.6 schematically illustrates the three states of the mirrors. To expand Eq. 1.36 to 2 dimensions the pulse train can be described for slowly varying phase by[1.111]

$$T(x,y) = \frac{1}{2} + \frac{1}{2}\text{sign}\{\cos[2\pi p(x,y)] - \cos[\pi\bar{\omega}(x,y)]\}. \tag{1.41}$$

In Eq. 1.41 the sign(x,y) function has been shifted by $1/2$ so that for all arguments the function behaves as

$$\frac{1}{2} + \frac{1}{2}\text{sign}(x,y) = \begin{cases} 1, & \text{for } x,y > 0 \\ 0, & \text{else} \end{cases}. \tag{1.42}$$

This function preserves the spatially-periodic nature of the binary pulse train. Once again consider an LG_1^0 beam, Fig. 1.7 illustrates the transmission function which creates this beam as given by Eq. 1.41. By setting mirrors on the DMD screen to the on state at positions corresponding to the peaks of the pulse train, both the phase and amplitude of the light can be modulated.

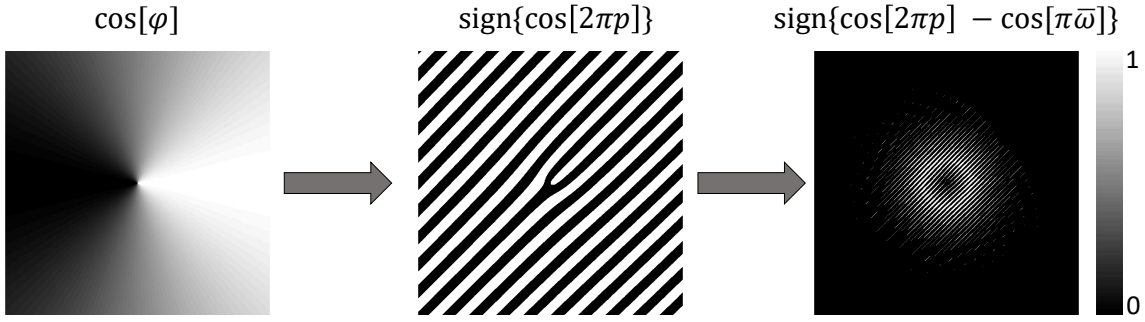


Fig. 1.7 The transmission function derived by Eq. 1.41 for an LG_1^0 beam. Note how in comparison to Fig. 1.3 the transmission function is binarised, i.e. equals either 0 or 1.

1.2 Laser brightness

The general equation for laser brightness is given by[1.112]

$$B = \frac{P}{\lambda^2 M_x^2 M_y^2}. \tag{1.43}$$

Here, B is the brightness, P is the power per unit surface area per unit solid angle (power density) and λ is the wavelength. M_x^2 and M_y^2 are the beam quality factors [1.113] in the x and y directions. The beam quality factor M_x^2 is defined by [1.31]

$$M_x^2 = \frac{\pi \omega_{0x} \theta_{0x}}{\lambda}, \tag{1.44}$$

where θ_{0x} is the half angle divergence and ω_{0x} is the beam waist. The waist is defined by the 2$^{\text{nd}}$ moment width of the beam and is given by

$$\omega_{0x} = 4\sqrt{\frac{\int_{-\infty}^{\infty}\int_{-\infty}^{\infty} I(x,y)(x-x_0)^2 dxdy}{\int_{-\infty}^{\infty}\int_{-\infty}^{\infty} I(x,y) dxdy}}, \tag{1.45}$$

with $I(x,y)$ being the intensity of the beam and x_0 its centroid. The intensity is given by

$$I(x,y) = E(x,y,z)E^*(x,y,z). \tag{1.46}$$

E^* denotes the complex conjugate of the beam E. The centroid x_0 is defined by

$$x_0 = \frac{\int_{-\infty}^{\infty}\int_{-\infty}^{\infty} I(x,y) x dxdy}{\int_{-\infty}^{\infty}\int_{-\infty}^{\infty} I(x,y) dxdy}. \tag{1.47}$$

The definition of M_y^2 is procedurally identical to that of M_x^2. For symmetric beams, Eq. 1.43 reduces to [1.114;1.31]

$$B = \frac{P}{\lambda^2 (M^2)^2}. \tag{1.48}$$

The M^2 affects two properties of beams. First, it can be used to express the size of a propagating beam $\omega(z)$ using the equation

$$\omega(z) = \sqrt{\omega_0^2 + \left(M^2\right)^2 \times (\lambda/(\pi\omega_0))(z-z_0)^2}, \tag{1.49}$$

for a beam with a waist ω_0 at the plane z_0. Second, for a beam with waist ω_0 the smallest waist size ω_f to which it can be focused by a lens of focal length f is given by

$$\omega_f = M^2 \frac{4\lambda f}{\pi \omega_0}. \tag{1.50}$$

The minimum value for M^2 is 1, and is only achieved by a Gaussian beam [1.113]. Equations 1.48, 1.49 and 1.50 provide two insights into laser brightness. First, to maximise brightness, the value of M^2 must minimised. The smaller the value of M^2, the less a beam will diverge as it propagates and the more tightly it can be focused, hence, the greater the

power density at some plane for a given input energy and, by extension, the greater the brightness. Second, the initial power density P must be made as large as possible. The remainder of this section introduces the relationship between the parameters M^2, P and structured light.

1.2.1 Effects of structured light on brightness

Structured light and M^2

Consider Eq. 1.45 and 1.47, since these equations explicitly depend on the intensity profile $I(x,y)$ of the beam, different beam types have different M^2 values. For common beam types, analytic solutions for the M^2 values are known in terms of the indices which define the beams[1.115;1.116;1.117;1.118]. Table 1.1 presents these solutions. Table. 1.1 shows that

Table 1.1 The M^2 values of common beam types with the mode indices shown in braces.

Profile (index)	$\boldsymbol{M^2}$
Super-Gaussian (k)	$0.5\sqrt{k}$
Hermite-Gaussian (m,n)	$2m+2n+1$
Laguerre-Gaussian (p, ℓ)	$2p+\lvert\ell\rvert+1$
Bessel-Gaussian (n,β)	$\sqrt{\left[1+n+\frac{\beta^2\omega_0^2}{4}\frac{i^{n+1}J_{n+1}\left(i\frac{\beta^2\omega_0^2}{4}\right)}{i^nJ_n\left(i\frac{\beta^2\omega_0^2}{4}\right)}\right]^2-\left(\frac{\beta^2\omega_0^2}{4}\right)^2}$
Airy(a_x,a_y)	$\sqrt{\frac{(3+8a_y^3+16a_y^6)a_x^2(a_x+a_y)+(3+8a_x^3+16a_x^6)a_y^2(a_x+a_y)}{64a_x^3a_y^3}}$

higher-order modes (those with higher indices) have higher M^2 values and so are less suitable for high brightness applications. Since the first four beam types given in Table. 1.1 have a Gaussian for their lowest order mode, they can be made to have an M^2 of 1 for their minimum indices $k=4$, $m=n=p=\ell=n=\beta=0$. By comparison, the Airy beam has a minimum $M^2=1.17$, for $a_x^3=a_y^3=\sqrt{3}/4$.

If a beam with a high initial $M^2=M_1^2$ could be losslessly transformed (i.e. maintaining P) into a beam with a lower $M^2=M_2^2$, the transformation would result in a brightness enhancement of

$$\eta=\left(\frac{M_1^2}{M_2^2}\right)^2, \tag{1.51}$$

for a given wavelength. If the initial mode is transformed back into a Gaussian beam Eq. 1.51 reduces to $\eta = M_1^4$. Hence, it is theoretically possible to significantly enhance the brightness by losslessly transforming a higher-order beam into a Gaussian beam.

Structured light and power density

To maximise brightness for a given M^2, the power density P must be maximised. This can be achieved by adding more energy to the lasing system. However, as a beam heats the medium through which it is propagating, the beam accrues a temperature-dependent phase and creates mechanical stress in the medium.

These thermal effects limit the energy which can be added to the system via two mechanisms. First, if the thermally-induced stress exceeds the mechanical fracture limit of the medium it will crack, rendering the optical system inoperable[1.119;1.120;1.121]. Second, before reaching mechanical failure, the phase aberrations introduced to the beam will significantly reduce its brightness. Recall Eq. 1.50, if a beam has an $M^2 = 1$, the size of the beam at the focal plane of a lens with focal length f_0 will be a minimum and so P will be maximised for a given input energy. However, if the beam contains an additional thermally-induced phase $\phi(x,t)$ which causes the beam to have an effective focal length f_1, it will no longer focus at the desired focal plane but will focus instead according to the compound focal length $(f_0 + f_1)/(f_0 f_1)$. Hence, P at the desired plane is reduced, even though a higher energy may be used[1.122;1.123;1.124]. This reduction in P is detrimental in industrial applications where a high on-axis energy density is required at a specified plane. Such applications include laser welding[1.3] and additive manufacturing processes (3D printing) which use a laser to melt or sinter materials[1.125;1.126].

The temperature profile of an illuminated optic and, by extension, the thermally-induced effects are described by the solution to the non-homogenous heat equation. Given the complexity of analytical time-dependent solutions to the heat equation, many previous works derive solutions under idealised thermal conditions, such as steady state temperature profiles[1.127;1.128;1.129;1.130;1.131], although some general analytical thermal solutions using Eigen-function analysis[1.132] and Green's functions[1.133;1.134] have been published. Additionally, the majority of research is directed at characterising the thermally-induced phase aberrations as a thermal lensing effect[1.131;1.133;1.135;1.136;1.137;1.138;1.139;1.140], with some general examinations of the thermally-induced phase available[1.128;1.141]. The growing use of lasers which produce structured light and the need for high brightness lasers has emphasised the need for more general characterisations of the thermal effects in high-

energy laser systems. Chapter 4 characterises the temperature profile in an illuminated optic by deriving a complete, analytic time-dependent solution to the non-homogeneous heat equation. This characterisation allows for an exploration of whether manipulation of the structure of light can be used to minimise both the thermal phase aberrations and thermal stress. If this is possible, the value of P, and, by extension, the brightness, can be maximised.

1.3 Simulating high energy laser sources

Optically induced thermal effects have been extensively studied, both theoretically[1.43;1.44;1.45;1.46] and experimentally[1.142;1.143], motivated by the quest for high brightness laser sources and the optimal delivery of such beams through optical systems. Since thermally-induced optical aberrations are predominantly observed in high power applications and take effect over short time scales, experimental verification is challenging and always limited to very specific test cases, such as when high power Gaussian beams pass through some medium (optical windows for example), or with solid-state lasers that output high power beams but suffer from deleterious thermal effects. Many approaches have been used to measure thermal aberrations both inside and external to lasers, including power monitoring[1.144], interferometric methods[1.8;1.9;1.10;1.128;1.131], lens based methods[1.135;1.136;1.137] and techniques using specialised equipment such as Shack-Hartman wavefront sensors[1.127;1.138;1.145;1.146]. Together with advances in measurement have been advances in aberration correction, most notably with adaptive optics[1.147;1.148;1.149]. However, high power laser studies involving the impact of thermal aberrations on structured light fields and the mitigation thereof remain largely neglected, due to the complexity of the experiments. The limited studies include thermal effects on Ince-Gaussian beams[1.150;1.151], Helmholtz-Gaussian beams[1.152] and Bessel-Gaussian beams[1.153], as well as some intra-cavity mode control with deformable mirrors[1.35;1.36;1.37;1.154;1.155;1.156]. It has also been demonstrated that annular pump beams can be used to reduce the thermal lensing effect on Gaussian beams passing through the centre of the optic[1.157;1.158]. Such annular pumps have been used to create high power annular structured light fields, for example, cylindrically symmetric vector vortex beams such as radially-polarized beams, and the scalar equivalent vortex beams carrying orbital angular momentum[1.159;1.160;1.161;1.162;1.163].

In principle the use of SLMs with CGHs is ideally suited to the experimental simulation of high-energy laser sources. This is because the reciprocal effect of a heated medium

on the beam is a phase-only perturbation. The flexibility and speed of DMDs would allow for the demonstration of the thermal effects in real-time. DMDs have gained in popularity of late [1.164] but they have yet to be used to simulate perturbing media, and in particular thermally-induced optical effects. By simulating the thermally-induced optical effects, the relationship between thermal aberrations and structured light can be fully explored in the laboratory without the need for specific optical materials and high-energy lasers. This significantly reduces the difficulty of high-energy laser experiments and accelerates the development of beam structures that yield the maximum possible brightness.

1.4 Outline of the dissertation

This work examines the relationship between structured light and laser brightness through three topics. First, manipulating the structure of beams with the aim of reducing their M^2. Second, structuring light to reduce the thermally-induced stress and thermally-induced phase aberrations with the aim of increasing power density. Third, using DMDs to create a fully configurable, low power experimental simulator of thermally-induced optical aberrations without the need for high laser powers.

Chapter 2 explores DMDs in depth, establishing their proper experimental implementation which is important for later chapters. The chapter resolves ambiguity in literature about the optical properties of DMDs. A full theoretical characterisation of the diffractive optical efficiency of DMDs is presented, and is verified experimentally. Techniques to ensure the creation of structured light having both the correct amplitude and phase profiles are explored in theory and confirmed through experimentation.

Chapter 3 examines the manipulation of structured light to reduce M^2. The chapter does this in two parts. First the general manipulation of structured light using LCoS SLMs is presented. A theoretical derivation is given detailing how to losslessly convert beams of one structure into beams of another structure, while explicitly controlling both their amplitude and phase. This theory is demonstrated experimentally with the conversion of Gaussian beams into non-propagation invariant beams of arbitrary structure. In the second part of the chapter this process is reversed and the non-propagation invariant beams are converted back into Gaussian beams. The effect of this transformation on the M^2 of the beam is calculated and verified experimentally.

Chapter 4 examines the effect of structured light on thermal stress, phase aberrations and

brightness. A complete time-dependent, analytical solution to the non-homogeneous heat equation is derived. This solution is then used to derive additional analytic solutions for the stress and phase aberrations introduced to a radially-symmetric optic. The interpretation of these solutions is discussed in detail as well. Further, this characterisation is used to determine if light can be structured to reduce thermal stress and phase aberrations and so enhance brightness. Finally, the DMD is reintroduced as a means of experimentally verifying the predictions of the theoretical solutions. In so doing, the possibility of using a DMD as an experimental simulator of high-energy laser sources is explored.

Chapter 5 presents a conclusion to the work and comments on its possible expansion in future.

References

1.1 R. G. Gould, "The laser, light amplification by stimulated emission of radiation," in *The Ann Arbor Conference on Optical Pumping, the University of Michigan*, vol. 15, no. 128, 1959, p. 92.

1.2 B. A. Lengyel, "Lasers: generation of light by stimulated emission," 1962.

1.3 J. F. Ready, *Industrial applications of lasers*. Elsevier, 1997.

1.4 A. K. Dubey and V. Yadava, "Laser beam machining—a review," *International Journal of Machine Tools and Manufacture*, vol. 48, no. 6, pp. 609–628, 2008.

1.5 R. L. Garwin, "How many orbiting lasers for boost-phase intercept?" *Nature*, vol. 315, no. 6017, pp. 286–290, 1985.

1.6 "Army awards laser weapon system contract." [Online]. Available: https://www.army.mil/article/225276/army_awards_laser_weapon_system_contract

1.7 F. Quelle, "Thermal distortion of diffraction-limited optical elements," *Applied Optics*, vol. 5, no. 4, pp. 633–637, 1966.

1.8 H. Welling and C. J. Bickart, "Spatial and temporal variation of the optical path length in flash-pumped laser rods," *Journal of the Optical Society of America*, vol. 56, no. 5, pp. 611–618, 1966.

1.9 G. Baldwin and E. Riedel, "Measurements of dynamic optical distortion in Nd-Doped glass laser rods," *Journal of Applied Physics*, vol. 38, no. 7, pp. 2726–2738, 1967.

1.10 J. Bradford and R. Eckardt, "Compensating for pump-induced distortion in glass laser rods," *Applied Optics*, vol. 7, no. 12, pp. 2418–2420, 1968.

1.11 J. Foster and L. Osterink, "Thermal effects in a Nd:YAG laser," *Journal of Applied Physics*, vol. 41, no. 9, pp. 3656–3663, 1970.

1.12 W. Koechner, "Thermal lensing in a Nd:YAG laser rod," *Applied Optics*, vol. 9, no. 11, pp. 2548–2553, 1970.

1.13 B. E. Cherrington, *Gaseous electronics and gas lasers*. Elsevier, 2014, vol. 94.

1.14 R. A. Young, "Chemically pumped molecular lasers," *The Journal of Chemical Physics*, vol. 40, no. 7, pp. 1848–1853, 1964.

1.15 M. Dzhidzhoev, V. T. Platonenko, and R. Khokhlov, "Chemical lasers," *Soviet Physics Uspekhi*, vol. 13, no. 2, p. 247, 1970.

1.16 F. P. Schäfer, W. Schmidt, and J. Volze, "Organic dye solution laser," *Applied Physics Letters*, vol. 9, no. 8, pp. 306–309, 1966.

1.17 E. Snitzer, "Proposed fiber cavities for optical masers," *Journal of Applied Physics*, vol. 32, no. 1, pp. 36–39, 1961.

1.18 R. Meant, L. Reekie, S. Poole, and D. Payne, "Neodymium-doped silica single-mode fibre laser," *Electron. Lett*, vol. 21, pp. 738–740, 1985.

1.19 W. J. Witteman, *The CO_2 laser*. Springer, 2013, vol. 53.

1.20 J. Powell, *CO_2 laser cutting*. Springer, 1993, vol. 214.

1.21 H. Abramczyk, *Introduction to laser spectroscopy*. Elsevier, 2005.

1.22 E. V. Dan'shchikov, V. Dymshakov, F. V. Lebedev, and A. Ryazanov, "Divergence of radiation from an electric-discharge CO_2 laser having an unstable resonator," *Soviet Journal of Quantum Electronics*, vol. 12, no. 8, p. 1013, 1982.

1.23 R. Maestle, W. Plass, J. Chen, C. Hembd-Soellner, A. Giesen, H. J. Tiziani, and H. Huegel, "Investigation of beam pointing stability, far-field divergence angle

and power density distribution of a high-power CO_2 laser," in *Third International Workshop on Laser Beam and Optics Characterization*, vol. 2870. International Society for Optics and Photonics, 1996, pp. 319–326.

1.24 F. P. Schafer, "Dye lasers," 1990.

1.25 F. J. Duarte, P. Kelley, L. W. Hillman, and P. F. Liao, *Dye laser principles: with applications*. Academic Press, 1990.

1.26 A. Kobyakov, M. Sauer, and D. Chowdhury, "Stimulated Brillouin scattering in optical fibers," *Advances in Optics and Photonics*, vol. 2, no. 1, pp. 1–59, 2010.

1.27 C. Jauregui, J. Limpert, and A. Tünnermann, "High-power fibre lasers," *Nature Photonics*, vol. 7, no. 11, pp. 861–867, 2013.

1.28 J. W. Dawson, M. J. Messerly, R. J. Beach, M. Y. Shverdin, E. A. Stappaerts, A. K. Sridharan, P. H. Pax, J. E. Heebner, C. W. Siders, and C. Barty, "Analysis of the scalability of diffraction-limited fiber lasers and amplifiers to high average power," *Optics Express*, vol. 16, no. 17, pp. 13 240–13 266, 2008.

1.29 T. Eidam, C. Wirth, C. Jauregui, F. Stutzki, F. Jansen, H.-J. Otto, O. Schmidt, T. Schreiber, J. Limpert, and A. Tünnermann, "Experimental observations of the threshold-like onset of mode instabilities in high power fiber amplifiers," *Optics Express*, vol. 19, no. 14, pp. 13 218–13 224, 2011.

1.30 N. Barré, M. Romanelli, and M. Brunel, "Role of cavity degeneracy for high-order mode excitation in end-pumped solid-state lasers," *Optics Letters*, vol. 39, no. 4, pp. 1022–1025, 2014.

1.31 D. Naidoo, I. A. Litvin, and A. Forbes, "Brightness enhancement in a solid-state laser by mode transformation," *Optica*, vol. 5, no. 7, pp. 836–843, 2018.

1.32 G. Machavariani, N. Davidson, A. Ishaaya, A. Friesem, and E. Hasman, "Efficient formation of a high-quality beam from a pure high-order Hermite-Gaussian mode," *Optics Letters*, vol. 27, no. 17, pp. 1501–1503, 2002.

1.33 S. Makki and J. Leger, "Solid-state laser resonators with diffractive optic thermal aberration correction," *IEEE Journal of Quantum Electronics*, vol. 35, no. 7, pp. 1075–1085, 1999.

1.34 S. Haddadi, O. Bouzid, M. Fromager, A. Hasnaoui, A. Harfouche, E. Cagniot, A. Forbes, and K. Aït-Ameur, "Structured Laguerre-Gaussian beams for mitigation of spherical aberration in tightly focused regimes," *Journal of Optics*, vol. 20, no. 4, p. 045602, 2018.

1.35 W. Lubeigt, M. Griffith, L. Laycock, and D. Burns, "Reduction of the time-to-full-brightness in solid-state lasers using intra-cavity adaptive optics," *Optics Express*, vol. 17, no. 14, pp. 12 057–12 069, 2009.

1.36 M. Gerber, T. Graf, and A. Kudryashov, "Generation of custom modes in a Nd:YAG laser with a semipassive bimorph adaptive mirror," *Applied Physics B*, vol. 83, no. 1, pp. 43–50, 2006.

1.37 W. Lubeigt, G. Valentine, J. Girkin, E. Bente, and D. Burns, "Active transverse mode control and optimisation of an all-solid-state laser using an intracavity adaptive-optic mirror," *Optics Express*, vol. 10, no. 13, pp. 550–555, 2002.

1.38 E. Cagniot, M. Fromager, T. Godin, N. Passilly, M. Brunel, and K. Ait-Ameur, "Variant of the method of Fox and Li dedicated to intracavity laser beam shaping," *Journal of the Optical Society of America A*, vol. 28, no. 3, pp. 489–495, 2011.

1.39 A. Hasnaoui and K. Ait-Ameur, "Properties of a laser cavity containing an absorbing ring," *Applied Optics*, vol. 49, no. 21, pp. 4034–4043, 2010.

1.40 R. de Saint Denis, N. Passilly, and K. Aït-Ameur, "Laser beam brightness of apertured optical resonators," *Optics Communications*, vol. 264, no. 1, pp. 193–202, 2006.

1.41 M. Damzen, R. Green, and K. Syed, "Self-adaptive solid-state laser oscillator formed by dynamic gain-grating holograms," *Optics Letters*, vol. 20, no. 16, pp. 1704–1706, 1995.

1.42 M. Innocenzi, H. Yura, C. Fincher, and R. Fields, "Thermal modeling of continuous-wave end-pumped solid-state lasers," *Applied Physics Letters*, vol. 56, no. 19, pp. 1831–1833, 1990.

1.43 L. Cini and J. Mackenzie, "Analytical thermal model for end-pumped solid-state lasers," *Applied Physics B*, vol. 123, no. 12, p. 273, 2017.

1.44 M. A. Isidro-Ojeda, J. J. Alvarado-Gil, V. S. Zanuto, M. L. Baesso, N. G. Astrath, and L. C. Malacarne, "Laser induced wavefront distortion in thick-disk material: An analytical description," *Optical Materials*, vol. 75, pp. 574–579, 2018.

1.45 L. C. Malacarne, N. G. Astrath, and M. L. Baesso, "Unified theoretical model for calculating laser-induced wavefront distortion in optical materials," *Journal of the Optical Society of America B*, vol. 29, no. 7, pp. 1772–1777, 2012.

1.46 L. C. Malacarne, N. G. Astrath, and L. S. Herculano, "Laser-induced wavefront distortion in optical materials: a general model," *Journal of the Optical Society of America B*, vol. 29, no. 12, pp. 3355–3359, 2012.

1.47 F. Dickey, "Laser beam shaping," *Optics and Photonics News*, vol. 26, no. 6, pp. 30–35, 2003.

1.48 H. Rubinsztein-Dunlop, A. Forbes, M. V. Berry, M. R. Dennis, D. L. Andrews, M. Mansuripur, C. Denz, C. Alpmann, P. Banzer, T. Bauer, E. Karimi, L. Marrucci, M. Padgett, M. Ritsch-Marte, N. M. Litchinitser, N. P. Bigelow, C. Rosales-Guzmán, A. Belmonte, J. P. Torres, T. W. Neely, M. Baker, R. Gordon, A. B. Stilgoe, J. Romero, A. G. White, R. Fickler, A. E. Willner, G. Xie, B. McMorran, and A. M. Weiner, "Roadmap on structured light," *Journal of Optics*, vol. 19, no. 1, p. 013001, 2017. [Online]. Available: http://stacks.iop.org/2040-8986/19/i=1/a=013001

1.49 A. Forbes, "Structured light: Tailored for purpose," *Optics and Photonics News*, vol. 31, no. 6, pp. 24–31, 2020.

1.50 M. de Oliveira, I. Nape, J. Pinnell, N. TabeBordbar, and A. Forbes, "Experimental high-dimensional quantum secret sharing with spin-orbit-structured photons," *Physical Review A*, vol. 101, no. 4, p. 042303, 2020.

1.51 A. Forbes and I. Nape, "Quantum mechanics with patterns of light: Progress in high dimensional and multidimensional entanglement with structured light," *AVS Quantum Science*, vol. 1, no. 1, p. 011701, 2019.

1.52 Y. Kashiwagi, T. Higashi, K. Obashi, Y. Sato, N. H. Komiyama, S. G. Grant, and S. Okabe, "Computational geometry analysis of dendritic spines by structured illumination microscopy," *Nature Communications*, vol. 10, no. 1, pp. 1–14, 2019.

1.53 M. Michihata, T. Hayashi, and Y. Takaya, "Measurement of axial and transverse trapping stiffness of optical tweezers in air using a radially polarized beam," *Applied Optics*, vol. 48, no. 32, pp. 6143–6151, Nov 2009.

1.54 Y. Kozawa and S. Sato, "Optical trapping of micrometer-sized dielectric particles by cylindrical vector beams," *Optics Express*, vol. 18, no. 10, pp. 10 828–10 833, 2010.

1.55 C. Rosales-Guzmán, N. Hermosa, A. Belmonte, and J. P. Torres, "Experimental detection of transverse particle movement with structured light," *Scientific Reports*, vol. 3, no. 1, pp. 1–5, 2013.

1.56 ——, "Measuring the translational and rotational velocities of particles in helical motion using structured light," *Optics Express*, vol. 22, no. 13, pp. 16 504–16 509, 2014.

1.57 J. Wang, J.-Y. Yang, I. M. Fazal, N. Ahmed, Y. Yan, H. Huang, Y. Ren, Y. Yue, S. Dolinar, M. Tur, and A. E. Willner, "Terabit free-space data transmission employing orbital angular momentum multiplexing," *Nature Photonics*, vol. 6, no. 7, p. 488, 2012.

1.58 J. T. Barreiro, T.-C. Wei, and P. G. Kwiat, "Beating the channel capacity limit for linear photonic superdense coding," *Nature Physics*, vol. 4, no. 4, pp. 282–286, 2008.

1.59 C. Rosales-Guzmán, B. Ndagano, and A. Forbes, "A review of complex vector light fields and their applications," *Journal of Optics*, vol. 20, no. 12, p. 123001, 2018. [Online]. Available: http://iopscience.iop.org/article/10.1088/2040-8986/aaeb7d

1.60 B. N. Chichkov, C. Momma, S. Nolte, F. Von Alvensleben, and A. Tünnermann, "Femtosecond, picosecond and nanosecond laser ablation of solids," *Applied Physics A*, vol. 63, no. 2, pp. 109–115, 1996.

1.61 A. M. Morales and C. M. Lieber, "A laser ablation method for the synthesis of crystalline semiconductor nanowires," *Science*, vol. 279, no. 5348, pp. 208–211, 1998.

1.62 M. Miyasaka and J. Stoemenos, "Excimer laser annealing of amorphous and solid-phase-crystallized silicon films," *Journal of Applied Physics*, vol. 86, no. 10, pp. 5556–5565, 1999.

1.63 D. B. Chrisey and G. K. Hubler, "Pulsed laser deposition of thin films," 1994.

1.64 K. Sugioka, M. Meunier, and A. Piqué, *Laser precision microfabrication*. Springer, 2010, vol. 135.

1.65 A. Forbes, "Structured light from lasers," *Laser & Photonics Reviews*, vol. 13, no. 11, p. 1900140, 2019.

1.66 D. Kim and J. Kim, "High Power TEM_{00} Mode Operation of Diode-Pumped Solid State Lasers," *Applied Physics B*, vol. 121, no. 3, pp. 401–405, 2015.

1.67 J. Kim, J. Mackenzie, J. Hayes, and W. Clarkson, "High power Er:YAG laser with radially-polarized Laguerre-Gaussian (LG_{01}) mode output," *Optics Express*, vol. 19, no. 15, pp. 14 526–14 531, 2011.

1.68 M. Okida, T. Omatsu, M. Itoh, and T. Yatagai, "Direct generation of high power Laguerre-Gaussian output from a diode-pumped Nd:YVO_4 1.3-μm bounce laser," *Optics Express*, vol. 15, no. 12, pp. 7616–7622, 2007.

1.69 M. L. Lukowski, J. T. Meyer, C. Hessenius, E. M. Wright, and M. Fallahi, "Generation of high-power spatially structured beams using vertical external cavity surface emitting lasers," *Optics Express*, vol. 25, no. 21, pp. 25 504–25 514, 2017.

1.70 P. Tuan, Y. Hsieh, Y. Lai, K. Huang, and Y. Chen, "Characterization and generation of high-power multi-axis vortex beams by using off-axis pumped degenerate cavities with external astigmatic mode converter," *Optics Express*, vol. 26, no. 16, pp. 20 481–20 491, 2018.

1.71 M. Eckerle, F. Beirow, T. Dietrich, F. Schaal, C. Pruss, W. Osten, N. Aubry, M. Perrier, J. Didierjean, X. Délen, F. Balembois, P. Georges, M. Ahmed Abdou, and T. Graf, "High-power single-stage single-crystal Yb:YAG fiber amplifier for radially polarized ultrashort laser pulses," *Applied Physics B*, vol. 123, no. 5, p. 139, 2017.

1.72 J.-P. Negel, A. Loescher, B. Dannecker, P. Oldorf, S. Reichel, R. Peters, M. A. Ahmed, and T. Graf, "Thin-disk multipass amplifier for fs pulses delivering 400 W of average and 2.0 GW of peak power for linear polarization as well as 235 W and 1.2 GW for radial polarization," *Applied Physics B*, vol. 123, no. 5, p. 156, 2017.

1.73 N. Heckenberg, R. McDuff, C. Smith, and A. White, "Generation of optical phase singularities by computer-generated holograms," *Optics Letters*, vol. 17, no. 3, pp. 221–223, 1992.

1.74 N. Heckenberg, R. McDuff, C. Smith, H. Rubinsztein-Dunlop, and M. Wegener, "Laser beams with phase singularities," *Optical and Quantum Electronics*, vol. 24, no. 9, pp. S951–S962, 1992.

1.75 M. Beijersbergen, R. Coerwinkel, M. Kristensen, and J. Woerdman, "Helical-wavefront laser beams produced with a spiral phaseplate," *Optics Communications*, vol. 112, no. 5-6, pp. 321–327, 1994.

1.76 G. Turnbull, D. Robertson, G. Smith, L. Allen, and M. Padgett, "The generation of free-space Laguerre-Gaussian modes at millimetre-wave frequencies by use of a spiral phaseplate," *Optics Communications*, vol. 127, no. 4-6, pp. 183–188, 1996.

1.77 G. D. Boyd and J. P. Gordon, "Confocal multimode resonator for millimeter through optical wavelength masers," *Bell System Technical Journal*, vol. 40, no. 2, pp. 489–508, 1961.

1.78 A. E. Siegman, "Laser beams and resonators: The 1960s," *IEEE Journal of Selected Topics in Quantum Electronics*, vol. 6, no. 6, pp. 1380–1388, 2000.

1.79 J. Durnin, "Exact solutions for nondiffracting beams. i. the scalar theory," *Journal of the Optical Society of America A*, vol. 4, no. 4, pp. 651–654, 1987.

1.80 F. Arscott, "XXI—The Whittaker-Hill Equation and the Wave Equation in Paraboloidal Co-ordinates," *Proceedings of the Royal Society of Edinburgh Section A: Mathematics*, vol. 67, no. 4, pp. 265–276, 1967.

1.81 M. A. Bandres and J. C. Gutiérrez-Vega, "Ince-Gaussian beams," *Optics Letters*, vol. 29, no. 2, pp. 144–146, 2004.

1.82 J. C. Gutiérrez-Vega, M. Iturbe-Castillo, and S. Chávez-Cerda, "Alternative formulation for invariant optical fields: Mathieu beams," *Optics Letters*, vol. 25, no. 20, pp. 1493–1495, 2000.

1.83 J. Gutiérrez-Vega, M. Iturbe-Castillo, G. Ramırez, E. Tepichın, R. Rodrıguez-Dagnino, S. Chávez-Cerda, and G. New, "Experimental demonstration of optical Mathieu beams," *Optics Communications*, vol. 195, no. 1-4, pp. 35–40, 2001.

1.84 C. Lopez-Mariscal, M. A. Bandres, and J. C. Gutierrez-Vega, "Observation of the experimental propagation properties of Helmholtz-Gauss beams," *Optical Engineering*, vol. 45, no. 6, p. 068001, 2006.

1.85 M. V. Berry and N. L. Balazs, "Nonspreading wave packets," *American Journal of Physics*, vol. 47, no. 3, pp. 264–267, 1979.

1.86 G. Sutton, "Properties of the Airy Beam," in *41st Plasmadynamics and Lasers Conference*, 1995, p. 4758.

1.87 G. Siviloglou, J. Broky, A. Dogariu, and D. Christodoulides, "Observation of accelerating Airy beams," *Physical Review Letters*, vol. 99, no. 21, p. 213901, 2007.

1.88 V. Arrizón, G. Méndez, and D. Sánchez-de La-Llave, "Accurate encoding of arbitrary complex fields with amplitude-only liquid crystal spatial light modulators," *Opt. Express*, vol. 13, no. 20, pp. 7913–7927, 2005.

1.89 G. N. Watson, *A treatise on the theory of Bessel functions*. Cambridge University Press, 1995.

1.90 G. Lazarev, P.-J. Chen, J. Strauss, N. Fontaine, and A. Forbes, "Beyond the display: Phase-only liquid crystal on silicon devices and their applications in photonics," *Optics Express*, vol. 27, no. 11, pp. 16 206–16 249, 2019.

1.91 A. Forbes, A. Dudley, and M. McLaren, "Creation and detection of optical modes with spatial light modulators," *Advances in Optics and Photonics*, vol. 8, pp. 200–227, 2016.

1.92 C. Rosales-Guzmán and A. Forbes, *How to shape light with spatial light modulators*. SPIE Press, 2017.

1.93 Q. Niu, C. Wang, and H. Shi, "Phase modulation characteristics analysis of liquid crystal spatial light modulator under oblique incidence," *Review of Scientific Instruments*, vol. 90, no. 5, p. 055001, 2019.

1.94 V. Calero, P. García-Martínez, J. Albero, M. M. Sánchez-López, and I. Moreno, "Liquid crystal spatial light modulator with very large phase modulation operating in high harmonic orders," *Optics Letters*, vol. 38, no. 22, pp. 4663–4666, 2013.

1.95 R.-G. Carmelo, H. Xiao-Bo, S. Adam, P. Moreno-Acosta, S. Franke-Arnold, R. Ramos-Garcia, and A. Forbes, "Polarisation-insensitive generation of complex vector modes from a digital micromirror device," *Scientific Reports (Nature Publisher Group)*, vol. 10, no. 1, 2020.

1.96 L. Gong, Y. Ren, W. Liu, M. Wang, M. Zhong, Z. Wang, and Y. Li, "Generation of cylindrically polarized vector vortex beams with digital micromirror device," *Journal of Applied Physics*, vol. 116, p. 183105, 2014.

1.97 K. J. Mitchell, S. Turtaev, M. J. Padgett, T. Čižmár, and D. B. Phillips, "High-speed spatial control of the intensity, phase and polarisation of vector beams using a digital micro-mirror device," *Optics Express*, vol. 24, no. 25, pp. 29 269–29 282, 2016.

1.98 Y.-X. Ren, Z.-X. Fang, L. Gong, K. Huang, Y. Chen, and R.-D. Lu, "Digital generation and control of Hermite-Gaussian modes with an amplitude digital micromirror device," *Journal of Optics*, vol. 17, no. 12, p. 125604, 2015.

1.99 J. Di, Y. Yu, Z. Wang, W. Qu, C. Y. Cheng, and J. Zhao, "Quantitative measurement of thermal lensing in diode-side-pumped Nd:YAG laser by use of digital holographic interferometry," *Optics Express*, vol. 24, no. 25, pp. 28 185–28 193, 2016.

1.100 Y.-X. Ren, Z.-X. Fang, L. Gong, K. Huang, Y. Chen, and R.-D. Lu, "Dynamic generation of Ince-Gaussian modes with a digital micromirror device," *Journal of Applied Physics*, vol. 117, no. 13, p. 133106, 2015.

1.101 X. Ding, Y. Ren, and R. Lu, "Shaping super-Gaussian beam through digital micromirror device," *Science China Physics, Mechanics & Astronomy*, vol. 58, no. 3, pp. 1–6, 2015.

1.102 Y.-X. Ren, R.-D. Lu, and L. Gong, "Tailoring light with a digital micromirror device," *Annalen der Physik*, vol. 527, no. 7-8, pp. 447–470, 2015.

1.103 A. O. Georgieva, A. V. Belashov, and N. V. Petrov, "Complex wavefront manipulation and holographic correction based on digital," in *Emerging Digital Micromirror Device Based Systems and Applications XII*, vol. 11294. International Society for Optics and Photonics, 2020, p. 112940B.

1.104 M. A. Cox, E. Toninelli, L. Cheng, M. J. Padgett, and A. Forbes, "A high-speed, wavelength invariant, single-pixel wavefront sensor with a digital micromirror device," *IEEE Access*, vol. 7, pp. 85 860–85 866, 2019.

1.105 Y. Chen, Z.-X. Fang, Y.-X. Ren, L. Gong, and R.-D. Lu, "Generation and characterization of a perfect vortex beam with a large topological charge through a digital micromirror device," *Applied Optics*, vol. 54, no. 27, pp. 8030–8035, 2015.

1.106 W. Liu, J. Fan, C. Xie, Y. Song, C. Gu, L. Chai, C. Wang, and M. Hu, "Programmable controlled mode-locked fiber laser using a digital micromirror device," *Optics Letters*, vol. 42, no. 10, pp. 1923–1926, 2017.

1.107 F. Schepers, T. Bexter, T. Hellwig, and C. Fallnich, "Selective Hermite-Gaussian mode excitation in a laser cavity by external pump beam shaping," *Applied Physics B*, vol. 125, no. 5, p. 75, 2019.

1.108 X. Hu, Q. Zhao, P. Yu, X. Li, Z. Wang, Y. Li, and L. Gong, "Dynamic shaping of orbital-angular-momentum beams for information encoding," *Optics Express*, vol. 26, no. 2, pp. 1796–1808, 2018.

1.109 "File:dlp cinema. a texas instruments technology - photo philippe binant.jpg — wikimedia commons, the free media repository." [Online]. Available: https://commons.wikimedia.org/w/index.php?title=File:DLP_CINEMA._A_Texas_Instruments_Technology_-_Photo_Philippe_Binant.jpg&oldid=224978671

1.110 J. D. Jackson, *Visual Analysis of a Texas Instruments Digital Micromirror Device*. The Institute of Optics, University of Rochester, 2019.

1.111 M. Mirhosseini, O. S. Magana-Loaiza, C. Chen, B. Rodenburg, M. Malik, and R. W. Boyd, "Rapid generation of light beams carrying orbital angular momentum," *Optics Express*, vol. 21, no. 25, pp. 30 196–30 203, 2013.

1.112 P. Shukla, J. Lawrence, and Y. Zhang, "Understanding laser beam brightness: A review and new prospective in material processing," *Optics & Laser Technology*, vol. 75, pp. 40–51, 2015.

1.113 A. E. Siegman, "Defining, measuring, and optimizing laser beam quality," in *Laser Resonators and Coherent Optics: Modeling, Technology, and Applications*, vol. 1868. International Society for Optics and Photonics, 1993, pp. 2–12.

1.114 A. Forbes, L. Burger, and I. A. Litvin, "Modeling laser brightness from cross porro prism resonators," in *Laser Beam Shaping VII*, vol. 6290. International Society for Optics and Photonics, 2006, p. 62900M.

1.115 A. Parent, M. Morin, and P. Lavigne, "Propagation of Super-Gaussian field distributions," *Optical and Quantum Electronics*, vol. 24, no. 9, pp. S1071–S1079, 1992.

1.116 S. Saghafi and C. Sheppard, "The beam propagation factor for higher order Gaussian beams," *Optics Communications*, vol. 153, no. 4-6, pp. 207–210, 1998.

1.117 R. Borghi and M. Santarsiero, "M^2 factor of Bessel-Gauss beams," *Optics Letters*, vol. 22, no. 5, pp. 262–264, 1997.

1.118 R.-P. Chen and C.-F. Ying, "Beam propagation factor of an Airy beam," *Journal of Optics*, vol. 13, no. 8, p. 085704, 2011.

1.119 A. K. Cousins, "Temperature and thermal stress scaling in finite-length end-pumped laser rods," *IEEE Journal of Quantum Electronics*, vol. 28, no. 4, pp. 1057–1069, 1992.

1.120 T. Fan, "Heat generation in Nd:YAG and Yb:YAG," *IEEE Journal of Quantum Electronics*, vol. 29, no. 6, pp. 1457–1459, 1993.

1.121 L. Yan and C. H. Lee, "Thermal effects in end-pumped Nd:phosphate glasses," *Journal of Applied Physics*, vol. 75, no. 3, pp. 1286–1292, 1994.

1.122 A. Siegman, "Analysis of laser beam quality degradation caused by quartic phase aberrations," *Applied Optics*, vol. 32, no. 30, pp. 5893–5901, 1993.

1.123 S. Chénais, F. Balembois, F. Druon, G. Lucas-Leclin, and P. Georges, "Thermal lensing in diode-pumped ytterbium lasers-part i: theoretical analysis and wavefront measurements," *IEEE Journal of Quantum electronics*, vol. 40, no. 9, pp. 1217–1234, 2004.

1.124 W. Koechner, *Solid-state laser engineering*. Springer, 2013, vol. 1.

1.125 K. Bartkowiak, S. Ullrich, T. Frick, and M. Schmidt, "New developments of laser processing aluminium alloys via additive manufacturing technique," *Physics Procedia*, vol. 12, pp. 393–401, 2011.

1.126 H. Bikas, P. Stavropoulos, and G. Chryssolouris, "Additive manufacturing methods and modelling approaches: a critical review," *The International Journal of Advanced Manufacturing Technology*, vol. 83, no. 1-4, pp. 389–405, 2016.

1.127 J. D. Mansell, J. Hennawi, E. K. Gustafson, M. M. Fejer, R. L. Byer, D. Clubley, S. Yoshida, and D. H. Reitze, "Evaluating the effect of transmissive optic thermal lensing on laser beam quality with a Shack-Hartmann wave-front sensor," *Applied Optics*, vol. 40, no. 3, pp. 366–374, 2001.

1.128 C. Pfistner, R. Weber, H. Weber, S. Merazzi, and R. Gruber, "Thermal beam distortions in end-pumped Nd:YAG, Nd:GSGG, and Nd:YLF rods," *IEEE Journal of Quantum Electronics*, vol. 30, no. 7, pp. 1605–1615, 1994.

1.129 Y.-F. Chen, C. Kao, T. Huang, C. Wang, and S. Wang, "Influence of thermal effect on output power optimization in fiber-coupled laser-diode end-pumped lasers," *IEEE Journal of Selected Topics in Quantum Electronics*, vol. 3, no. 1, pp. 29–34, 1997.

1.130 M. Schmid, T. Graf, and H. Weber, "Analytical model of the temperature distribution and the thermally induced birefringence in laser rods with cylindrically symmetric heating," *Journal of the Optical Society of America B*, vol. 17, no. 8, pp. 1398–1404, 2000.

1.131 W. Clarkson, "Thermal effects and their mitigation in end-pumped solid-state lasers," *Journal of Physics D: Applied Physics*, vol. 34, no. 16, p. 2381, 2001.

1.132 U. O. Farrukh, A. M. Buoncristiani, and C. E. Byvik, "An analysis of the temperature distribution in finite solid-state laser rods," *IEEE Journal of Quantum Electronics*, vol. 24, no. 11, pp. 2253–2263, 1988.

1.133 A. Forbes and L. R. Botha, "Physical optics modeling of intracavity thermal distortions in solid state laser resonators," in *Novel Optical Systems Design and Optimization V*, vol. 4768. International Society for Optics and Photonics, 2002, pp. 153–163.

1.134 E. Bernhardi, A. Forbes, C. Bollig, and M. D. Esser, "Estimation of thermal fracture limits in quasi-continuous-wave end-pumped lasers through a time-dependent analytical model," *Optics Express*, vol. 16, no. 15, pp. 11 115–11 123, 2008.

1.135 D. Burnham, "Simple measurement of thermal lensing effects in laser rods," *Applied Optics*, vol. 9, no. 7, pp. 1727–1728, 1970.

1.136 J. Murray, "Pulsed gain and thermal lensing of Nd:LiYF4," *IEEE Journal of Quantum Electronics*, vol. 19, no. 4, pp. 488–491, 1983.

1.137 B. Neuenschwander, R. Weber, and H. P. Weber, "Determination of the thermal lens in solid-state lasers with stable cavities," *IEEE Journal of Quantum Electronics*, vol. 31, no. 6, pp. 1082–1087, 1995.

1.138 P. Hardman, W. Clarkson, G. Friel, M. Pollnau, and D. Hanna, "Energy-transfer upconversion and thermal lensing in high-power end-pumped Nd:YLF laser crystals," *IEEE Journal of Quantum Electronics*, vol. 35, no. 4, pp. 647–655, 1999.

1.139 M. MacDonald, T. Graf, J. Balmer, and H. Weber, "Reducing thermal lensing in diode-pumped laser rods," *Optics Communications*, vol. 178, no. 4-6, pp. 383–393, 2000.

1.140 J. Blows, P. Dekker, P. Wang, J. Dawes, and T. Omatsu, "Thermal lensing measurements and thermal conductivity of Yb:YAB," *Applied Physics B*, vol. 76, no. 3, pp. 289–292, 2003.

1.141 J. Bourderionnet, A. Brignon, J.-P. Huignard, and R. Frey, "Influence of aberrations on fundamental mode of high power rod solid-state lasers," *Optics Communications*, vol. 204, no. 1-6, pp. 299–310, 2002.

1.142 A. J. Kemp, G. J. Valentine, and D. Burns, "Progress towards high-power, high-brightness neodymium-based thin-disk lasers," *Progress in Quantum Electronics*, vol. 28, no. 6, pp. 305–344, 2004.

1.143 M. Bass and W. Koechner, *Solid-State Lasers : A Graduate Text*. New Haven, CT, USA: Springer-Verlag, 2002. [Online]. Available: http://www.springer.de/phys/

1.144 D.-L. Kim and B.-T. Kim, "Laser output power losses in ceramic Nd:YAG lasers due to thermal effects," *Optik*, vol. 127, no. 20, pp. 9738–9742, 2016.

1.145 S. Chenais, F. Druon, F. Balembois, G. Lucas-Leclin, Y. Fichot, P. Georges, R. Gaume, B. Viana, G. Aka, and D. Vivien, "Thermal lensing measurements in diode-pumped Yb-doped GdCOB, YCOB, YSO, YAG and KGW," *Optical Materials*, vol. 22, no. 2, pp. 129–137, 2003.

1.146 V. V. Zelenogorsky, A. A. Solovyov, I. E. Kozhevatov, E. E. Kamenetsky, E. A. Rudenchik, O. V. Palashov, D. E. Silin, and E. A. Khazanov, "High-precision methods and devices for in situ measurements of thermally induced aberrations in optical elements," *Applied Optics*, vol. 45, no. 17, pp. 4092–4101, 2006.

1.147 Z. Zhu, Y. Li, J. Chen, J. Ma, and J. Chu, "Development of a unimorph deformable mirror with water cooling," *Optics Express*, vol. 25, no. 24, pp. 29 916–29 926, 2017.

1.148 T. Peng, C. Dai, J. Lou, Y. Cui, B. Tao, and J. Ma, "A low-cost deformable lens for correction of low-order aberrations," *Optics Communications*, vol. 460, p. 125209, 2020.

1.149 S. Piehler, T. Dietrich, P. Wittmüss, O. Sawodny, M. A. Ahmed, and T. Graf, "Deformable mirrors for intra-cavity use in high-power thin-disk lasers," *Optics Express*, vol. 25, no. 4, pp. 4254–4267, 2017.

1.150 H. Nadgaran and M. Servatkhah, "The effects of induced heat loads on the propagation of Ince-Gaussian beams," *Optics Communications*, vol. 284, no. 22, pp. 5329–5337, 2011.

1.151 M.-M. Zhang, S.-C. Bai, and J. Dong, "Effects of Cr4+ ions on forming Ince-Gaussian modes in passively Q-switched microchip solid-state lasers," *Laser Physics Letters*, vol. 16, no. 2, p. 025003, 2019.

1.152 H. Nadgaran and R. Fallah, "Investigation of the pump reshaping effect on the thermally-affected Helmholtz-Gauss beams generated by a solid-state laser," *Laser Physics*, vol. 25, no. 8, p. 085007, 2015.

1.153 M. Sabaeian and H. Nadgaran, "Bessel-Gauss beams: investigations of thermal effects on their generation," *Optics Communications*, vol. 281, no. 4, pp. 672–678, 2008.

1.154 T. Y. Cherezova, L. N. Kaptsov, and A. V. Kudryashov, "CW industrial rod YAG:Nd^{3+} laser with an intracavity active bimorph mirror," *Applied Optics*, vol. 35, no. 15, pp. 2554–2561, 1996.

1.155 T. Y. Cherezova, S. Chesnokov, L. Kaptsov, and A. Kudryashov, "Super-Gaussian laser intensity output formation by means of adaptive optics," *Optics Communications*, vol. 155, no. 1-3, pp. 99–106, 1998.

1.156 T. Y. Cherezova, S. S. Chesnokov, L. N. Kaptsov, V. V. Samarkin, and A. V. Kudryashov, "Active laser resonator performance: formation of a specified intensity output," *Applied Optics*, vol. 40, no. 33, pp. 6026–6033, 2001.

1.157 D. Kim, S. Noh, S. Ahn, and J. Kim, "Influence of a ring-shaped pump beam on temperature distribution and thermal lensing in end-pumped solid state lasers," *Optics Express*, vol. 25, no. 13, pp. 14 668–14 675, 2017.

1.158 D. Lin and W. Clarkson, "Reduced thermal lensing in an end-pumped Nd:YVO_4 laser using a ring-shaped pump beam," in *CLEO: Science and Innovations*. Optical Society of America, 2016, pp. SM3M–5.

1.159 T. Dietrich, M. Rumpel, T. Graf, and M. A. Ahmed, "Investigations on ring-shaped pumping distributions for the generation of beams with radial polarization in an Yb:YAG thin-disk laser," *Optics Express*, vol. 23, no. 20, pp. 26 651–26 659, 2015.

1.160 Z. Fang, K. Xia, Y. Yao, and J. Li, "Radially polarized and passively Q-switched Nd:YAG laser under annular-shaped pumping," *IEEE Journal of Selected Topics in Quantum Electronics*, vol. 21, no. 1, pp. 337–342, 2014.

1.161 T. Omatsu, K. Miyamoto, and A. J. Lee, "Wavelength-versatile optical vortex lasers," *Journal of Optics*, vol. 19, no. 12, p. 123002, 2017.

1.162 A. Forbes, "Controlling light's helicity at the source: orbital angular momentum states from lasers," *Philosophical Transactions of the Royal Society A*, vol. 375, no. 2087, p. 20150436, 2017.

1.163 Z. Fang, K. Xia, Y. Yao, and J. Li, "Radially polarized LG_{01}-mode Nd:YAG laser with annular pumping," *Applied Physics B*, vol. 117, no. 1, pp. 219–224, 2014.

1.164 S. Scholes, R. Kara, J. Pinnell, V. Rodríguez-Fajardo, and A. Forbes, "Structured light with digital micromirror devices: a guide to best practice," *Optical Engineering*, vol. 59, no. 4, p. 041202, 2019.

Chapter 2

Creating structured light with Digital Micro-mirror Devices

This chapter is based on the publication
***S. Scholes**, R. Kara, J. Pinnell, V. Rodríguez-Fajardo, and A. Forbes, "Structured light with digital micromirror devices: a guide to best practice," Optical Engineering, 59(4), p.041202, 2019.*
S.S derived the theoretical model and performed the experiments with R.K and J.P contributing to the latter. All authors contributed to the writing of the associated publication with supervision provided by author A.F.

The aim of this chapter is to establish the proper experimental implementation of DMDs. This is crucial to the implementation of DMDs as simulators for high-energy laser sources.

2.1 Digital Micro-mirror Devices

DMDs were developed by Larry Hornbeck during the 1980s[2.1] while working at Texas Instruments. Originally, DMDs were conceived in terms of a deformable mirror membrane but by 1993 research on this idea stopped in favour of using an array of individually addressable micro-mirrors. The developmental work on DMDs was aimed at creating an alternative to LCD technology in personal televisions[2.2]. Within a year the possibility of using DMDs in digital projection devices became apparent and the research was directed into developing DMDs for high resolution projection applications, such

as movie projectors[2.3;2.4]. By the turn of the century it was clear that DMDs could be used outside of their intended use case. Early work used a DMD to reconstruct digital holograms using interferometric fringes[2.5]. In 2003, D. Dudley presented a paper on *Emerging Digital Micromirror Device (DMD) Applications* in which topics from projection to lithography were given as potential applications[2.6]. The relatively low cost, rapid refresh rate and polarization invariance of DMDs makes them an attractive option for beam shaping applications. One such application was phase modulation by reverse phase contrast, in which the rapid refresh rate of the DMD in beam shaping applications was demonstrated[2.7]. By 2010, it was possible to use DMDs as a spatial light modulator with laser sources to produce novel intensity profiles of light. High precision laser beam shaping was demonstrated via the creation of flattop beams[2.8;2.9]. Around the same time, formalism on using general binary amplitude modulation algorithms to structure light was presented[2.10;2.11]. With this formalism in place, the role of DMDs as spatial light modulators was entrenched, expanding the possibilities for DMDs to create modes of structured light, such as LG and HG beams[2.12;2.13]. As the techniques to shape light using DMDs matured it was possible to create structured light in which more degrees of freedom were controlled. The creation of vector vortex beams by controlling the polarization of beams having Orbital Angular Momentum (OAM) has been demonstrated[2.14;2.15]. Further, DMDs have been used to characterise unknown optical fields[2.16]. In particular, DMDs have been used as Shack-Hartmann wavefront sensors[2.17], and in single pixel imaging systems[2.18;2.19;2.20]. As DMDs have become widespread in the beam shaping community, the need for their proper characterisation has become apparent. In 2017, work emerged comparing the beam shaping capabilities of DMDs and traditional liquid crystal type spatial light modulators[2.21]. This work shows that attention is now being focused on optimising the implementation of DMDs in the laboratory environment. A number of contradictions and omissions in the behaviour of DMDs are present in the work cited in this section. Many authors[2.6;2.9;2.12;2.16;2.22;2.23] characterise the diffractive properties of the DMD as a blaze type grating, while the other work cited above does not. The papers [2.7; 2.8; 2.9; 2.11; 2.12; 2.14; 2.16; 2.22; 2.24; 2.25; 2.26; 2.27; 2.28] present experimental setups in which the alignment of the DMDs is inconsistent with a blaze grating description, and does not seem to fully account for the true diffractive nature of the DMD.

Here the topic of the implementation of DMDs in experimental setups is addressed explicitly, providing an optical characterisation of DMDs that allows for the accurate prediction (and enhancement) of the diffractive optical efficiency of the DMD. Further,

techniques to ensure the creation of structured beams with the correct amplitude and phase profiles are presented. This analysis establishes the proper experimental use of DMDs, which is foundational to their use in Chp 4.

At the time of writing, DMDs are manufactured under the name Digital Light Projection (DLP), a trademark of Texas Instruments (TI). The DMDs are manufactured as chipsets which are then sold on, either by third party suppliers such as Mouser and Vialux, or the chipsets can be purchased directly from TI in evaluation modules. Regardless of the means of procurement, currently all DMDs are manufactured by TI. Two distinct variants of DMD are available: those with Cartesian mirror layouts and those with diamond like mirror layouts. In the case of the TI 6500 DMD, the mirrors are arranged in a Cartesian grid. The mirrors pivot about their hypotenuse, thus directing light diagonally away from the DMD at twice the incident angle of the beam. By contrast, for the TI 3000 series DMD, in order for the mirrors to tilt using a hinge mounted along the hypotenuse of each mirror but still have the reflected light be coplanar with the surface on which the DMD is mounted, the mirrors are rotated 45° with respect to the optical axis. This rotation causes the square mirrors to appear as diamonds. To achieve optimal packing, these diamonds are arranged with their centres twice as far apart horizontally as vertically. In this chapter, both a DLP 3000 220 DMD and a DLP 6500 FYE DMD are examined, thus covering the mirror configurations of all currently available DMDs.

2.2 Diffractive properties of DMDs

2.2.1 The DMD as a blaze grating

A blaze grating is a type of diffraction grating designed to direct the maximum possible amount of light into a specific diffraction order. When this occurs that diffraction order is said to be 'blazed'. These gratings are identified by 'sawtooth' type structures on their surface, as shown in Fig. 2.1. Since the mirrors of the DMD in the on state resemble such a structure many publications (see Sec. 2.1) assume the DMD has the diffractive properties of a blaze grating. A blaze grating is characterised by 5 parameters: the grating number N (typically expressed as lines per mm), θ_B the tilt angle of the blaze grating, θ_i the incident angle of the light, m the order to be blazed and λ the wavelength of the incident light [2.29]. The relationship between these parameters is given by

$$\lambda = \frac{2}{Nm}\sin(\theta_B)\cos(\theta_i - \theta_B), \tag{2.1}$$

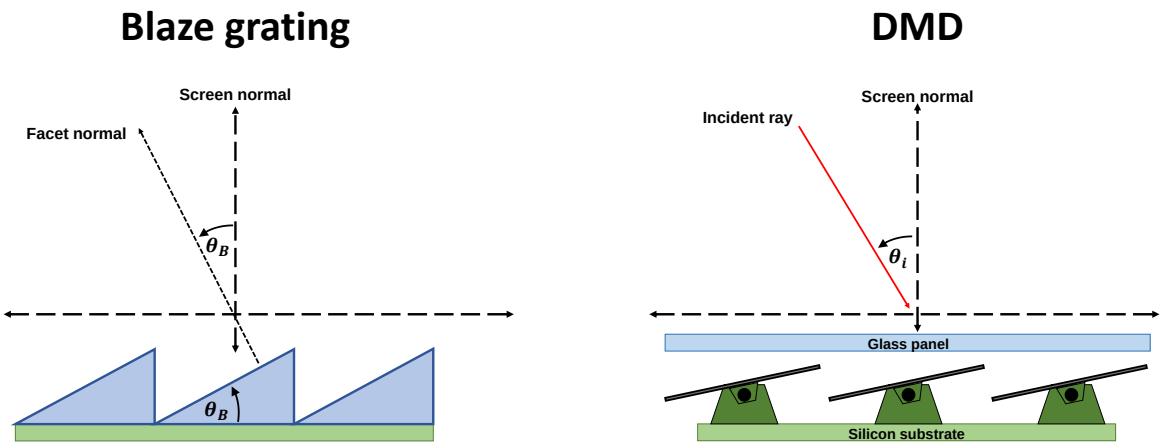


Fig. 2.1 A comparison between a blaze grating (left) and a DMD with the mirrors in the on state (right). The tilt angle θ_B and the incident angle θ_i are measured relative to the screen normal of the DMD with counter-clockwise as the positive direction.

where the angles are measured relative to the screen normal of the DMD, with counter-clockwise as the positive direction. For a given N, θ_i and θ_B, a given order m will only be blazed for a specific wavelength λ_B, referred to as the 'blaze wavelength'. On a DMD the tilt angle θ_B is fixed, as is the incident wavelength. Thus, the only parameter which can be adjusted to blaze a given order m is the incident angle θ_i. Figure 2.2 shows the wavelength required to blaze the first 3 diffraction orders as a function of incident

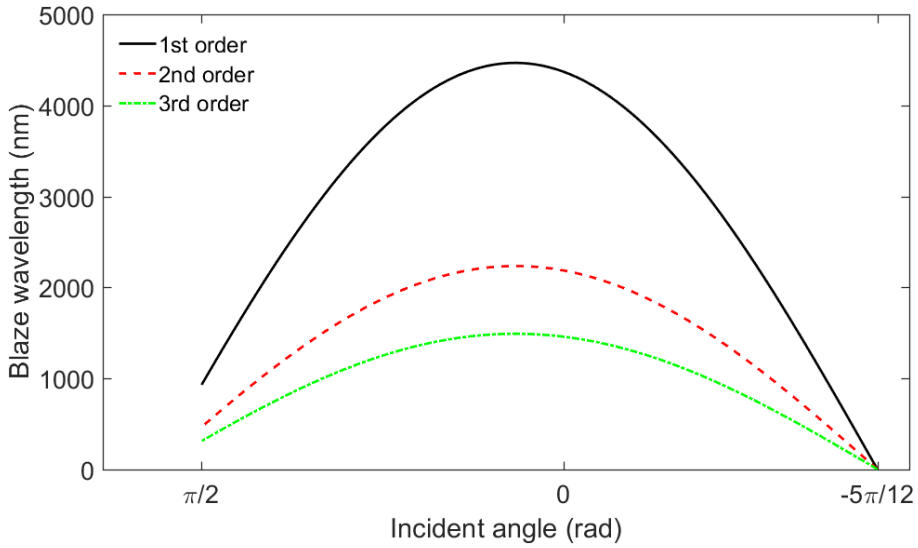


Fig. 2.2 The incident wavelength required to blaze the 1st, 2nd and 3rd order diffractions as a function of incident angle for a mirror tilt angle of $\theta_B = \pi/15$ and $N = 1/7.6 \times 10^{-3}$.

angle for the 3000 series DMD. The mirror tilt angle is $\theta_B = \pi/15$ (rad) and $N = 1/7.6 \times 10^{-3}$ (mm^{-1}). Equation 2.1 predicts that for an incident HeNe laser, the incident angle required to blaze the first order is beyond $-5\pi/12$ rad ($-75°$). Further, for an incident HeNe beam the difference between the incident angle which blazes the first diffraction order θ_1 and the incident angle which blazes the second diffraction order θ_2 is less than 1 milli-radian. Consequently, aligning the DMD to blaze the first diffraction order for an incident HeNe beam would be difficult in the laboratory environment, but could be feasible for mid-infrared sources where the required incident angle is smaller. Thus, although the DMD could be made to act as a blaze grating for sufficiently long wavelengths, when implemented with visible spectrum sources, an alternative model must be used to determine the diffractive properties of the device.

2.2.2 The DMD as a modified amplitude grating

The diffractive properties of the DMD are described first as a reflective binary amplitude-only grating, and then this over-simplified description is modified to account for the incident angle of the illuminating beam. To formulate the diffractive model, a Fraunhoffer diffraction analysis is performed. This analysis is valid if the Fresnel number $\hat{F} << 1$. The Fresnel number is given by

$$\hat{F} = \frac{A}{\lambda z}, \tag{2.2}$$

for a wavelength λ, area A and propagation distance z. For a TI 3000 DMD and HeNe source

$$\begin{aligned} \hat{F} &= \frac{(7.6 \times 10^{-6})^2}{632.8 \times 10^{-9} z}, \\ \hat{F} &= \frac{9.1 \times 10^{-5}}{z}. \end{aligned} \tag{2.3}$$

Hence for $z > 9.1 \times 10^{-2}$ the diffractive properties of the DMD can be understood in terms of Fraunhoffer diffraction. The following conventions are applied: a square region of the screen is considered and a local coordinate system within this region established. This coordinate system may be rotated such that the mirrors in the array always appear as squares; the incident illumination is assumed to be normal to the mirror array, since for an amplitude-only grating a non-normal incident angle only serves to displace the entire diffraction pattern laterally in space, leaving the relative intensities of the diffraction orders unchanged. Within the region of interest, each mirror of width w can be described

by the function rect(x, w) where rect(x, w) is defined as

$$\text{rect}(x,w) = \begin{cases} 1, & \text{for } |\frac{x}{w}| < \frac{1}{2} \\ 0.5, & \text{for } |\frac{x}{w}| = \frac{1}{2} \\ 0, & \text{otherwise} \end{cases}. \tag{2.4}$$

To expand this to an array of mirrors, the rect function is convolved with a comb function,

$$\text{comb}(x,\Delta) = \sum_{m=-\infty}^{m=\infty} \delta(x - \frac{m}{\Delta}) = \begin{cases} \infty, & \text{for } x = \frac{m}{\Delta} \\ 0, & \text{otherwise} \end{cases}, \tag{2.5}$$

where Δ is the spacing between mirror centres, such that $\Delta > w$ since there are small gaps between the mirrors. To bound the array, the convolution is multiplied by an additional rect function that has the width of the region of interest. The width of the screen can be written as the number of mirrors, N, multiplied by the mirror spacing Δ. Thus the full transmission function in two dimensions for the DMD screen is

$$T(X',Y') = \left[\text{rect}\left(\frac{X'}{w}\right)\text{rect}\left(\frac{Y'}{w}\right) \otimes \frac{1}{\Delta}\text{comb}\left(\frac{X'}{\Delta}\right)\frac{1}{\Delta}\text{comb}\left(\frac{Y'}{\Delta}\right)\right] \cdot \text{rect}\left(\frac{X'}{N\Delta}\right)\text{rect}\left(\frac{Y'}{N\Delta}\right). \tag{2.6}$$

Here $\otimes$ represents the convolution operator with X' and Y' representing the local coordinate system. This function is separable and can be written as

$$\begin{aligned} T(X') &= \left[\text{rect}\left(\frac{X'}{w}\right) \otimes \frac{1}{\Delta}\text{comb}\left(\frac{X'}{\Delta}\right)\right] \cdot \text{rect}\left(\frac{X'}{N\Delta}\right), \\ T(Y') &= \left[\text{rect}\left(\frac{Y'}{w}\right) \otimes \frac{1}{\Delta}\text{comb}\left(\frac{Y'}{\Delta}\right)\right] \cdot \text{rect}\left(\frac{Y'}{N\Delta}\right). \end{aligned} \tag{2.7}$$

The Fourier transform $\mathscr{F}$ is defined for a function $f(x')$ by

$$\mathscr{F}[f(x')] = \int_{-\infty}^{\infty} f(x')\exp(-i2\pi f_{x'}x')dx'. \tag{2.8}$$

Applying the Fourier transform to Eq. 2.6 gives

$$\mathscr{F}(f_{x'}) = \mathscr{F}[T(X')] = \left[w\,\text{sinc}(wf_{x'}) \cdot \sum_{m=-\infty}^{m=\infty} \delta\left(x - \frac{m}{\Delta}\right)\right] \otimes N\Delta\,\text{sinc}(N\Delta f_{x'}), \tag{2.9}$$

with

$$\text{sinc}(\chi) = \frac{\sin(\pi\chi)}{\pi\chi}. \tag{2.10}$$

Here χ is a placeholder for the argument in the sinc() function. Applying the Whittaker-Shannon Sampling Theorem [2.30] the solution can be further simplified to

$$\mathscr{F}(f_{x'}) = \sum_{m=-\infty}^{m=\infty} w\,\mathrm{sinc}\left(w\frac{m}{\Delta}\right) N\Delta\,\mathrm{sinc}\left[N\Delta\left(f_{x'} - \frac{m}{\Delta}\right)\right] \tag{2.11}$$

and

$$\mathscr{F}(f_{y'}) = \sum_{m=-\infty}^{m=\infty} w\,\mathrm{sinc}\left(w\frac{m}{\Delta}\right) N\Delta\,\mathrm{sinc}\left[N\Delta\left(f_{y'} - \frac{m}{\Delta}\right)\right]. \tag{2.12}$$

Thus the Fraunhofer diffraction pattern intensity $I(x', y')$ is given by

$$I(x', y') = \left(\frac{w^2N^2\Delta^2}{\lambda z}\right)^2 \left\{\sum_{m=-\infty}^{m=\infty} \mathrm{sinc}\left(w\frac{m}{\Delta}\right)\mathrm{sinc}\left[N\Delta\left(\frac{x'}{\lambda z} - \frac{m}{\Delta}\right)\right]\right\}^2 \times \left\{\sum_{m=-\infty}^{m=\infty} \mathrm{sinc}\left(w\frac{m}{\Delta}\right)\mathrm{sinc}\left[N\Delta\left(\frac{y'}{\lambda z} - \frac{m}{\Delta}\right)\right]\right\}^2, \tag{2.13}$$

where

$$\begin{aligned} x' &= \frac{x-y}{\sqrt{2}}, \\ y' &= \frac{x+y}{\sqrt{2}}. \end{aligned} \tag{2.14}$$

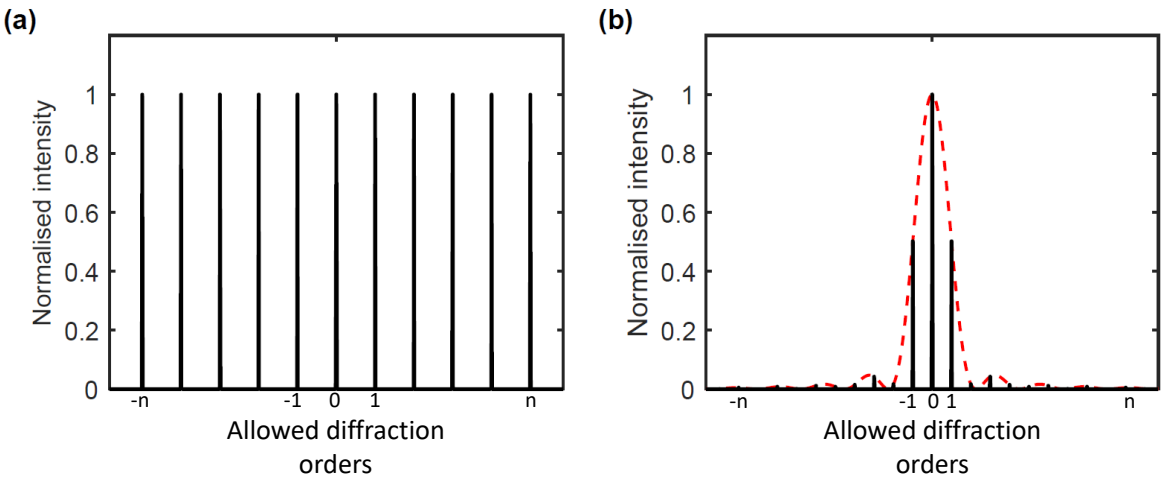


Fig. 2.3 (a) The set of diffraction peaks allowed by the second sinc factor in each summation. (b) Shows how the envelope function (in red) defined by $\mathrm{sinc}(w\frac{m}{\Delta})$ modulates the intensity of the allowed peaks to produce the observed diffraction pattern.

The diffraction pattern has two key elements: the allowed diffraction peaks, given by the second factor in each summation $\text{sinc}\{N\Delta[x'/(\lambda z) - m/\Delta]\}$; and the relative intensities given by the first factor in each summation $\text{sinc}(wm/\Delta)$. Figure 2.3 shows how these terms work together to predict a diffraction pattern. Equation 2.13 allows for the expression of the diffraction efficiency of the n^{th} order from the DMD as the weighting of the envelope function for the n^{th} term relative to every other term.

$$\text{eff}_n = \frac{\text{sinc}(w\frac{n}{\Delta})^4}{\left[\sum_{m=-\infty}^{m=\infty} \text{sinc}(w\frac{m}{\Delta})\right]^4}. \tag{2.15}$$

The efficiency given in Eq. 2.15 is highly sensitive to the values chosen for w and Δ. For the TI 3000 DMD the manufacturer states $w = 7.6\ \mu$m, but the mirror spacing $\Delta = w + \epsilon$

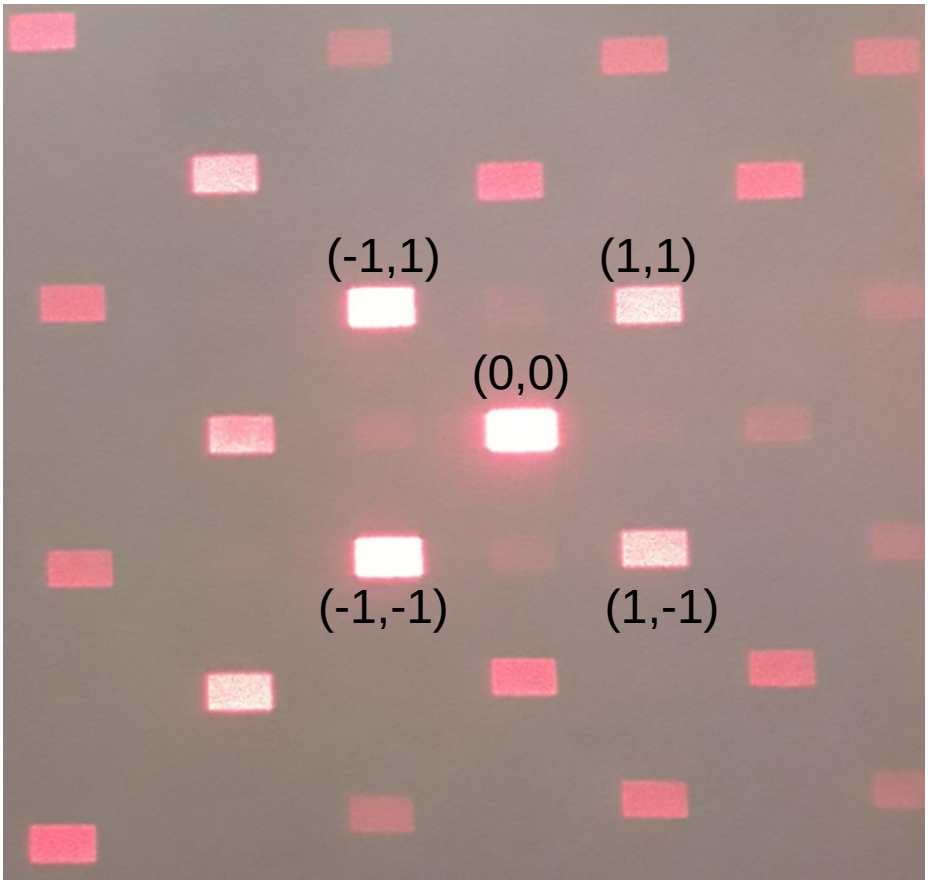


Fig. 2.4 The observed diffraction pattern for the TI 3000 DMD aligned at an incident angle of 0 rad with all mirrors in the on state. Note that the diffraction orders labelled $(-1,1)$ and $(-1,-1)$ are brighter than those labelled $(1,1)$ and $(1,-1)$.

is proprietary information. Unpublished sources state the value of ϵ as between 0.8 and 1 μm. With these values the efficiency of the DMD is predicted to be between 61% and 67%. Consider Fig. 2.4 which shows the observed diffraction pattern for the TI 3000 DMD aligned at an incident angle of 0 rad with all mirrors in the on state. Note that the diffraction orders labelled $(-1,1)$ and $(-1,-1)$ are brighter than those labelled $(1,1)$ and $(1,-1)$. This observation indicates that Eq. 2.13 is an incomplete description of the system. If Eq. 2.13 were complete, the intensity of the orders around the $(0,0)$ order would be symmetric since a change in the angle of the mirrors is equivalent to a change in the incident angle of the illuminating beam. To account for this behaviour Eq. 2.13 is modified by decoupling the envelope function $\text{sinc}(wm/\Delta)$ from the zero order diffraction peak given by the term $\text{sinc}\{N\Delta[x'/(\lambda z) - m/\Delta]\}$. The envelope function becomes

$$\text{sinc}\left[w\frac{m+\sin(2\theta_B)+\sin(\theta_i)}{\Delta}\right], \tag{2.16}$$

where θ_B and θ_i have the same meaning as in Eq. 2.1, with positive angles measured anti-clockwise relative to the screen normal. This formulation treats the DMD as a modified amplitude grating. The relative positions of the diffraction orders are governed by the physical structure of the DMD screen, while the relative intensity of the orders is governed by the incident angle of the light and the mirror angle. Figure 2.5 shows how this decou-

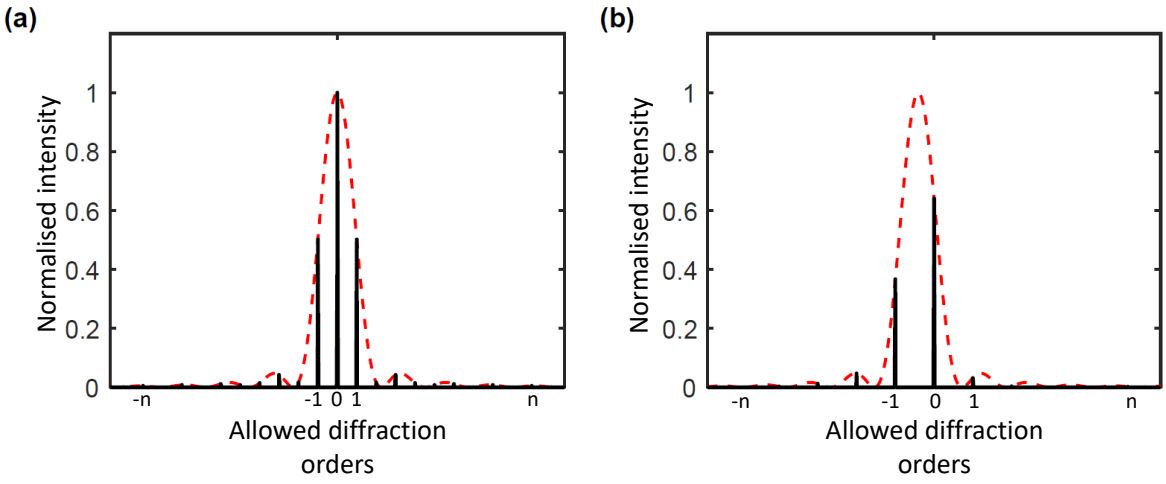


Fig. 2.5 (a) The relationship between the envelope function (in red) and the allowed diffraction orders for a pure amplitude grating. Note how in (a) the envelope function is fixed around the zero order diffraction peak. (b) The effect of decoupling the envelope function from the zero order. Energy can now be moved into the first order diffraction without changing the relative positions of the orders in space.

pling of the envelope term affects the relative intensities of the diffraction orders. When the mirrors are set to the on state the envelope function moves off the zero diffraction order, resulting in additional energy in the diffraction orders which lie in the direction of the on state.

When used as a beam shaping device, a hologram is displayed on the DMD. This hologram has an additional diffraction grating encoded into it, as explained in Sec. 1.1.1. This encoded grating is a binary amplitude grating because it consists of alternating regions of on state and off state mirrors. This 'holographic grating' separates the inherent zero order diffraction of the DMD into many beams. Within this set of diffracted beams the desired structured beam forms in the first order (Fig. 1.3). Each region of the encoded grating has a width ϖ. The on state mirrors direct light toward a detector while the off state mirrors direct it away. The total transmission function, $T(X',Y')_{\text{Tot}}$ is the interaction between the DMD and the holographic grating. For perfectly reflective mirrors the transmission function is

$$T(X',Y')_{\text{Tot}} = T(X',Y')_{\text{DMD}} \otimes \left[\text{rect}\left(X', \frac{\varpi}{2}\right)\right]. \tag{2.17}$$

The corresponding intensity pattern is

$$I(x',y') = \left[\frac{\varpi}{2}\,\text{sinc}\left(\frac{\varpi x'}{2\lambda z}\right)\right]^2 \cdot T(X',Y')_{\text{DMD}}. \tag{2.18}$$

The efficiency of the DMD with a holographic grating displayed can be calculated as the product of the DMD efficiency and the efficiency of a binary amplitude grating

$$\text{eff}_n = \frac{\text{sinc}\left[w\frac{n+\sin(2\theta_B)+\sin(\theta_i)}{\Delta}\right]^4}{\left\{\sum_{m=-\infty}^{m=\infty}\text{sinc}\left[w\frac{m+\sin(2\theta_B)+\sin(\theta_i)}{\Delta}\right]\right\}^4} \cdot \left[\frac{1}{2}\,\text{sinc}\left(\frac{n}{2}\right)\right]^2. \tag{2.19}$$

Equation 2.19 predicts that the first order diffraction from the holographic grating, which is typically what is measured experimentally, will have an efficiency of at best $\approx 6\%$. Finally, if a hologram is displayed which not only has an encoded diffraction grating but also a spatial structure which sets additional mirrors to the off state, such as the holograms created by complex amplitude modulation, the intensity of the first order decreases. Complex amplitude modulation holograms set the states of the mirrors based on the amplitude $A(x,y)$ of the desired beam. As a result these holograms set mirrors which

would be in the on state (for only a grating) to the off state. The effect of this is a decrease in the functional efficiency of the device since less light is directed into the first order.

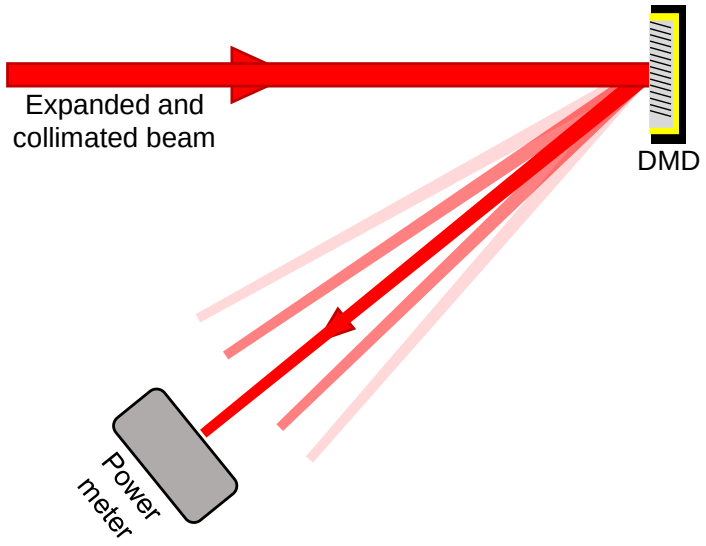


Fig. 2.6 The experimental setup used to verify the treatment of the DMD presented in Sec. 2.2.2. An expanded and collimated beam was incident onto a DMD and the power of the relevant diffraction order was measured by a power meter.

2.2.3 DMD efficiency measured experimentally

To verify the validity of the theoretical treatment of the DMD in Sec. 2.2.2, the experimental setup in Fig. 2.6 was constructed. The beam was expanded and collimated by means of a microscope objective and collimating lens. The DMD used was the TI 3000. The total incident power, and the power transmitted into the relevant diffractive orders was measured using a ThorLabs S121C power meter. A total of five measurements were taken. The first three were of the zero order diffraction without a hologram displayed. They were: the mirrors in the on state, with the DMD aligned at 0 rad; the mirrors in the on state, with the DMD aligned at $\pi/15$ rad; and the mirrors in the parked state, with the DMD aligned at $\pi/15$ rad. Next, the efficiency of the first order diffraction from a holographic grating was measured with the DMD aligned at $\pi/15$ rad. The results for these four measurements are presented in Table 2.1. Lastly, the effect of encoding an aperture onto the holographic grating was measured. The size of the encoded aperture was adjusted from 0.2 mm to 1.895 mm resulting in a change in the number of mirrors in the on state. Figure 2.7 shows the relationship between the aperture radius (number of on state mirrors) and the

efficiency of the first order. Table 2.1 reveals three things. First, when the mirrors are in the

Table 2.1 Diffraction efficiency of the TI 3000 DMD.

Order measured	**Mirror state**	**DMD alignment (rad)$\pm\pi/180$**	**Theoretical efficiency (%)**	**Measured efficiency (%)$\pm$2.1**
0^{th}	on	0	25.7	32.9
0^{th}	on	$\pi/15$	50.4	52.9
0^{th}	parked	$\pi/15$	61.9	60.3
1^{st} holographic order	on	$\pi/15$	5.1	5.0

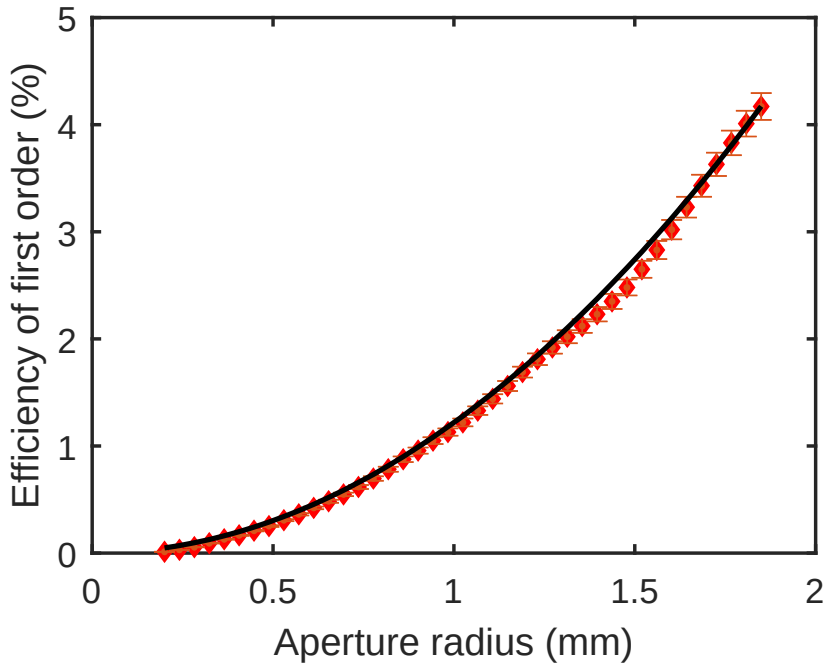


Fig. 2.7 Efficiency of the first order holographic diffraction as a function of aperture radius. The black line is predicted by Eq. 2.19 based on the number of mirrors in the on state in the hologram. The red diamonds are the experimentally measured values.

parked state the DMD does behave as an unmodified amplitude-only diffraction grating. In this configuration the measured efficiency is in close agreement with the predictions of Eq. 2.15. Second, when the mirrors are in the on state the DMD behaves as a modified amplitude-only grating, meaning the diffractive efficiency is a function of the incident angle of the beam, as described by Eq. 2.16. The first two results in Table 2.1 show that the diffractive efficiency of the DMD can be enhanced by aligning it such that the off

state mirrors are normal to the incident light. For the TI 3000 DMD this corresponds to an alignment angle of $\pi/15$ rad. By doing so the envelope function given by Eq. 2.16 is moved partially back over the zero diffraction order, increasing the energy in that order. Third, when the off state mirrors are normal to the incident light, the effective efficiency of the device is then related to the hologram it is displaying (Eq. 2.19) and the number of mirrors in the on state (Fig. 2.7). The analysis presented in this section does not assume the DMD is being used to generate any specific structure of light, but instead characterises the general diffractive efficiency. Thus alignment of the off state mirrors perpendicular to the incident beam will improve the optical efficiency of a DMD in all use cases.

2.3 Generating high fidelity modes with the DMD

Section 2.2.3 presents an alignment regime that optimises the diffractive efficiency of DMDs. This section shows that this alignment regime does not reduce the ability of the DMD to generate high fidelity modes of structured light. A high fidelity beam is one in which both the amplitude and phase profiles of the beam closely match the ideal theoretical field . This section provides recommendations for ensuring the greatest accuracy of both of these beam properties.

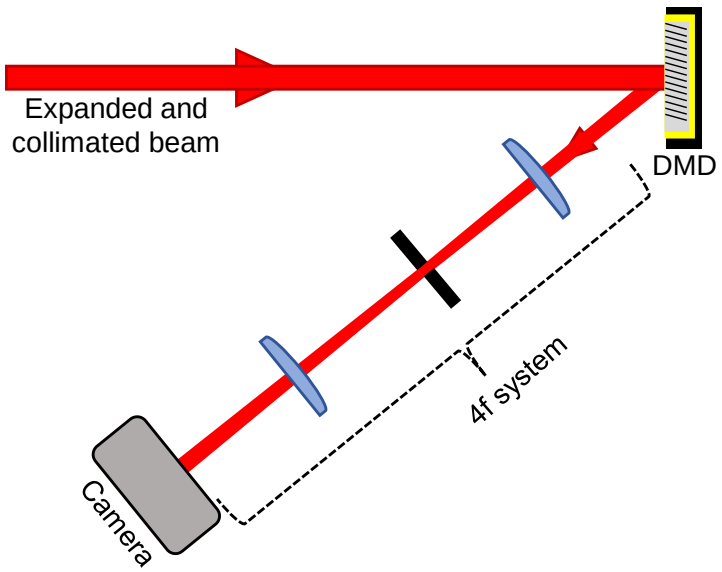


Fig. 2.8 To determine the mode quality, an expanded and collimated beam was incident on a 3000 series DMD. The holographic first order diffraction was then imaged, via a 4f system to a camera.

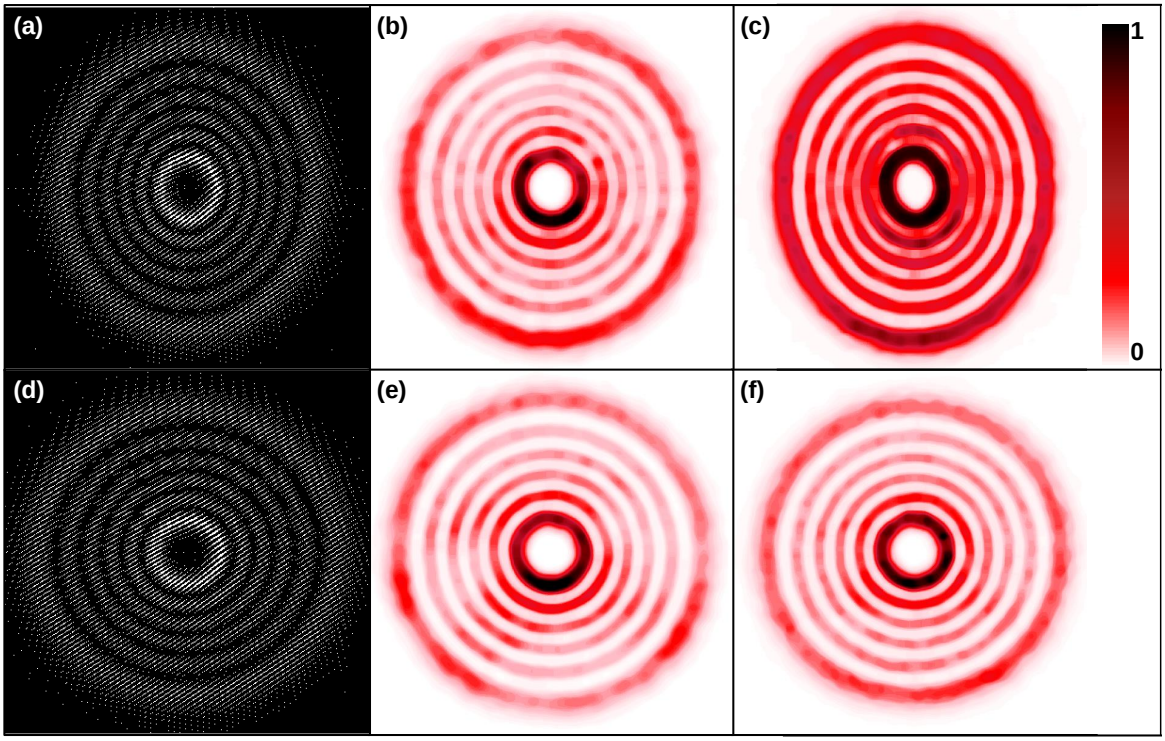


Fig. 2.9 (a) the computed hologram as displayed on the DMD screen. (b) the measured beam with the DMD aligned at 0 rad. (c) the measured beam with the DMD aligned at $\pi/15$ rad, when using the initial encoding scheme. (d), (e) and (f) show the same but using the optimised encoding.

2.3.1 Amplitude profile correction

This section examines the effect of different alignment configurations of the DMD on the fidelity of the amplitude profiles of the beams it is generating. LG beams are used as an example, and are generated using complex amplitude modulation as described in Sec. 1.1.2. Figure 2.14 demonstrates that the procedures outlined can be applied to a variety of beams in addition to LG beams. To determine the effect of alignment on mode fidelity, the experimental setup in Fig. 2.8 was constructed. This setup used a well expanded and collimated laser beam of uniform intensity which was incident on the 3000 series DMD. The first order holographic diffraction from the DMD was then imaged by a 4f system to a Point Grey Blackfly camera. The DMD was aligned in two orientations: first, the low diffractive efficiency orientation in which the mirrors in the parked state are perpendicular to the incident beam; and second, the high efficiency orientation, in which the mirrors in the off state are perpendicular to the incident beam, resulting in an incident angle of $\pi/15$ rad.

Initially the matrix used to create the hologram used the mirror pitch to define the positions of the mirrors in space, the principle being that such an encoding scheme would result in a hologram displayed on the DMD with the correct dimensions and so would produce a high fidelity beam . Figure 2.9 shows the computer generated holograms for an LG_5^5 beam as they appear on the DMD together with the experimentally generated result. It is seen that with the initial encoding scheme, the generated modes are vertically elongated (meaning a low fidelity beam) with the elongation more prominent when the device is aligned at $\pi/15$ rad. This ellipticity is a result of the imperfect mapping between the supposed position of the DMD pixels in software and the true position of the pixels, caused by the projection of a Cartesian matrix in software onto the diamond arrangement of pixels on the DMD. The ellipticity of the modes is corrected with a further adjustment of the encoding scheme for the generation of the binary holograms. By means of iteratively optimising the x-dimension. It was found that a ratio between the horizontal and vertical pixel size in the encoding scheme of 1.6889 corrected the elongation. It should be noted here that the orientation and pixel indexing of DMDs may differ from the standards used by software. For example, on the 3000 series DMD, pixels are indexed from the top right hand corner of the screen as opposed to the traditional starting point of the top left, assumed in most programmes.

Further, the screen on the 3000 series is rotated by π rad. Therefore the pixel addressed as 'row one column one' is in the bottom left of the screen. It is important to ascertain the specific screen orientation and pixel addressing system used by the DMD to ensure the correct calculation and displaying of holograms. To quantify the quality of the amplitude profile of the modes the measured beams were tested using Pearson's R as a measure of correlation between the observed and theoretical profiles, as shown in Fig. 2.10. Note that the highest correlation is obtained ($\approx 97\%$) with optimal pixel encoding and when the DMD is aligned at $\pi/15$ rad. The correlation drops by 0.7% with the DMD aligned at 0 rad, even when using the optimal encoding. When using the initial unoptimised encoding scheme, the correlation drops to below 91% for both alignments. Figure 2.10 illustrates that the highest fidelity modes are produced with the highest efficiency when using the optimal pixel encoding scheme and a DMD is alignment of $\pi/15$ rad.

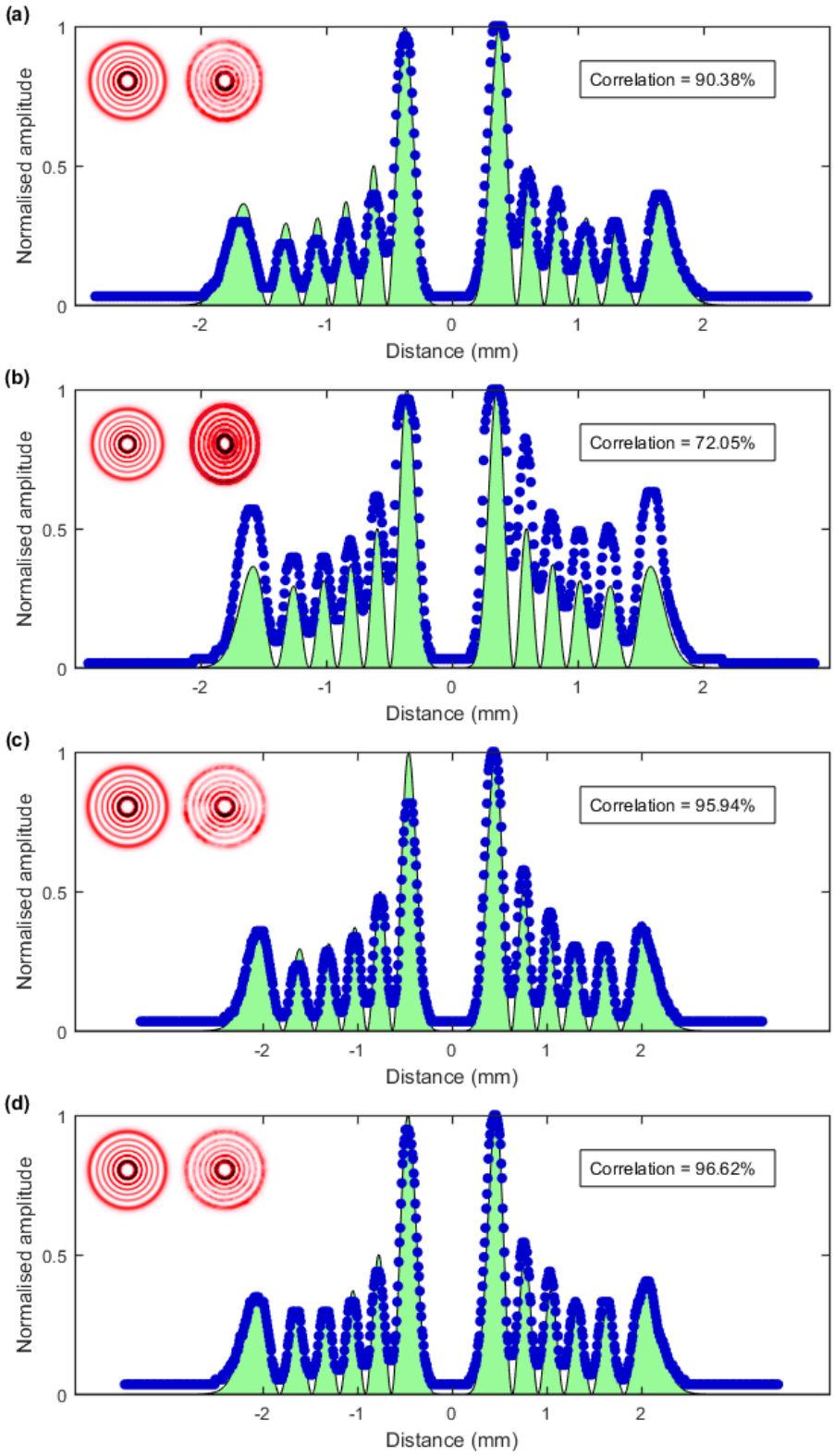


Fig. 2.10 Correlation between the theoretical (green solid) and experimental (blue dots) LG_5^5 beam for both alignments and encoding schemes. The inset shows a side by side comparison of the beams with the ideal beam on the left and the measured beam on the right. (a) the initial encoding scheme at an angle of 0 rad. (b) the initial encoding scheme at an angle of $\pi/15$ rad. (c) the optimised encoding scheme at an angle of 0 rad. (d) the optimised encoding scheme at an angle of $\pi/15$ rad.

2.3.2 Phase profile correction

Aberration correction is an important step in beam shaping. Imperfections in the manufacturing process mean that beam shaping devices such as DMDs are often not optically flat, resulting in (mostly astigmatic) phase distortions of the shaped beam. Correcting the phase of these devices thus allows the generation of higher quality beams [2.21;2.31]. Information reagrding the surface distortions of beam shaping devices is typically determined using an interferometric approach [2.32;2.33]. By interfering a reference beam with the beam reflected from the DMD, phase irregularities can be clearly seen in the interferogram. However, interferometric approaches are often difficult to align. As an alternative, a fast non-interferometric approach was proposed which allows the determination of phase distortions from a single image of a LG_1^0 beam at the focal plane of a lens [2.34]. Here a hybrid scheme is implemented with the aforementioned single image procedure as an integral step to correct the aberrations of both the 3000 series and 6000 series DMDs. Since the procedure cannot distinguish the source of the aberrations, it will also compensate for phase errors from other optics, such as lenses and mirrors, in the optical path. This is an added benefit of the procedure.

Full details of the procedure are found in [2.34]. The concept behind the method is that LG beams with small ℓ values are very sensitive to phase distortions. Hence, by observing the distortions of a $\ell = 1$ LG beam at the focal plane, the phase irregularities can be inferred because at the focal plane the phase distortions manifest as amplitude distortions. Specifically, the phase is inferred through the application of a phase-retrieval algorithm to the observed intensity of the distorted 'doughnut' image generated at the focal plane. Here the Gerchberg-Saxon (G-S) algorithm is used [2.35]. The retrieved phase determined by the G-S algorithm is a sum of the beam's phase and the encoded helical phase. By subtracting the helical phase from the combination, the beam's phase is isolated and can be removed from the phase of all subsequently generated holograms.

Experimental verification of aberration correction

To demonstrate the aberration correction method outlined above, an experimental setup (Fig. 2.11) was used in which a well expanded and collimated laser beam of uniform intensity was incident on the 3000 series DMD. The first order holographic diffraction from the DMD was then passed through a lens and a Point Grey Blackfly camera placed at the focal plane. The DMD was aligned at an incident angle of $\pi/15$ rad. The results of the DMD aberration correction are summarised in Fig. 2.12. A selection of modes were used

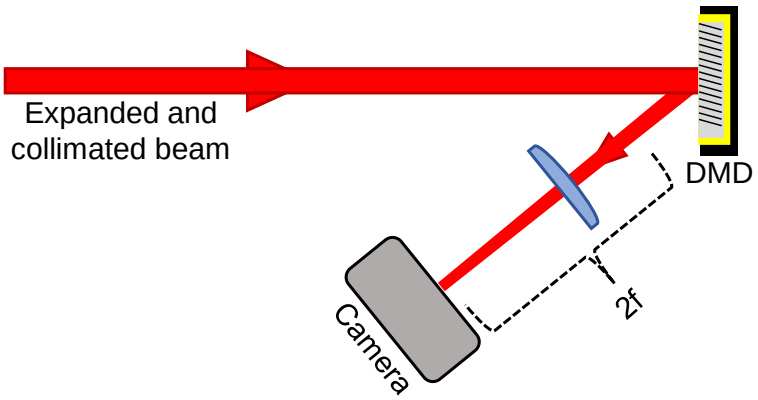


Fig. 2.11 The setup to demonstrate the efficacy of the wavefront correction method. An expanded and collimated beam was incident on a DMD. The first order holographic diffraction was then focused through a lens. A camera was placed at the focal plane of the lens.

to test the method. The modes were an LG_5^0, an LG_0^5 and a superposition of an LG_5^5 and LG_{-5}^5. The initial beams are shown in the top row, while the corrected beams are shown in the bottom row.

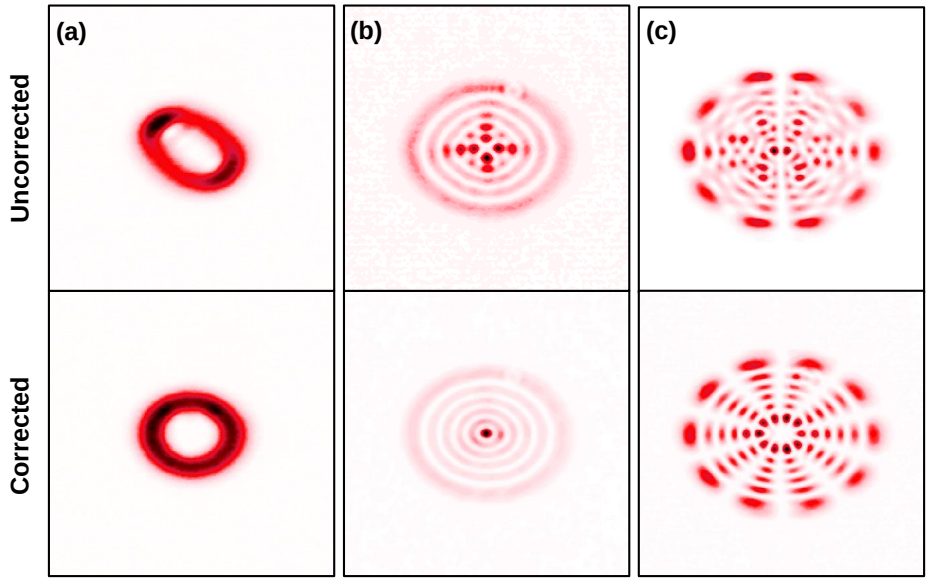


Fig. 2.12 The effect of the aberration correction procedure for the 3000 series DMD. The top row shows: (a) an LG_5^0; (b) an LG_0^5; and (c) a superposition of an LG_5^5 and LG_{-5}^5 beam. The bottom row shows the beams after correction. The colourmap is the same as that used in Fig. 2.9.

The drawback of this aberration correction method is that it is only able to correct for small phase distortions, of the order of the incident light's wavelength. If the DMD has larger surface distortions, the algorithm will fail to converge, since the starting point is too far away from an acceptable local minimum. This can be overcome by adopting a semi-empirical workaround. Often, first order astigmatism is the main contributor to the aberration. Hence, by adding phase maps corresponding to first order astigmatism and manually adjusting the weighting coefficients of these maps, a significant portion of the phase error can be removed. Doing so will improve the starting point of the algorithm, and increase the likelihood of converging to a local minimum. This entire process can be iterated as many times as necessary until the desired performance is achieved. The 3000 series DMD in the experimental setup shown in Fig. 2.11 was replaced with the 6500 model DMD. The initial aberration was too high for the G-S algorithm to converge and the semi-empirical method was employed to obtain an initial condition within the range of the algorithm. This intermediate beam was then analysed using the G-S algorithm, which converged to an acceptable local minimum after approximately 40 iterations. As can be seen in Fig. 2.13 (d) the corrected beam is of high quality, indicating that residual phase distortions are small. Figure 2.14 shows four things: amplitude only modulation; the

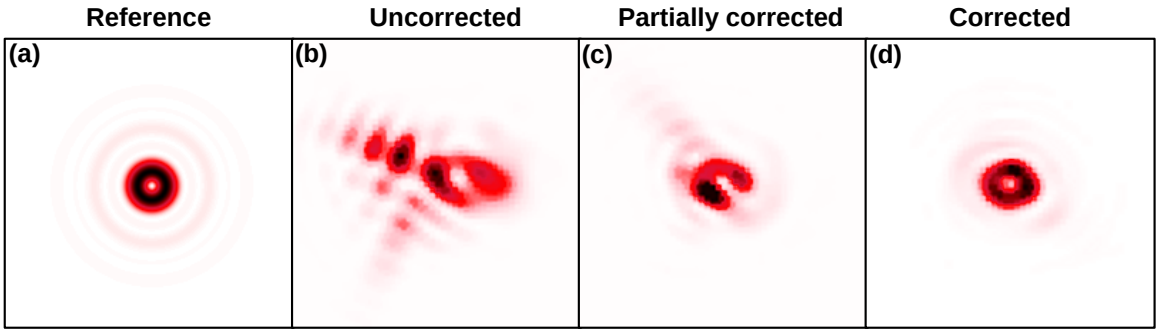


Fig. 2.13 Experimental aberration correction of the 6500 DMD. (b) The initial beam aberration is too large for the algorithm to handle, the first order astigmatism was manually corrected for. (c) The partially corrected beam after the manual aberration correction. After this, the intermediate beam can be fed through the G-S algorithm to find the remaining phase distortions. (d) The corrected beam.

introduction of an optical vortex; the creation of a high order Hermite-Gaussian mode by complex amplitude modulation; and a superposition of HG modes by complex amplitude modulation. It does this by displaying the holograms used to produce each beam, the intended intensity profile of each beam, and the measured intensity profile of each beam.

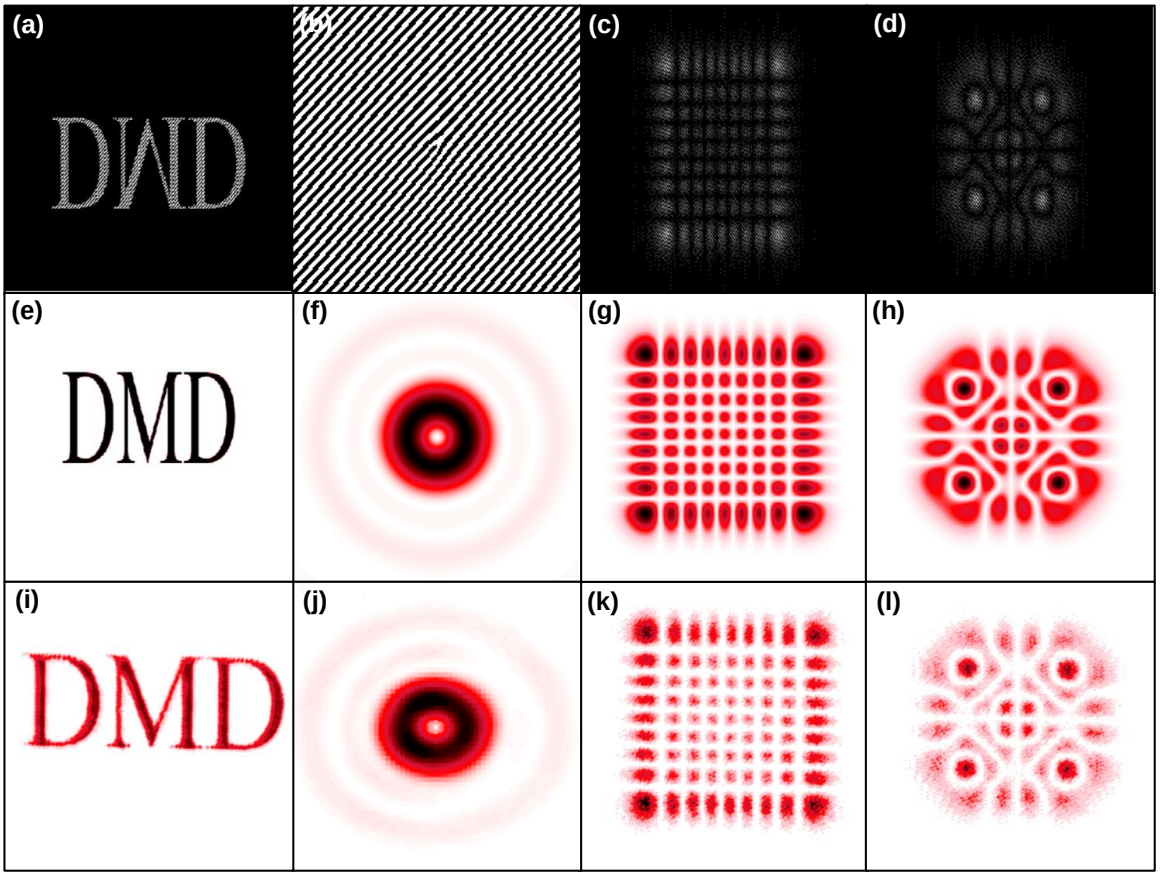


Fig. 2.14 (a), (b), (c) and (d) show the computed holograms to generate: the text "DMD" using amplitude only modulation; a phase singularity at the focal plane of a lens; an HG_8^8 mode using complex amplitude modulation; and a superposition of an HG_3^7 and an HG_7^3 mode using complex amplitude modulation. Note the apparent elongation of the holograms, this is a result of the optimised encoding scheme used to generate the holograms. When displayed on the DMD, the pixel arrangement of the screen causes the holograms to be drawn out to the correct aspect ratio. (e), (f), (g) and (h) show the intended intensity profiles of the beams generated by the holograms in the first row. (i), (j), (k) and (l) show the experimentally measured beams.

The close agreement between the intended and the measured intensity profiles in Fig. 2.14 demonstrates how the recommendations made in this work can be applied to a variety of beam shaping techniques and spatial modes using DMDs.

2.4 Summary of chapter 2

Chapter 2 explained the proper experimental implementation of DMDs. A thorough analysis of their functioning has been presented to ensure their correct implementation in later chapters. Specifically, Sec. 2.2.3 proves that a theoretical treatment in which the DMD is characterised as an modified amplitude grating is accurate whereas the widely made assumption that it is a simple amplitude grating or blazed grating is not. This is a novel finding. This characterisation implies that the most pragmatic approach to DMD alignment, balancing ease of alignment with diffractive efficiency, is to align the DMD so that an incident beam strikes it such that the off state mirrors are normal to the incident beam. In this configuration, the DMD is able to produce high fidelity modes when an appropriate encoding scheme is used to generate the hologram, as outlined in Sec. 2.3.1. Finally, an explanation of how to compensate for the phase aberrations inherent to DMDs using a semi-empirical method based on the Gerchberg-Saxon algorithm is demonstrated.

Chapter 3 now examines the manipulation of structured light using LCoS SLMs. The findings presented here in Chp. 2 will be of relevance again in Chp. 4.

References

2.1 L. J. Hornbeck, "Deformable mirror light modulator," Apr. 10 1984, US Patent 4,441,791.

2.2 ——, "Current status of the digital micromirror device (dmd) for projection television applications," in *Proceedings of IEEE International Electron Devices Meeting*. IEEE, 1993, pp. 381–384.

2.3 J. B. Sampsell, "Digital micromirror device and its application to projection displays," *Journal of Vacuum Science & Technology B: Microelectronics and Nanometer Structures Processing, Measurement, and Phenomena*, vol. 12, no. 6, pp. 3242–3246, 1994.

2.4 L. J. Hornbeck, "Digital light processing for high-brightness high-resolution applications," in *Projection Displays III*, vol. 3013. International Society for Optics and Photonics, 1997, pp. 27–40.

2.5 T. M. Kreis, P. Aswendt, and R. Höfling, "Hologram reconstruction using a digital micromirror device," *Optical Engineering*, vol. 40, 2001.

2.6 D. Dudley, W. M. Duncan, and J. Slaughter, "Emerging digital micromirror device (dmd) applications," in *MOEMS display and imaging systems*, vol. 4985. International Society for Optics and Photonics, 2003, pp. 14–25.

2.7 P. J. Rodrigo, I. R. Perch-Nielsen, and J. Glückstad, "High-speed phase modulation using the rpc method with a digital micromirror-array device," *Optics Express*, vol. 14, no. 12, pp. 5588–5593, 2006.

2.8 J. Liang, R. N. Kohn Jr, M. F. Becker, and D. J. Heinzen, "High-precision laser beam shaping using a binary-amplitude spatial light modulator," *Applied Optics*, vol. 49, no. 8, pp. 1323–1330, 2010.

2.9 ——, "High-precision beam shaper for coherent and incoherent light using a dlp spatial light modulator," in *Emerging Digital Micromirror Device Based Systems and Applications III*, vol. 7932. International Society for Optics and Photonics, 2011, p. 793208.

2.10 E. Ulusoy, L. Onural, and H. M. Ozaktas, "Full-complex amplitude modulation with binary spatial light modulators," *Journal of the Optical Society of America A*, vol. 28, no. 11, pp. 2310–2321, 2011.

2.11 D. Akbulut, T. J. Huisman, E. G. van Putten, W. L. Vos, and A. P. Mosk, "Focusing light through random photonic media by binary amplitude modulation," *Optics Express*, vol. 19, no. 5, pp. 4017–4029, 2011.

2.12 J. Liang, S.-Y. Wu, R. N. Kohn, M. F. Becker, and D. J. Heinzen, "Grayscale laser image formation using a programmable binary mask," *Optical Engineering*, vol. 51, no. 10, p. 108201, 2012.

2.13 V. Lerner, D. Shwa, Y. Drori, and N. Katz, "Shaping Laguerre-Gaussian laser modes with binary gratings using a digital micromirror device," *Optics Letters*, vol. 37, no. 23, pp. 4826–4828, 2012.

2.14 L. Gong, Y. Ren, W. Liu, M. Wang, M. Zhong, Z. Wang, and Y. Li, "Generation of cylindrically polarized vector vortex beams with digital micromirror device," *Journal of Applied Physics*, vol. 116, no. 18, p. 183105, 2014.

2.15 K. J. Mitchell, S. Turtaev, M. J. Padgett, T. Čižmár, and D. B. Phillips, "High-speed spatial control of the intensity, phase and polarisation of vector beams using a digital micro-mirror device," *Optics Express*, vol. 24, no. 25, pp. 29 269–29 282, 2016.

2.16 E. Peters, P. Clemente, E. Salvador-Balaguer, E. Tajahuerce, P. Andrés, D. G. Pérez, and J. Lancis, "Real-time acquisition of complex optical fields by binary amplitude modulation," *Optics Letters*, vol. 42, no. 10, pp. 2030–2033, 2017.

2.17 B. Vohnsen, A. C. Martins, S. Qaysi, and N. Sharmin, "Hartmann-Shack wavefront sensing without a lenslet array using a digital micromirror device," *Applied Optics*, vol. 57, no. 22, pp. E199–E204, 2018.

2.18 H. González, L. Martínez-León, F. Soldevila, M. Araiza-Esquivel, J. Lancis, and E. Tajahuerce, "High sampling rate single-pixel digital holography system employing a dmd and phase-encoded patterns," *Optics Express*, vol. 26, no. 16, pp. 20 342–20 350, 2018.

2.19 M. A. Cox, E. Toninelli, L. Cheng, M. J. Padgett, and A. Forbes, "A high-speed, wavelength invariant, single-pixel wavefront sensor with a digital micromirror device," *IEEE Access*, vol. 7, pp. 85 860–85 866, 2019.

2.20 R. Liu, S. Zhao, P. Zhang, H. Gao, and F. Li, "Complex wavefront reconstruction with single-pixel detector," *Applied Physics Letters*, vol. 114, no. 16, p. 161901, 2019.

2.21 S. Turtaev, I. T. Leite, K. J. Mitchell, M. J. Padgett, D. B. Phillips, and T. Čižmár, "Comparison of nematic liquid-crystal and dmd based spatial light modulation in complex photonics," *Optics Express*, vol. 25, no. 24, pp. 29 874–29 884, 2017.

2.22 J. P. Rice, J. E. Neira, M. Kehoe, and R. Swanson, "Dmd diffraction measurements to support design of projectors for test and evaluation of multispectral and hyperspectral imaging sensors," in *Emerging Digital Micromirror Device Based Systems and Applications*, vol. 7210. International Society for Optics and Photonics, 2009, p. 72100D.

2.23 M.-C. Park, B.-R. Lee, J.-Y. Son, and O. Chernyshov, "Properties of dmds for holographic displays," *Journal of Modern Optics*, vol. 62, no. 19, pp. 1600–1607, 2015.

2.24 P. Zhu, O. Fajardo, J. Shum, Y.-P. Z. Schärer, and R. W. Friedrich, "High-resolution optical control of spatiotemporal neuronal activity patterns in zebrafish using a digital micromirror device," *Nature Protocols*, vol. 7, no. 7, p. 1410, 2012.

2.25 S. N. Chandrasekaran, H. Ligtenberg, W. Steenbergen, and I. M. Vellekoop, "Using digital micromirror devices for focusing light through turbid media," in *Emerging Digital Micromirror Device Based Systems and Applications VI*, vol. 8979. International Society for Optics and Photonics, 2014, p. 897905.

2.26 Y.-X. Ren, Z.-X. Fang, L. Gong, K. Huang, Y. Chen, and R.-D. Lu, "Digital generation and control of Hermite-Gaussian modes with an amplitude digital micromirror device," *Journal of Optics*, vol. 17, no. 12, p. 125604, 2015.

2.27 Y.-X. Ren, R.-D. Lu, and L. Gong, "Tailoring light with a digital micromirror device," *Annalen der Physik*, vol. 527, no. 7-8, pp. 447–470, 2015.

2.28 A. Carmichael Martins and B. Vohnsen, "Analysing the impact of myopia on the stiles-crawford effect of the first kind using a digital micromirror device," *Ophthalmic and Physiological Optics*, vol. 38, no. 3, pp. 273–280, 2018.

2.29 "Shimadzu inc. application note - blazed wavelength." [Online]. Available: https://www.shimadzu.com/opt/guide/diffraction/07.html

2.30 J. W. Goodman, *Introduction to Fourier optics 2nd Edition*. New York: The MacGraw-Hill Companies, 1998.

2.31 T. Čižmár, M. Mazilu, and K. Dholakia, "In situ wavefront correction and its application to micromanipulation," *Nature Photonics*, vol. 4, no. 6, pp. 388–394, 2010.

2.32 G. D. Love, "Wave-front correction and production of Zernike modes with a liquid-crystal spatial light modulator," *Applied Optics*, vol. 36, no. 7, pp. 1517–1524, 1997.

2.33 T.-L. Kelly and J. Munch, "Phase-aberration correction with dual liquid-crystal spatial light modulators," *Applied Optics*, vol. 37, no. 22, pp. 5184–5189, 1998.

2.34 A. Jesacher, A. Schwaighofer, S. Fürhapter, C. Maurer, S. Bernet, and M. Ritsch-Marte, "Wavefront correction of spatial light modulators using an optical vortex image," *Optics Express*, vol. 15, no. 9, pp. 5801–5808, 2007.

2.35 R. W. Gerchberg, "A practical algorithm for the determination of phase from image and diffraction plane pictures," *Optik*, vol. 35, pp. 237–246, 1972.

Chapter 3

Manipulating structured light using LCoS Spatial Light Modulators

Pages 61 through 72 of this chapter are based on the publication
***S. Scholes**, V. Rodríguez-Fajardo, and A. Forbes, "Lossless reshaping of structured light," Journal of the Optical Society of America A, 37, p.C80-C85, 2020.*
Author S.S derived the theoretical model and performed the experiments. All authors contributed to the writing of the associated publication with supervision provided by author A.F.

Pages 73 through 78 of this chapter are based on the publication
***S. Scholes**, and A. Forbes, "Improving the beam quality factor (M^2) by phase-only reshaping of structured light," Optics Letters, 45, p.3753-3756, 2020.*
Author S.S derived the theoretical model, performed the experiments and wrote the associated publication with supervision provided by author A.F.

The aim of this chapter is to explore how the structure of a beam can be manipulated without loss of power to reduce its M^2, and so improve brightness. To achieve this, a means of altering both the phase and amplitude structure of a beam in a lossless way must first be established.

3.1 Lossless reshaping of light

This chapter considers the common case of spatial structuring of *scalar* light. The approach demonstrated here can be used for full control when implemented in combination

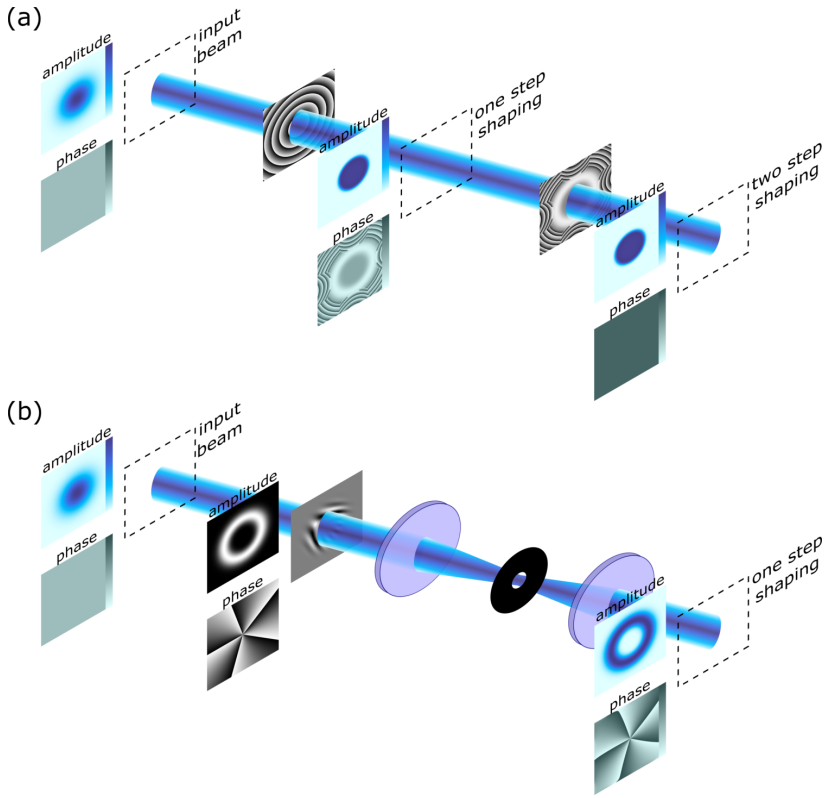


Fig. 3.1 The different approaches to creating structured light. Panel (a) shows how lossless single-step shaping can be achieved using a phase-only element, but requires the phase at the target plane to be left as a free DoF, requiring a second element for correction. Panel (b) shows how a single step in which the amplitude of the beam is also controlled can produce ideal structured light, but now the process is lossy.

with temporal [3.1;3.2] and vectorial [3.3;3.4;3.5] shaping tools. The problem of converting a Gaussian beam into some other form has many specific solutions. For example, conversion of a Gaussian to a flattop beam achieved with refractive [3.6], diffractive [3.7] and holographic approaches [3.8], or the creation of vortex beams by spiral phase plates [3.9], geometric phase [3.10;3.11] and spatial light modulators [3.12]. It is not fully appreciated that when this is done in a single step, as is the case with many of these examples cited above, the transformation is either imperfect or lossy. To illustrate this, consider perhaps the simplest beam shaping problem, reshaping a Gaussian beam in size while maintaining the Gaussian amplitude profile and input phase. A single-step approach, with a single lens, will correctly resize the beam in a lossless manner, but will alter the phase so that the shaping is imperfect. The phase degree of freedom (DoF) must still be corrected for. This is achieved using two lenses, i.e. a two-step approach. Such a telescope, appropriately designed, will (in principle) correctly shape both DoFs in a lossless manner. To return to

the earlier examples (see Fig. 3.1), it is possible to create a flattop beam losslessly in a single step if the phase is left as a free DoF [3.13], while single-step shaping of Gaussian beams into vortex beams that carry orbital angular momentum (OAM) [3.14;3.15] through azimuthal phase transformation results in the correct 'vortex' phase but leaves the amplitude as a free DoF: many radial modes are excited with low power content in the desired ring of light [3.16;3.17]. Perfect reshaping can be achieved in one step, but then the process is lossy, requiring amplitude control (such as complex amplitude modulation), as has been done for the creation of radial mode controlled vortex beams [3.18].

Thus, in general, a two (or more) step approach is needed for complete and lossless reshaping of structured light. By applying tools from lossless beam shaping theory [3.19;3.20;3.21;3.22], solutions have been developed for specific cases, notably the special case of Gaussian to flattop conversion [3.23;3.24;3.25;3.26] implemented using refractive optics [3.27;3.28], holograms [3.29;3.30], prisms [3.31] and diffractive optics [3.32;3.33]. Likewise specific solutions have been found for the reverse problem, the *detection* of structured light, for OAM modes [3.34], Bessel modes [3.35;3.36], Hermite-Gaussian modes [3.37] and Laguerre-Gaussian modes [3.38] with lossless approaches always making use of two or more steps rather than a lossy single step [3.39].

In this chapter a generic approach for arbitrary reshaping of structured light beyond the special cases already visited is presented. A general recipe and a detailing of the conditions under which it is applicable is provided. General reshaping solutions beyond the simple Gaussian to flattop converters are demonstrated. The solutions are implemented experimentally as CGHs on LCoS SLMs, with the critical design steps elucidated. This implementation serves as a proof-of-principle. While LCoS SLMs are inherently lossy devices (with an efficiency of $\approx 60\%$) due to their diffractive properties, replacing them with appropriately coated diffractive or refractive optical elements would make the implementation functionally lossless.

3.2 Theoretical outline

Textbooks on lossless laser beam shaping describe the many approaches taken to date [3.21]. The concept applied here relies on redistributing the energy in an input beam with profile $|I(x,y)|^2$ in a precise way to form an output beam with a desired intensity profile $|Q(x,y)|^2$ at the focal plane of a lens, i.e., in the far field. The first element performs the energy redistribution and the second element corrects for the phase. This is achieved by imparting

the incident beam with a specific phase $\phi(x,y)$, as determined by the desired output profile. There are three steps to derive the necessary $\phi(x,y)$. The first is a calculation of a scaling constant A. This constant is the ratio of the energy of the input beam to the output beam. Next is the formulation of an intermediary mathematical function $\alpha(x,y)$. This is a spatial mapping function which moves energy from a specific spatial region of the input beam to a specific spatial region of the output beam in a way consistent with the conservation of energy from the scaling constant A. It is the calculation of this mapping function which lies at the heart of the method, since once $\alpha(x,y)$ is known, it is possible to perform the final step, which is to derive the phase delay $\phi(x,y)$ that must be introduced to a beam to achieve the desired output profile. The theory of this is known [3.21], and has been applied to the specific case of Gaussian to flattop converters [3.26;3.40], but it is expanded here in the context of structured light and laser brightness. This chapter makes clear how and when the approach works (and when it doesn't) as well as how the design steps impact on the practical reshaping of structured light.

3.2.1 Derivation of equations

Consider two planes in space, the first at coordinate $(x,y,z=0)$ and the second at a distance $(x,y,z=2f)$ where f is the focal length of a lens. The coordinate system for both the global position and the plane at $z=0$ is (x,y,z), while the coordinate system exclusively on the plane at $z=2f$ is (X,Y,Z). The function α maps regions of the input plane to regions of the output plane meaning $\alpha(x,y) \rightarrow (X,Y)$. A beam of amplitude profile $|I(x,y)|^2$ with a flat phase is incident upon the phase element $\phi(x,y)$ positioned at $(x,y,z=0)$. At the second plane, corresponding to the focal plane of the lens, a beam of amplitude profile $|Q(x,y)|^2$ is desired. To calculate the expression for the phase element $\phi(x,y)$ the energy scaling constant A must first be calculated.

$$A = \frac{\int_{-\infty}^{\infty} |I(X)|^2 dX}{\int_{-\infty}^{\infty} |Q(X)|^2 dX}. \tag{3.1}$$

The next step is to derive a differential expression for $\alpha(x,y)$. This expression will describe how the energy of the input beam at the plane of the phase element should be mapped to the focal plane of the lens to produce the desired output profile. Consider a beam affected by the phase element $\phi(x,y)$ passing through a lens. The beam at the focal plane of the lens in 1 dimension is given by

$$P(X) \propto \int_{-\infty}^{\infty} I(x) e^{i\phi(x)} e^{-i\frac{2\pi}{\lambda f}Xx} dx. \tag{3.2}$$

Recall that $\alpha(x) \rightarrow X$.

$$P(\alpha(x)) \propto \int_{-\infty}^{\infty} I(x) e^{i\phi(x)} e^{-i\frac{2\pi}{\lambda f}\alpha(x)x} dx. \tag{3.3}$$

Let

$$\begin{aligned} \phi(x) &= \frac{2\pi}{\lambda f}\Phi(x) \\ \gamma &= \frac{2\pi}{\lambda f} \end{aligned} \tag{3.4}$$

$$P(\alpha(x)) \propto \int_{-\infty}^{\infty} I(x) e^{i\gamma[\Phi(x)-\alpha(x)x]} dx. \tag{3.5}$$

Equation 3.5 can be evaluated by the method of stationary phase as

$$P(\alpha(x)) \propto I(x) e^{i\gamma[\Phi(x)-\alpha(x)x]} e^{i\frac{\pi}{4}} \frac{\sqrt{2\pi}}{\sqrt{\gamma\Phi(x)''}}, \tag{3.6}$$

with

$$\frac{d}{dx}[\Phi(x) - \alpha(x)x] = 0. \tag{3.7}$$

For a specific $\phi(x)$

$$|P|^2 \propto A|Q(X)|^2. \tag{3.8}$$

Thus

$$\begin{aligned} |I(x)|^2 \frac{2\pi}{\phi''} &= A|Q(X)|^2 \\ \frac{|I(x)|^2}{A|Q(\alpha(x))|^2} &= \phi''. \end{aligned} \tag{3.9}$$

Note [3.21]

$$\begin{aligned} \frac{d}{d\alpha}\left[\frac{d}{dx}[\Phi(x) - \alpha(x)x]\right] &= \frac{d^2\Phi}{dx^2}\frac{dx}{d\alpha} - 1 \\ \frac{d^2\Phi}{dx^2} &= \frac{d\alpha}{dx}. \end{aligned} \tag{3.10}$$

This gives $\alpha(x)$ in 1-dimensional Cartesian coordinates as

$$\frac{d\alpha(x)}{dx} = \frac{1}{A}\frac{|I(x)|^2}{|Q(\alpha(x))|^2}. \tag{3.11}$$

This equation describes how energy can be mapped from the input profile to the output profile in a manner consistent with the conservation of energy described by A. The phase $\phi(x)$ can then be calculated from the expression for α. The phase is

$$\begin{aligned} \frac{d\phi(x)}{dx} &= \gamma\alpha(x) \\ \phi(x) &= \gamma\int_0^x \alpha(s)ds. \end{aligned} \tag{3.12}$$

An indication of how well the generated beam will conform to the ideal output amplitude profile is provided by the quantity $\beta = \omega_i\omega_{\text{opt}}\gamma = 2\pi\omega_i\omega_{\text{opt}}/(\lambda f)$ [3.21]. The greater the value of β, the higher the fidelity of the beam at the focal plane with regards to the ideal output profile. Output profiles with abrupt changes in intensity (such as step functions) will typically require high (>30) β values to achieve acceptable fidelity [3.40]. Given input and output profiles of fixed waist ω_i and ω_{opt}, the parameter β, and, by extension, the fidelity of the output beam, can be increased by reducing the focal length f.

Solving the system of Eqns. 3.2-3.11 in polar coordinates gives

$$\frac{d\alpha(r)}{dr} = \frac{1}{A}\frac{r|I(r)|^2}{\alpha(r)|Q(\alpha(r))|^2}. \tag{3.13}$$

In Fig. 3.2, a truncated Gaussian input is mapped to an annular polynomial output defined by the equation $X^2 - X^4$. Note the following: the function $\alpha(x)$ maps points from the input plane to points of the output plane; the points near the centre of the input plane where the beam is most intense, indicated by the red solid and magenta dotted lines, are mapped to points further apart on the output plane than a point further out on the input plane; the function $\alpha(x)$ has a maximum value ω_{opt}, corresponding to the waist of the output beam, and the scaling constant A as given in Eqn. 3.1 relates the shaded area of the output profile to the shaded area of the input profile, ensuring that the method is lossless since energy is conserved.

3.2.2 Properties of the $\alpha(x)$ function

The mapping function $\alpha(x)$ has three properties of interest. First, Eqn. 3.11 breaks down for $|Q(\alpha(x))|^2 = 0$. The formulation of $\alpha(x)$ cannot map an input beam to a region of the output beam containing no light as this would require a phase singularity. Second, and as a consequence of the first property, the value of $\alpha(x)$ monotonically approaches an

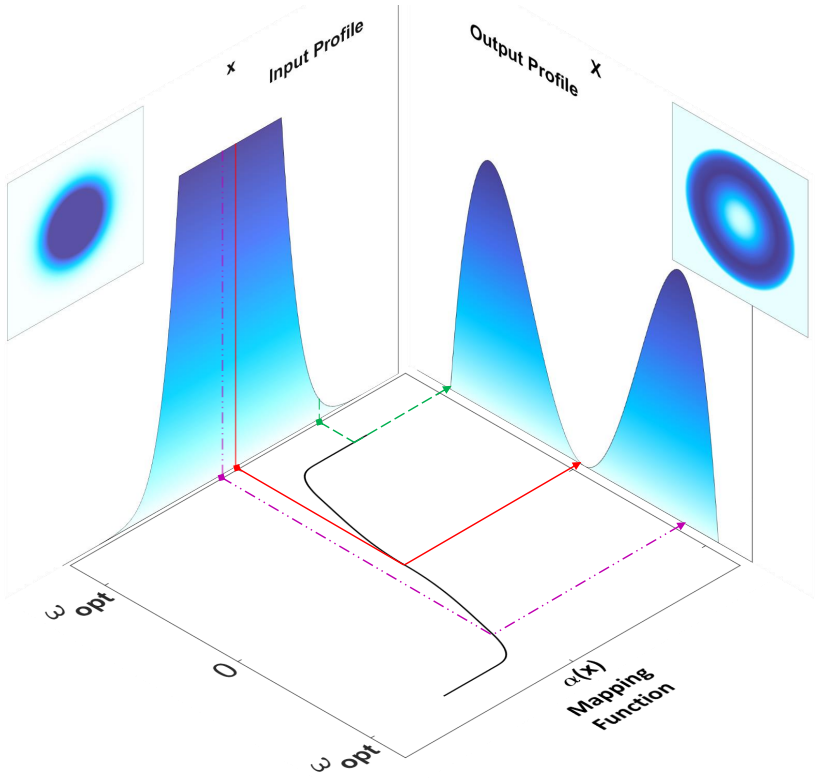


Fig. 3.2 The mapping function α for a truncated Gaussian input to an annular polynomial output. The insets show the intensities of the input and output beams while the panels show the beam profiles.

asymptotic maximum value corresponding to the value of the waist of the output beam ω_{opt}, as seen in Fig. 3.2. Third, the choice of coordinate system has a significant impact on the structure and functioning of $\alpha(x)$.

Consider the integration over all space of a circular Gaussian beam in Cartesian separated coordinates,

$$\begin{aligned} V &= \int_{-\infty}^{\infty}\int_{-\infty}^{\infty} \exp\left(-x^2\right)\exp\left(-y^2\right) dx dy, \\ V &= \int_{-\infty}^{\infty} \exp\left(-x^2\right) dx \int_{-\infty}^{\infty} \exp\left(-y^2\right) dy, \\ V &= \sqrt{\pi}\sqrt{\pi}, \\ V &= \pi. \end{aligned} \tag{3.14}$$

As well as in Polar coordinates,

$$\begin{aligned} V &= \int_0^{2\pi}\int_0^{\infty} r\exp\left(-r^2\right) dr d\theta, \\ V &= \int_0^{2\pi} d\theta \int_0^{\infty} r\exp\left(-r^2\right) dr, \\ V &= 2\pi\frac{1}{2}, \\ V &= \pi. \end{aligned} \tag{3.15}$$

When integrating over all space, the results of these two expressions are the same. However, if the working is limited to only a 1-dimensional integral, along x in the Cartesian case and r in the Polar case, the result is $\sqrt{\pi}$ and 1/2 respectively. This difference in scaling affects A, the mapping function $\alpha()$, and then by extension the phase element. Functionally, by reducing the problem to 1 dimension to enable a simplified solution a 'propagation of coordinate system' is inadvertently introduced. If the Cartesian expression is chosen, the phase element will attempt to produce an output profile with Cartesian symmetry, while if the Polar expression is used, the output profile will have a radial symmetry.

3.2.3 Deriving the second phase element

The beam which forms at the plane $z = 2f$ has the desired intensity profile $|Q(x,y)|^2$ and an uncontrolled phase $\psi(x,y)$. This is because to losslessly control the amplitude of the beam in a single step using the first phase element, the phase of the beam must be left as a free DoF. To complete the perfect lossless reshaping, the second phase element must first remove the uncontrolled phase $\psi(x,y)$. This can be achieved by designing the second element to have a phase $-\psi(x,y)$. There are two approaches to doing this. For problems using either a short focal length or a smooth output profile where the β parameter is sufficiently large to ensure high fidelity, the second phase element can be well approximated as the complex conjugate of the first shaping element. Alternatively, if the β parameter cannot be made large enough to ensure fidelity, the second element is better designed by using numerical simulation to determine the phase of the shaped beam at the relevant plane. This is due to the second property of the mapping function $\alpha(x)$ discussed previously. In cases where the reshaping is inaccurate (an insufficient β) energy will fall outside the boundary of ω_{opt}, violating the mapping function $\alpha(x)$ associated with the first element and resulting in a breakdown of the system. By using a numerical simulation to extract the phase instead of obtaining it by conjugating the first element, this problem can be overcome. Once the beam has passed through the second phase element and has

a flat phase, it can be passed through any other phase-only element with phase $\psi'(x,y)$. Hence a beam with desired amplitude profile $Q(x,y)$ and phase $\psi'(x,y)$ can be created.

3.3 Experimental implementation I

To demonstrate the method experimentally, a Gaussian beam was converted into several different spatial profiles. Figure 3.3 shows the experimental setup used. The first phase element, as described in Sec. 3.1, was modelled using a Holoeye Pluto 1 LCoS SLM illuminated by a well expanded and collimated beam from a HeNe laser source. The SLM displayed a hologram which created a beam with a Gaussian amplitude profile and a phase calculated by Eqn. 3.12. The beam from the SLM passed through a lens of focal length f1 = 0.5 m . At the focal plane of this lens the desired output beam $|Q(x,y)|^2$ formed. This mode was filtered and imaged to a CCD by means of a 4f lens system with f2 = f3 = 0.3 m.

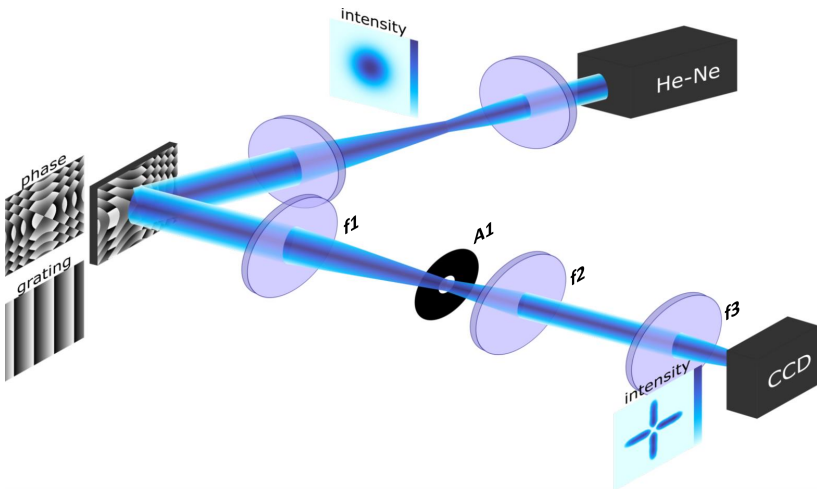


Fig. 3.3 Conceptual design of the experimental setup used to implement the method. A well expanded and collimated beam from a HeNe source was incident on the SLM. The beam from the SLM passed through lens f1 forming the desired profile $|Q(x)|^2$ at the plane of the black aperture A1. The plane of A1 was imaged to camera by a 4f system (lenses f2 and f3) . Here, the second beam shaping element described in Sec. 3.2.3 would be placed at the plane of the black aperture A1.

This first experiment was concerned with measuring the amplitude of the beam generated by the method. Therefore the second phase element was not implemented. The motivation for this is that the derivation of the first phase element is considerably more complex than the derivation of the second, so experimentally validating the design of the

first element was prioritised. Experimental implementation of the second phase element (and its effect on brightness) is presented in Sec. 3.5.

3.4 Experimental results I

The experimental results shown in Fig. 3.4a and Fig. 3.4b were created using the experimental setup shown in Fig. 3.3. The beams were generated by encoding a Gaussian beam of waist ω_G with the appropriate phase to form an output profile of waist ω_{opt} at the focal plane of a lens with focal length 0.5 m. The output profile was then captured by a camera. The waist parameters and cameras used are summarised in Table. 3.1. In the case of the

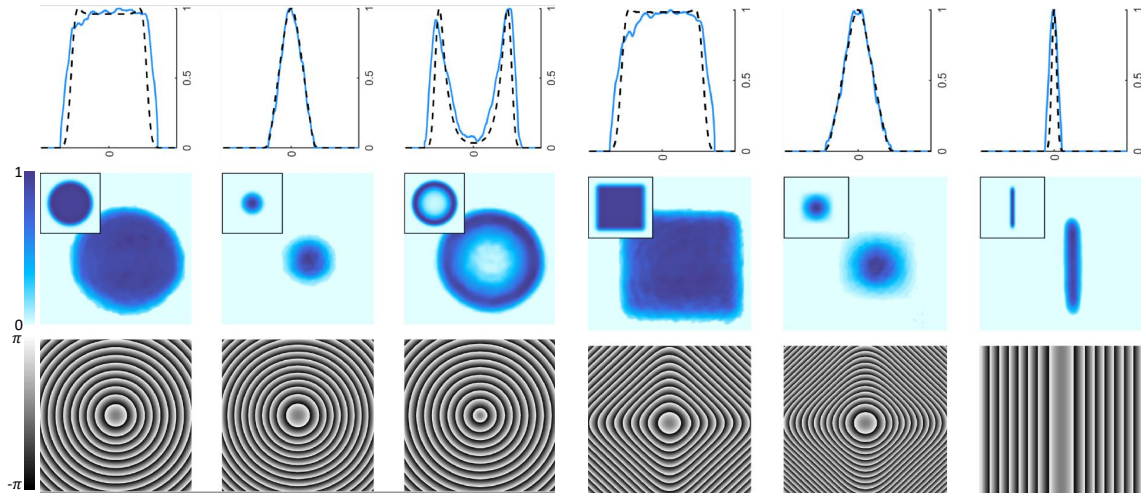
Table 3.1 The cameras, Gaussian and output profile waists used for the experiment.

Profile	ω_G **(m)**	ω_{opt} **(m)**	**Camera**
radial flattop radial annulus Cartesian 2D flattop	0.0011	0.0008	Logitech C270
Cartesian 1D Gaussian	0.0011	0.0007	
radial linear Cartesian linear	0.00087	0.0011	Thorlabs 1240C

Logitech C270 camera, all optics of the camera were removed to leave the sensor exposed.

Figure 3.4a shows the measured beams having radial symmetry. The phase of the first shaping element, the experimentally measured beam (as well as an inset of the simulated beam) and a comparison of the profiles of the measured and simulated beams are shown. The beams illustrated in Fig. 3.4a are a flattop, a beam with a linear intensity profile, and an annular beam. Figure 3.4b displays the same, but for beams of Cartesian symmetry. The beams illustrated in Fig. 3.4b are a flattop, a beam with a linear intensity profile, and a 1-dimensional Gaussian profile where the beam has a focused Gaussian intensity across one axis of its profile and a uniform profile in the other axis.

To quantify the fidelity of the generated modes, the Pearson's R correlation between the simulated and experimentally generated modes was calculated. The results are presented in Table. 3.2. The correlation measures the final purity of the experimentally created modes, while the lossless nature is a statement on the energy efficiency of the process. Using our approach, the resulting beams can be created with high efficiency (in theory



(a) The modes with radial symmetry. (b) The modes with Cartesian symmetry.

Fig. 3.4 Measured modes and profiles for (a) beams with radial symmetry and (b) beams with Cartesian symmetry. Each row of the figure shows, from left to right, the phase of the first shaping element, the experimentally measured beam, and a comparison of the profiles of the simulated and measured beams as a black dashed line and blue solid line respectively. The profile cross-sections are plotted on a transverse axis in millimetres. The insets in each experimental result show the simulated beam.

with 100% efficiency) and high purity, demonstrated here by correlations in excess of $>90\%$.

The results presented here demonstrate how the method can be used to generate

Table 3.2 The correlations between the simulated and measured beams.

Profile	Correlation
Radial flattop	95.1%
radial annulus	92.7%
radial linear	99.1%
Cartesian 1D Gaussian	90.9%
Cartesian 2D flattop	95.6%
Cartesian 2D linear	99.5%

modes with unique spatial profiles while maintaining high fidelity. An interesting extension to this reshaping method is how it may be applied to superpositions of modes. In particular, the separable nature of the Cartesian coordinate system allows two separate

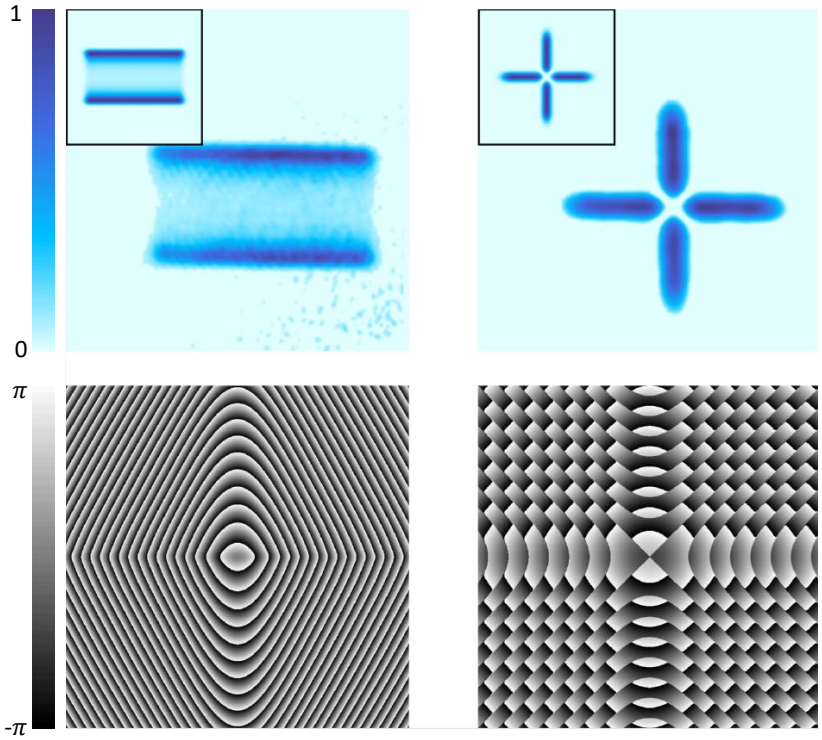


Fig. 3.5 The 'double bar' and 'cross hair' profiles. These profiles are the result of superpositions of modes at right angles to each other in a Cartesian symmetry.

profiles to be encoded perpendicularly to one another. Figure 4.8 shows the 'double bar' structure that emerged as a combination of a flattop profile and a linear valley profile at right angles to one another. Figure 4.8 also shows the combination of two 1D Gaussian profiles at right angles which gives rise to a 'cross hair' type mode.

The work above establishes a general approach to the reshaping of structured light. It could be extended and used in conjunction with temporal and vectorial shaping techniques to provide complete control over all the characteristics of light. This general formulation allows for the conversion of almost any input beam into a wide range of spatial profiles having both a specific phase and amplitude. This generality is supported by the experimental results presented.

Having presented a method for creating light with a desired amplitude and phase profile, the remainder of this chapter is concerned with the reciprocal problem, converting structured beams back into Gaussian beams. In particular, the effect of this destructuring on the brightness of a beam is examined.

The remaining pages in this chapter are based on the second publication mentioned at the start of the chapter hence the change in graphical style.

3.5 Improving the M^2

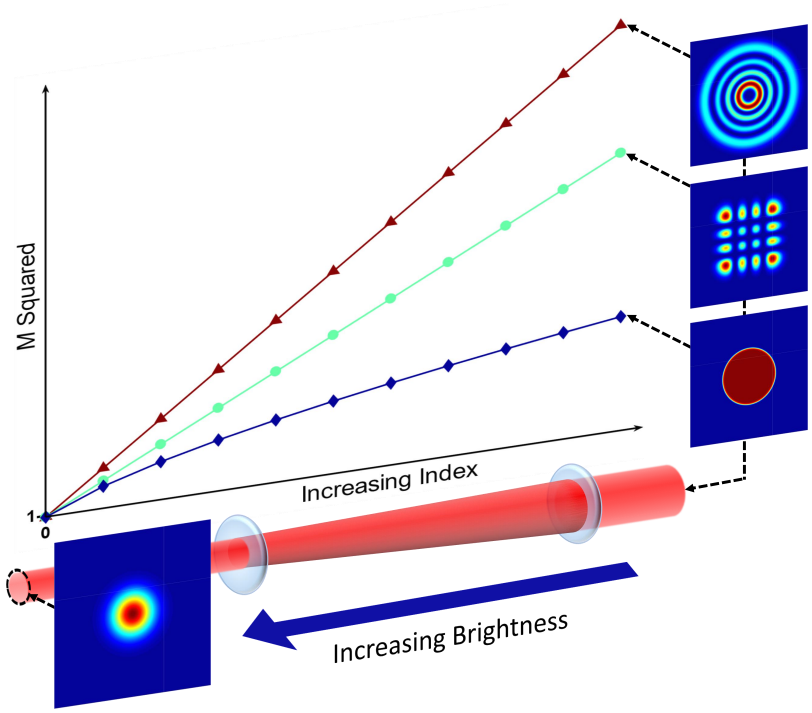


Fig. 3.6 The beam quality of structured light fields decreases with increasing mode index (see Table. 1.1), resulting in an increase in the beam quality factor, M^2, shown here for the examples of Hermite-Gaussian, Laguerre-Gaussian and Super-Gaussian beams, with the mode index plotted as $2m+2n+1$, $2p+|\ell|+1$ and k, respectively. By using the lossless reshaping technique presented in the first part of the chapter it is possible to move 'down the curve' towards a Gaussian ($M^2 = 1$) using an optical system with two phase-only elements, thus enhancing the brightness, shown here conceptually.

External brightness enhancement by beam transformation has proved limiting. It has been shown that the beam quality factor cannot be improved by binary diffractive optical elements [3.41], while demonstrations with single continuous phase elements [3.42;3.43] have so far resulted in a lossy or imperfect process, as explained in Sec. 3.1. So the beam quality is improved but not the brightness. Here, it is shown that by using the lossless reshaping technique presented in the first part of the chapter, the beam quality factor of an arbitrary beam can be improved. Importantly, because the approach is in principle lossless, P can be maintained while the M^2 is reduced, thus increasing the brightness, B.

If an initial beam of $M^2 > 1$ is converted to a Gaussian ($M^2 = 1$) while maintaining the same power (and wavelength), then the brightness can be enhanced by a factor $\eta = M^4$. Table 1.1 presents equations for the M^2 values [3.44;3.45] of the common beam types shown in Fig. 3.6.

While one-step approaches have been suggested to improve the beam quality factor, they come at the expense of loss or imperfect transformation, hence cannot improve the brightness. A lossless two-step approach is depicted graphically in Fig. 3.6 for some example structured light beam types. Structured light is a topical field [3.46] and often the structure is desired. But it can be undesirable in the context of laser brightness, such as when higher-order modes of structured beams are used to achieve higher output powers from laser sources due to their larger gain volume [3.47;3.48]. However, this does not increase brightness due to the reduced beam quality factor M^2 associated with higher-order modes [3.13;3.44;3.45;3.49;3.50;3.51], as shown in Fig. 3.6 and Table 1.1. By losslessly reshaping structured light, it is possible to move 'down the curves' of Fig. 3.6 towards lower M^2 without loss of power, ideally to a Gaussian beam with the highest beam quality (lowest beam quality factor, $M^2 = 1$). Since the method is based on a conformal mapping approach with two non-binary phase elements, as illustrated in Fig. 3.6, it is not in contradiction to prior work [3.41].

Consider one of the beams created in Sec. 3.4. These beams have an amplitude $Q(x, y)$ and phase ψ. From the reciprocity of light, passing this beam through the second optical element described in Sec. 3.2.3 twice will result in the beam having the conjugate phase, $-\psi$. The phase conjugation will cause the beam to 'unravel' as it propagates, effectively destructuring it, such that it arrives at the next phase element with the form $E(x, y) = A(x, y)\exp(-i\phi)$. The first phase-only element with phase ϕ now removes the unwanted phase from the beam, leaving only the Gaussian amplitude. Thus there are two phase elements needed, a first with a phase transmission function of -2ψ and a second with phase ϕ. This process is depicted in Fig. 3.7(a).

3.6 Experimental implementation II

Once again making use of LCoS SLMs. A single device was used with a split-screen approach, and henceforth the implementation will be explained conceptually with the two parts of the screen labelled SLM 1 and SLM 2. Using the setup shown in Fig. 3.7(b), an

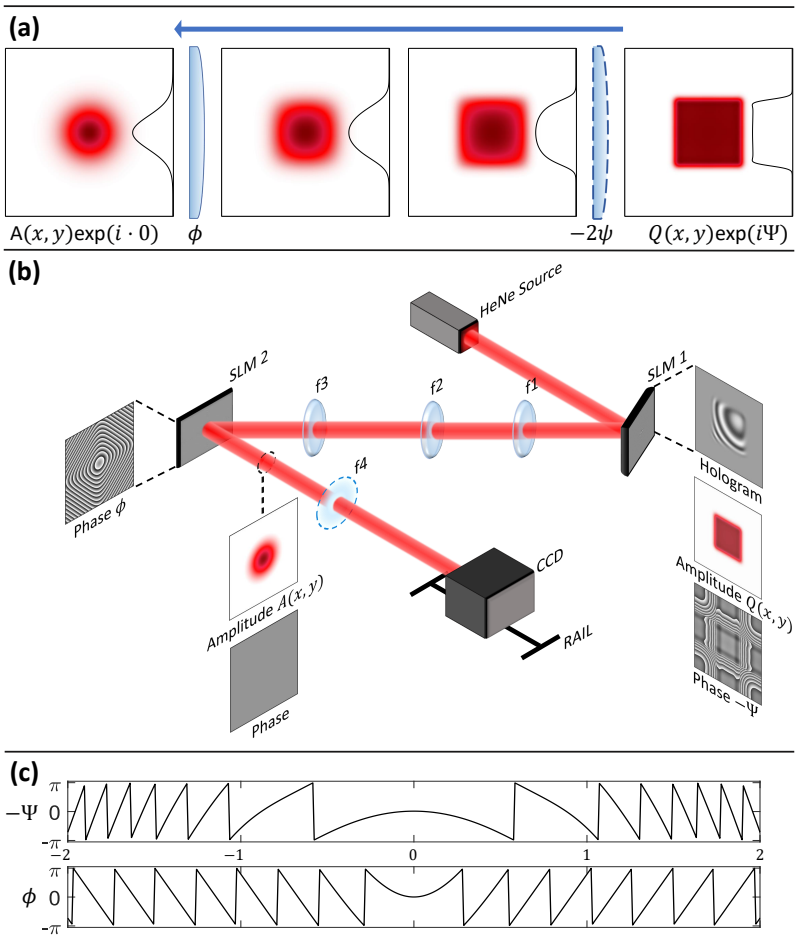


Fig. 3.7 (a) A step-wise depiction of the two-step approach corresponding to the subsequent panels. (b) The experimental setup consisted (conceptually) of two SLMs to implement the desired phase transformations. SLM 1 acted as the second phase element creating a beam of amplitude $Q(x,y)$ with phase $-\psi$. The beam passed through a lens f1 and was imaged (f2 and f3) onto the first phase element (SLM 2) with phase ϕ. The final beam, having a Gaussian amplitude $A(x,y)$ and a flat phase front was imaged by a camera. (c) The phase profiles $-\psi$ and ϕ encoded on SLM 1 and SLM 2 respectively. The elements match the case depicted in panels (a) and (b) and are plotted on a shared transverse axis in millimetres.

initial structured beam was created, modified through a two-step process, and then the M^2 value of the resultant Gaussian beam was measured. To begin, a well expanded and collimated beam from a HeNe laser was incident on SLM 1 which encoded some desired initial beam by complex amplitude modulation [3.52;3.53] as well as with the appropriate conjugate phase $-\psi$. The beam was then passed through a lens of focal length f1 = 0.3 m and was imaged to SLM 2 by means of a 4f system with lenses of f2 = f3 = 0.3 m. SLM 2 removed the remaining phase from the incident beam resulting in a Gaussian beam

with a flat phase. A Point Grey Firefly camera was used to measure the beam profiles at various positions. Whilst it is possible to determine the M^2 of beam from only two measurements of its waist using Eq. 1.44, this method is known to introduce large error into the measurement. For this reason, best practice dictates that the M^2 of a beam be determined by passing the beam through a lens and measuring its waist at several points as it propagates through the focus [3.54]. A quadratic polynomial is then fitted to these data points, and this fitted curve is equated to Eq. 1.49 [3.55]. From this the M^2 can be calculated by equating the quadratic coefficients. Consequently, to measure the M^2 value of the final beam, lens f4 having a focal length of 0.2 m was inserted into the experimental setup and the camera was moved on a rail through the waist of the beam. The second moment widths were then calculated from the captured images, from which the M^2 could be inferred.

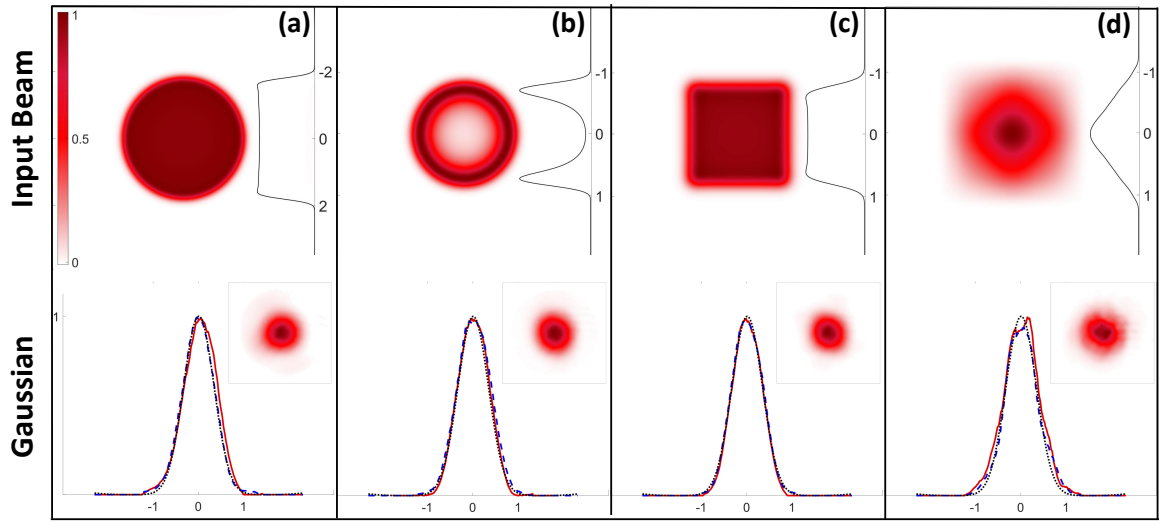


Fig. 3.8 Input beams shown as an intensity and profile, each with a flat phase, and the measured Gaussian output beam, shown for the four tested cases: (a) radial Super-Gaussian, (b) radial annulus, (c) Cartesian Super-Gaussian and (d) Cartesian linear, a beam with a linear intensity gradient. The examples cover Radial and Cartesian symmetry in high M^2 initial beams. The Gaussian beams are shown as cross-sectional profiles for x (blue dashed) and y (red solid), with the black dotted profiles as the theoretical prediction. The insets show the measured camera intensities. All profiles are plotted on an axis in millimetres.

Table 3.3 The M^2 values of the initial beam profiles used in the experiment, and the predicted brightness enhancement factor, η.

Profile	M^2	$\eta = (M^2)^2$
Super-Gaussian (radial & Cartesian)	3.64	13.25
radial annulus	16.71	279.22
Cartesian linear	3.90	15.21

3.7 Experimental results II

The concept was tested using the initial amplitude profiles given in Table 3.3. These profiles were selected for their non-propagation invariant nature and high M^2 value. These beams serve as a proof-of-principle, demonstrating the viability of the method in a way which is applicable to all non-propagation invariant beams having high M^2 values. Table 3.3 shows the M^2 values of the beams as well as the theoretical brightness

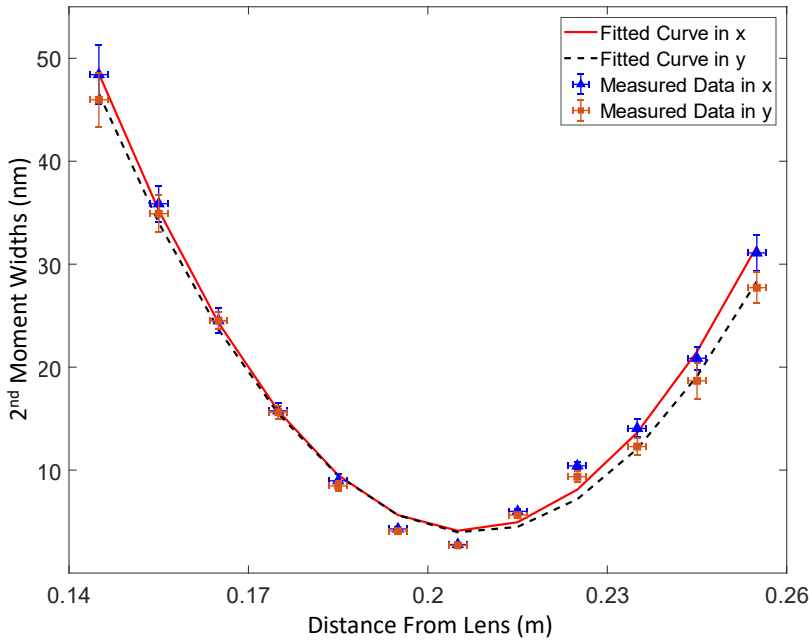


Fig. 3.9 The 2nd moment width for the Gaussian beam as a function of propagation distance from the focusing lens, shown as measured data and fitted curves. Fitting the data to the equation $W^2(z) = W_0^2 + \left(M^2\right)^2 \times [\lambda/(\pi W_0)]^2 (z - z_0)^2$ allows the unknown parameters to be inferred, including the M^2. This example plot is for the radial Super-Gaussian to Gaussian case and shows a beam quality factor improvement from $M^2 = 3.64$ to $M^2 = 1.06 \pm 0.05$

.

enhancement that would be expected in a lossless implementation. The M^2 of the Super-Gaussian was calculated with the equation given in Table 1.1. The annular and linear values were calculated by a numerical propagation simulation and quadratic curve fitting, as explained previously. The measured beams are shown in Fig. 3.8, which shows excellent conversion from the initially structured beams to a Gaussian beam for all cases, with correlation factors in excess of 98%. The Gaussian nature was further corroborated by the full propagation analysis shown in Fig. 3.9, which was used to determine the M^2 for the radial Super-Gaussian to Gaussian example. A beam quality factor decrease from $M^2 = 3.64$ to $M^2 = 1.06 \pm 0.05$ was found, yielding a brightness enhancement of $\eta = 11.79 \pm 1.20$ when ignoring the SLM losses, in close agreement with the prediction of ≈ 13.

The near perfect correlation between the measured and predicted Gaussian beams shows the viability of the method for improving the beam quality factor. Hence the approach can enhance the brightness significantly. This is not in contradiction to the prior argument that the beam quality could not be improved by binary diffractive optics [3.41]. In that scenario, the binary optics were envisaged to flip the phase jumps in higher-order modes and by propagation convert them to Gaussian-like beams in the far field. This does not improve beam quality or brightness. Instead, the approach presented here employs a two-step conformal mapping to transform one beam into another, where the final beam can be Gaussian. Thus both the principle and execution differ from Ref. [3.41]. This approach is sufficiently general so as to be applicable to beams with novel vectorial characteristics [3.4;3.5] by implementing the solution with meta-surfaces or by using the present approach on each polarization component separately.

3.8 Summary of chapter 3

In Chp. 3, LCoS SLMs were used to manipulate the amplitude and phase of light. The theory for a versatile beam shaping technique which can losslessly convert almost any input beam into a wide variety of output beams was presented. This theory was based on a two-step, phase-only method derived from conformal mapping, and represents a novel expansion on previous work. Experimental results confirming the efficacy and generality of the method are presented. The method was then reversed, to remove the structure of beams, converting structured beams back to the lowest M^2 beam, a Gaussian. The concept was demonstrated experimentally and showed that a significant brightness enhancement is possible, up to a factor of M^4, indicating that the more structured the initial beam the greater the enhancement.

Having demonstrated the reduction in M^2 of structured beams, Chp. 4 will focus on the remaining topics outlined in Sec. 1.4: The effects of structured light on thermal stress and phase aberrations, and using DMDs as experimental simulators of high-energy systems.

References

3.1 A. M. Weiner, "Ultrafast optical pulse shaping: A tutorial review," *Optics Communications*, vol. 284, no. 15, pp. 3669–3692, 2011.

3.2 ——, "Femtosecond pulse shaping using spatial light modulators," *Review of scientific instruments*, vol. 71, no. 5, pp. 1929–1960, 2000.

3.3 J. Chen, C. Wan, and Q. Zhan, "Vectorial optical fields: recent advances and future prospects," *Science Bulletin*, vol. 63, no. 1, pp. 54 – 74, 2018.

3.4 Q. Zhan, "Cylindrical vector beams: from mathematical concepts to applications," *Advances in Optics and Photonics*, vol. 1, no. 1, pp. 1–57, 2009.

3.5 C. Rosales-Guzmán, B. Ndagano, and A. Forbes, "A review of complex vector light fields and their applications," *Journal of Optics*, vol. 20, no. 12, p. 123001, 2018. [Online]. Available: http://iopscience.iop.org/article/10.1088/2040-8986/aaeb7d

3.6 J. A. Hoffnagle and C. M. Jefferson, "Design and performance of a refractive optical system that converts a gaussian to a flattop beam," *Applied Optics*, vol. 39, no. 30, pp. 5488–5499, 2000.

3.7 J. Turunen and F. Wyrowski, "Diffractive optics for industrial and commercial applications," *Diffractive Optics for Industrial and Commercial Applications, by Jari Turunen (Editor), Frank Wyrowski (Editor), pp. 440. ISBN 3-527-40100-8. Wiley-VCH, March 1998.*, p. 440, 1998.

3.8 H. Ma, Z. Liu, P. Zhou, X. Wang, Y. Ma, and X. Xu, "Generation of flat-top beam with phase-only liquid crystal spatial light modulators," *Journal of Optics*, vol. 12, no. 4, p. 045704, 2010.

3.9 M. W. Beijersbergen, R. P. C. Coerwinkel, M. Kristensen, and J. P. Woerdman, "Helical-wave-front laser-beams produced with a spiral phaseplate," *Optics Communications*, vol. 112, no. 5-6, pp. 321–327, 1994.

3.10 A. Rubano, F. Cardano, B. Piccirillo, and L. Marrucci, "Q-plate technology: a progress review," *Journal of the Optical Society of America B*, vol. 36, no. 5, pp. D70–D87, 2019.

3.11 E. Brasselet, N. Murazawa, H. Misawa, and S. Juodkazis, "Optical vortices from liquid crystal droplets," *Physical Review Letters*, vol. 103, no. 10, p. 103903, 2009.

3.12 N. Heckenberg, R. McDuff, C. Smith, and A. White, "Generation of optical phase singularities by computer-generated holograms," *Optics Letters*, vol. 17, no. 3, pp. 221–223, 1992.

3.13 A. Forbes, *Laser beam propagation: generation and propagation of customized light*. CRC Press, 2014.

3.14 M. J. Padgett, "Orbital angular momentum 25 years on," *Optics Express*, vol. 25, no. 10, pp. 11 265–11 274, 2017.

3.15 Y. Shen, X. Wang, Z. Xie, C. Min, X. Fu, Q. Liu, M. Gong, and X. Yuan, "Optical vortices 30 years on: OAM manipulation from topological charge to multiple singularities," *Light: Science & Applications*, vol. 8, no. 1, pp. 1–29, 2019.

3.16 E. Karimi, G. Zito, B. Piccirillo, L. Marrucci, and E. Santamato, "Hypergeometric-Gaussian modes," *Optics Letters*, vol. 32, no. 21, pp. 3053–3055, 2007.

3.17 B. Sephton, A. Dudley, and A. Forbes, "Revealing the radial modes in vortex beams," *Applied Optics*, vol. 55, no. 28, pp. 7830–7835, 2016.

3.18 M. Rafayelyan and E. Brasselet, "Laguerre-Gaussian modal q-plates," *Optics Letters*, vol. 42, no. 10, pp. 1966–1969, 2017.

3.19 O. Bryngdahl, "Geometrical transformations in optics," *Journal of the Optical Society of America*, vol. 64, no. 8, pp. 1092–1099, 1974.

3.20 P. W. Rhodes and D. L. Shealy, "Refractive optical systems for irradiance redistribution of collimated radiation: their design and analysis," *Applied Optics*, vol. 19, no. 20, pp. 3545–3553, 1980.

3.21 F. M. Dickey, *Laser beam shaping: theory and techniques*. CRC press, 2018.

3.22 J. Jiang, D. Sell, S. Hoyer, J. Hickey, J. Yang, and J. A. Fan, "Free-form diffractive metagrating design based on generative adversarial networks," *ACS Nano*, vol. 13, no. 8, pp. 8872–8878, 2019.

3.23 J. L. Kreuzer, "Coherent light optical system yielding an output beam of desired intensity distribution at a desired equiphase surface," Nov. 4 1969, US Patent 3,476,463.

3.24 ——, "Laser light redistribution in illuminating optical signal processing systems," *Optical and Electro-Optical Information Processing*, p. 365, 1965.

3.25 B. R. Frieden, "Lossless conversion of a plane laser wave to a plane wave of uniform irradiance," *Applied Optics*, vol. 4, no. 11, pp. 1400–1403, 1965.

3.26 F. M. Dickey and S. C. Holswade, "Gaussian laser beam profile shaping," *Optical Engineering*, vol. 35, 1996.

3.27 D. Shafer, "Gaussian to flat-top intensity distributing lens," *Optics & Laser Technology*, vol. 14, no. 3, pp. 159–160, 1982.

3.28 S. Jahan and M. Karim, "Refracting systems for Gaussian-to-uniform beam transformations," *Optics & Laser Technology*, vol. 21, no. 1, pp. 27–30, 1989.

3.29 C.-Y. Han, Y. Ishii, and K. Murata, "Reshaping collimated laser beams with Gaussian profile to uniform profiles," *Applied Optics*, vol. 22, no. 22, pp. 3644–3647, 1983.

3.30 C. Dorrer and J. D. Zuegel, "Design and analysis of binary beam shapers using error diffusion," *Journal of the Optical Society of America B*, vol. 24, no. 6, pp. 1268–1275, 2007.

3.31 Y. Kawamura, Y. Itagaki, K. Toyoda, and S. Namba, "A simple optical device for generating square flat-top intensity irradiation from a Gaussian laser beam," *Optics Communications*, vol. 48, no. 1, pp. 44–46, 1983.

3.32 F. M. Dickey and S. C. Holswade, "Beam shaping: a review," in *Laser Beam Shaping Applications*. CRC Press, 2018, pp. 269–305.

3.33 A. N. K. Reddy and V. Pal, "Robust design of diffractive optical elements for forming flat-top beams with extended depth of focus," *Applied Physics B*, vol. 125, no. 12, p. 231, 2019.

3.34 G. C. G. Berkhout, M. P. J. Lavery, J. Courtial, M. W. Beijersbergen, and M. J. Padgett, "Efficient sorting of orbital angular momentum states of light," *Physical Review Letters*, vol. 105, p. 153601, 2010.

3.35 A. Dudley, Y. Li, T. Mhlanga, M. Escuti, and A. Forbes, "Generating and measuring nondiffracting vector Bessel beams." *Optics Letters*, vol. 38, pp. 3429–3432, 2013.

3.36 A. Trichili, T. Mhlanga, Y. Ismail, F. S. Roux, M. McLaren, M. Zghal, and A. Forbes, "Detection of Bessel beams with digital axicons," *Optics Express*, vol. 22, no. 14, pp. 17 553–17 560, 2014.

3.37 Y. Zhou, J. Zhao, Z. Shi, S. M. H. Rafsanjani, M. Mirhosseini, Z. Zhu, A. E. Willner, and R. W. Boyd, "Hermite-Gaussian mode sorter," *Optics Letters*, vol. 43, no. 21, pp. 5263–5266, 2018.

3.38 N. K. Fontaine, R. Ryf, H. Chen, D. T. Neilson, K. Kim, and J. Carpenter, "Laguerre-Gaussian mode sorter," *Nature Communications*, vol. 10, no. 1, pp. 1–7, 2019.

3.39 F. Bouchard, N. H. Valencia, F. Brandt, R. Fickler, M. Huber, and M. Malik, "Measuring azimuthal and radial modes of photons," *Optics Express*, vol. 26, no. 24, pp. 31 925–31 941, 2018.

3.40 L. Romero and F. Dickey, "Lossless laser beam shaping," *Journal of the Optical Society of America A*, vol. 13, no. 4, pp. 751–760, 1996.

3.41 A. Siegman, "Binary phase plates cannot improve laser beam quality," *Optics Letters*, vol. 18, no. 9, pp. 675–677, 1993.

3.42 R. Oron, N. Davidson, A. A. Friesem, and E. Hasman, "Continuous-phase elements can improve laser beam quality," *Optics Letters*, vol. 25, no. 13, pp. 939–941, 2000.

3.43 J. Alda, "Quality improvement of a coherent and aberrated laser beam by using an optimum and smooth pure phase filter," *Optics Communications*, vol. 192, no. 3-6, pp. 199–204, 2001.

3.44 A. Parent, M. Morin, and P. Lavigne, "Propagation of Super-Gaussian field distributions," *Optical and Quantum Electronics*, vol. 24, no. 9, pp. S1071–S1079, 1992.

3.45 S. Saghafi and C. Sheppard, "The beam propagation factor for higher order Gaussian beams," *Optics Communications*, vol. 153, no. 4-6, pp. 207–210, 1998.

3.46 H. Rubinsztein-Dunlop, A. Forbes, M. V. Berry, M. R. Dennis, D. L. Andrews, M. Mansuripur, C. Denz, C. Alpmann, P. Banzer, T. Bauer, E. Karimi, L. Marrucci, M. Padgett, M. Ritsch-Marte, N. M. Litchinitser, N. P. Bigelow, C. Rosales-Guzmán, A. Belmonte, J. P. Torres, T. W. Neely, M. Baker, R. Gordon, A. B. Stilgoe, J. Romero, A. G. White, R. Fickler, A. E. Willner, G. Xie, B. McMorran, and A. M. Weiner, "Roadmap on structured light," *Journal of Optics*, vol. 19, no. 1, p. 013001, 2017. [Online]. Available: http://stacks.iop.org/2040-8986/19/i=1/a=013001

3.47 S. Ngcobo, K. Aït-Ameur, N. Passilly, A. Hasnaoui, and A. Forbes, "Exciting higher-order radial Laguerre–Gaussian modes in a diode-pumped solid-state laser resonator," *Applied Optics*, vol. 52, no. 10, pp. 2093–2101, 2013.

3.48 T. Bell, A. Hasnaoui, K. Ait-Ameur, and S. Ngcobo, "Excitation of high-radial-order Laguerre-Gaussian modes in a solid-state laser using a lower-loss digitally controlled amplitude mask," *Journal of Optics*, vol. 19, no. 10, p. 105604, 2017.

3.49 R. Borghi and M. Santarsiero, "M^2 factor of Bessel-Gauss beams," *Optics Letters*, vol. 22, no. 5, pp. 262–264, 1997.

3.50 R.-P. Chen and C.-F. Ying, "Beam propagation factor of an Airy beam," *Journal of Optics*, vol. 13, no. 8, p. 085704, 2011.

3.51 A. E. Siegman, "How to (maybe) measure laser beam quality," in *Diode Pumped Solid State Lasers: Applications and Issues*. Optical Society of America, 1998, p. MQ1.

3.52 C. Rosales-Guzmán and A. Forbes, *How to shape light with spatial light modulators*. SPIE Press, 2017.

3.53 A. Forbes, A. Dudley, and M. McLaren, "Creation and detection of optical modes with spatial light modulators," *Advances in Optics and Photonics*, vol. 8, pp. 200–227, 2016.

3.54 "Lasers and laser-related equipment–test methods for laser beam widths, divergence angles and beam propagation ratios–part 1: Stigmatic and simple astigmatic beams," *ISO 11146-1: 2005 (E)*, 2005.

3.55 A. E. Siegman, "Defining, measuring, and optimizing laser beam quality," in *Laser Resonators and Coherent Optics: Modeling, Technology, and Applications*, vol. 1868. International Society for Optics and Photonics, 1993, pp. 2–12.

Chapter 4

Structured light and thermal effects

This chapter is based on the publications
Scholes, S. *and Forbes, A., Thermal aberrations and structured light I: Analytical model for structured pumps and probes. Submitted to Applied Physics B at the time of writing.*
and
Scholes, S. *and Forbes, A., Thermal aberrations and structured light II: Experimental simulation with DMDs. Submitted to Applied Physics B at the time of writing.*
Author S.S derived the theoretical model, performed the experiments and wrote the associated publications with supervision provided by author A.F.

The aims of this chapter are two-fold. The first is to explore the interaction between the structure of a beam, the thermal effects in a medium and the brightness of a beam. The second is to demonstrate an experimental simulator of high-energy laser sources using a DMD.

As more energy is added to the cavity of a solid-state laser, temperature-dependent phase aberrations and mechanical stresses develop in the lasing medium. These deleterious thermal effects place an upper limit on the energy which can be added to a lasing cavity, and are a major impediment in the development of higher-brightness lasers. The thermally-induced phase increases the divergence of the output beam and degrades its ability to be focused at a target plane, while high temperatures in the gain media lead to non-linear effects such as phonon-phonon and Brillouin scattering [4.1;4.2;4.3;4.4] . The maximum energy which may be added to the system is ultimately restricted by the thermal stresses induced in the lasing medium as a result of thermal gradients. If the stresses exceed the fracture limit of the lasing medium, it will mechanically fail. Even highly transmissive or reflective media (lenses and mirrors) are susceptible to thermal aberrations, since the

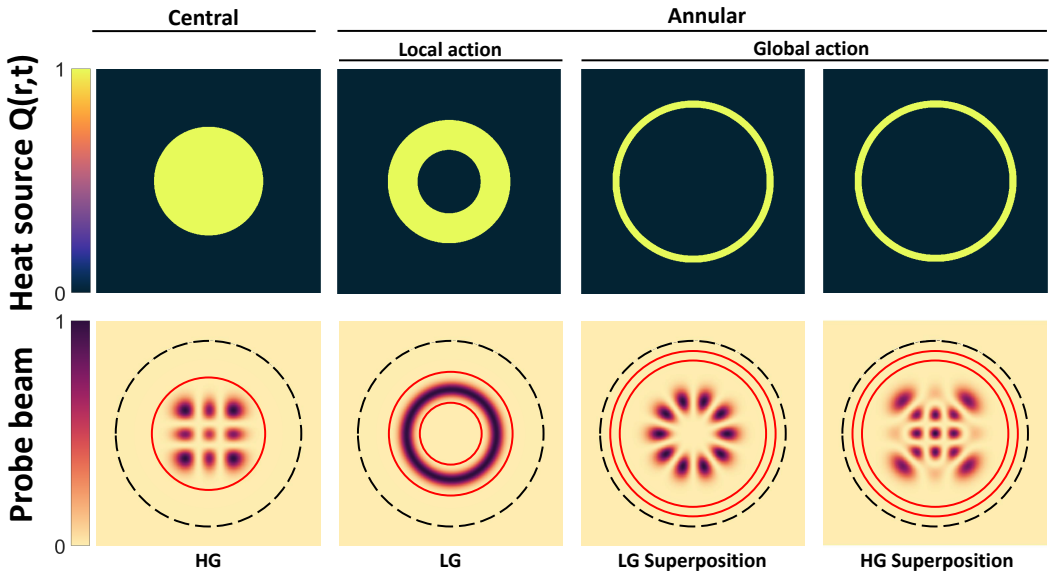


Fig. 4.1 The cases this chapter examines. The analysis makes use of an abstract heat source $Q(r,t)$ and probe beams. The heat source is separated into two categories, central and annular. The annular case is further divided into two sub categories, the local action and the global action. The local action refers to an examination of the thermal phase-only within the annular region under heating, while the global action refers to the examination of the thermal phase for the entire optic. The red circles indicate the location of the heat source relative to the probe beam while the dotted black line indicates the circumference of the optic. The central heat source is probed with an HG beam. The local action of the annular source is probed with an LG beam. The global action of the annular source is probed with both superpositions of LG and HG beams.

detrimental effects introduced to the beam are proportional to the gradient of the temperature profile in the medium, not the absolute value [4.5;4.6;4.7;4.8]. Historically, reports on thermal aberrations predominantly characterise the phase of the heated media under idealised thermal conditions, such as steady state temperature profiles [4.8;4.9;4.10;4.11;4.12] although general analytical thermal solutions have been published [4.13;4.14]. Since thermal aberrations are typically dominated by a thermal lensing effect, the majority of research is directed at this topic [4.12;4.14;4.15;4.16;4.17;4.18;4.19;4.20] with some more general examinations available [4.9;4.21]. A review of thermal effects in laser cavities is presented in Ref. [4.22]. This chapter presents a versatile analytical description for the temperature profile $u(r,t)$ of a radially-symmetric medium undergoing heating, which leads to a complete characterisation of the phase $\phi(r,t)$ and the thermally-induced stress. These characterisations are used to design beam structures which reduce deleterious thermal effects and so increase brightness. Experimental exploration of the relationship between thermal effects and beam structure has proved challenging, as explained in Sec. 1.3. This chapter contains

what is believed to be the first demonstration of a fully configurable, low power physical simulator for high-energy sources. Specifically, a Digital Micro-mirror Device (DMD) and Computer Generated Holograms (CGHs) are used, foregoing the use of specific optics and physical heat sources entirely. In doing so, a proof-of-principle is presented for an experimental system capable of producing beams with properties identical to those yielded by a wide variety of materials, heat sources and applications at a fraction of the cost and complexity.

This chapter examines the thermal stress and thermal phase aberrations for a radially-symmetric optic of radius R, using probe beams and an abstract optical heat source $Q(r,t)$. The heat sources and corresponding probe beams are shown in Fig. 4.1. Specifically, two categories of heat source, central and annular are considered, as shown in Fig. 4.1. First, a centrally-positioned optical heat source $Q_c(r,t)$ is examined and is used to develop the fundamentals of the approach. Specifically, a general characterisation of the temperature of an optic under such heating (Sec. 4.1.1) is presented. This characterisation is used to derive expressions for the phase (Sec. 4.1.2) and stress (Sec. 4.1.3) induced by this heating. The effect of the thermal phase on an HG probe beam passing through the centre of the optic is examined. Second, the effect of an annular heat source $Q_{an}(r,t)$ on the stress (Sec. 4.2.1) experienced by an optic is explored. The thermal phase introduced by this annular source is examined for two cases, the 'local action' (Sec. 4.5.1) and the 'global action' (Sec. 4.5.2). The local action refers to an examination of the thermal phase-only within the annular region under heating, while the global action refers to the examination of the thermal phase for the entire optic. The important distinctions between the phase descriptions in these cases is highlighted, particularly in their interpretation as physical quantities, such as effective focal length. The local action is examined with LG probe beams whilst the global action is probed using superpositions of both HG and LG beams. HG and LG beams are used for the following reasons: they provide a beam which can be easily configured to match the spatial structure of an applied heat source; their ubiquity in the structured light field[4.23] makes them a good test case for a proof-of-principle demonstration, and, as natural transverse modes of laser cavities[4.24;4.25] their examination here provides context for this work in terms of high-energy laser sources. Last, a discussion elaborating upon the physical interpretation of the approach and the impact of the findings on laser brightness is presented.

4.1 A central heat source

4.1.1 The temperature profile u(r,t)

The temperature profile $u(r,t)$ in polar coordinates for an optic undergoing heating is given by the solution to the non-homogenous heat equation given by

$$\frac{\partial u(r,\theta,t)}{\partial t} - \varrho\nabla^2 u(r,\theta,t) = Q(r,\theta,t). \tag{4.1}$$

Recall ∇^2 is the radial Laplacian given by

$$\nabla^2 = \frac{\partial^2}{\partial r^2} + \frac{1}{r}\frac{\partial}{\partial r} + \frac{1}{r^2}\frac{\partial^2}{\partial\theta^2}. \tag{4.2}$$

ϱ defines the thermal properties of the medium and is given by

$$\varrho = \frac{k_T}{\rho c_p}, \tag{4.3}$$

where k_T is the thermal conductivity, ρ is the density and c_p is the specific heat capacity. Units and quantities for these parameters are presented in Table 4.1. $Q(r,\theta,t)$ is referred to as the source term and can be expressed in terms of thermodynamic relationships as

$$Q(r,\theta,t) = \xi\nu\frac{du}{dt}, \tag{4.4}$$

with

$$du = \frac{dE}{\rho c_p A}. \tag{4.5}$$

Hence

$$\begin{aligned} Q(r,\theta,t) &= \frac{\xi\nu}{\rho c_p}\frac{dE}{Adt}, \\ Q(r,\theta,t) &= \frac{\xi\nu}{\rho c_p} I(r,\theta,t). \end{aligned} \tag{4.6}$$

Here, ξ is the absorption coefficient and ν is the fractional heat load. These constants together capture what fraction of the intensity $I(r,\theta,t)$ of the illuminating beam is absorbed by the optic as heat. To derive a time-dependent analytic solution to Eq. 4.1, the technique of Eigen-function expansion is used. To begin, the Eigen-functions for Eq. 4.1 are found

by solving the associated homogenous heat equation

$$\frac{\partial u(r,\theta,t)}{\partial t} - \varrho \nabla^2 u(r,\theta,t) = 0. \tag{4.7}$$

Employing separation of variables

$$u(r,\theta,t) = R(r)\Theta(\theta)T(t). \tag{4.8}$$

Substituting Eq. 4.8 into Eq. 4.7, dividing by $\varrho R(r)\Theta(\theta)T(t)$ and multiplying by r^2 puts Eq. 4.7 into seperated form

$$\frac{r^2}{\varrho T}\frac{\partial T}{\partial t} = \frac{r^2}{R}\frac{\partial^2 R}{\partial r^2} + \frac{r}{R}\frac{\partial R}{\partial r} + \frac{1}{\Theta}\frac{\partial^2 \Theta}{\partial \theta^2}. \tag{4.9}$$

Let

$$\frac{1}{\Theta}\frac{\partial^2 \Theta}{\partial \theta^2} = -n^2, \tag{4.10}$$

hence

$$\begin{aligned} &\frac{\partial^2 \Theta}{\partial \theta^2} + n^2\Theta = 0, \\ &\Theta(\theta) = A\cos(n\theta) + B\sin(n\theta). \end{aligned} \tag{4.11}$$

Let

$$\frac{1}{\varrho T}\frac{\partial T}{\partial t} = -\mu^2, \tag{4.12}$$

hence

$$\begin{aligned} &\frac{\partial T}{\partial t} = -\varrho\mu^2 T, \\ &T(t) = C\exp(-\varrho\mu^2 t). \end{aligned} \tag{4.13}$$

Together Eq. 4.10 and Eq. 4.12 give

$$r^2\frac{\partial^2 R}{\partial r^2} + r\frac{\partial R}{\partial r} + (r^2\mu^2 + n^2)R = 0. \tag{4.14}$$

Equation 4.14 is the Bessel equation, the solution to which is a linear combination of Bessel functions of the first and second kind

$$R(r) = DJ_0(\mu r) + EY_0(\mu r). \tag{4.15}$$

Applying the following boundary conditions

$$u(R,t) = 0^\circ C, \tag{4.16}$$

gives

$$R(r) = DJ_0(\mu r). \tag{4.17}$$

For radially-symmetric problems, Eq. 4.11 may be neglected, reducing the solution of Eq. 4.9 to

$$u(r,t) = \sum_{n=1}^{\infty} p_n J_0(\mu_n r)\exp(-\Delta t). \tag{4.18}$$

Here $\mu_n = \aleph_n/R$, $\aleph_n$ is the n^{th} root of the 0^{th} order Bessel function of the first kind J_0. R is the radius of the domain over which the solution applies and $\Delta = \varrho\mu_n^2$. p_n is the initial temperature distribution at time $t^\dagger < t$ derived using the orthogonality of the Bessel function

$$\int_0^R J_0(\mu_n)J_0(\mu_m)r\,dr = \frac{R^2}{2}\delta_{m,n}[J_1(\aleph_n)]^2. \tag{4.19}$$

$\delta_{m,n}$ is the Kronecker Delta. For $t^\dagger = 0$

$$\begin{aligned}
\int_0^R \sum_{n=1}^{\infty} p_n J_0(\mu_n r) r J_0(\mu_m r)\,dr &= \int_0^R u(r,0) r J_0(\mu_m)\,dr, \\
\frac{p_n R^2}{2}[J_1(\aleph_n)]^2 &= \int_0^R u(r,0) r J_0(\mu_m)\,dr, \\
p_n &= \frac{2}{R^2[J_1(\aleph_n)]^2}\int_0^R u(r,0) r J_0(\mu_m)\,dr.
\end{aligned} \tag{4.20}$$

Hence the Eigen-function for this system is $J_0(\mu_n r)$. Assume the following form for the solution to $Q(r,t)$.

$$Q(r,t) = \sum_{n=1}^{\infty} q_n R_n(r). \tag{4.21}$$

Replacing $R_n(r)$ with the Eigen-fuction

$$Q(r,t) = \sum_{n=1}^{\infty} q_n J_0(\mu_n r). \tag{4.22}$$

Again, using Eq. 4.19 to isolate the function q_n

$$\begin{aligned}\int_0^R Q(r,t)rJ_0(\mu_n r)dr &= \int_0^R \sum_{n=1}^{\infty} q_n J_0(\mu_n r)rJ_0(\mu_m r)dr,\\ \int_0^R Q(r,t)rJ_0(\mu_n r)dr &= q_n \frac{R^2}{2}(J_1(\aleph_n))^2,\end{aligned} \tag{4.23}$$

$$q_n = \frac{2}{(RJ_1(\aleph_n))^2}\int_0^R Q(r,t)rJ_0(\mu_n r)dr. \tag{4.24}$$

The solution $u(r,t)$ to Eq. 4.1 is assumed to have the form

$$u(r,t) = \sum_{n=1}^{\infty} a_n(t)R_n(r). \tag{4.25}$$

Substituting this form back into Eq. 4.1 gives

$$\frac{\partial u}{\partial t} = \sum_{n=1}^{\infty} \frac{\partial a_n}{\partial t}R_n, \tag{4.26}$$

and

$$\nabla^2 u = \sum_{n=1}^{\infty} a_n \nabla^2 R_n. \tag{4.27}$$

It should be noted that Eq. 4.27 implicitly assumes that the derivative of an infinite sum is equivalent to the sum of its derivatives. This is generally true for partial differential equations with homogeneous boundary conditions,

$$\begin{aligned}\sum_{n=1}^{\infty} \frac{\partial a_n}{\partial t}R_n - \varrho(\sum_{n=1}^{\infty} a_n \nabla^2 R_n) &= Q(r,t),\\ \sum_{n=1}^{\infty} \frac{\partial a_n}{\partial t}R_n - \varrho(\sum_{n=1}^{\infty} a_n \nabla^2 R_n) &= \sum_{n=1}^{\infty} q_n R_n(r).\end{aligned} \tag{4.28}$$

Since $R_n(r)$ is an Eigen-function it obeys the relationship

$$R_n^{''}(r) + \frac{1}{r}R_n^{'}(r) + \mu_n^2 R_n = 0. \tag{4.29}$$

Here the prime $'$ indicates the derivative. Substituting gives

$$\begin{aligned}\sum_{n=1}^{\infty}\frac{\partial a_n}{\partial t}R_n-\varrho(\sum_{n=1}^{\infty}a_n(-(\mu_n)^2R_n))&=\sum_{n=1}^{\infty}q_nR_n,\\ \sum_{n=1}^{\infty}[R_n(\frac{\partial a_n}{\partial t}+\varrho\mu_n^2a_n-q_n)]&=0,\\ \sum_{n=1}^{\infty}[J_0(\mu_nr)(\frac{\partial a_n}{\partial t}+\Delta a_n-q_n)]&=0.\end{aligned}\tag{4.30}$$

Since $J_0(\mu_n r)\neq 0$ for all r, $\frac{\partial a_n}{\partial t}+\Delta a_n-q_n=0$. This is now an ordinary differential equation. Consider also the initial condition

$$\begin{aligned}u(r,0)&=0,\\ \sum_{n=1}^{\infty}a_n(0)R_n(r)&=0,\\ \sum_{n=1}^{\infty}a_n(0)J_0(\mu_nr)&=0.\end{aligned}\tag{4.31}$$

thus

$$a_n(0)=0.\tag{4.32}$$

This yields

$$\frac{\partial a_n}{\partial t}+\Delta a_n-q_n=0,\tag{4.33}$$

with

$$a_n(0)=0,\tag{4.34}$$

$$\begin{aligned}\frac{\partial a_n}{\partial t}&=q_n-\Delta a_n,\\ \frac{\frac{\partial a_n}{\partial t}}{q_n-\Delta a_n}&=1,\\ \int\frac{\frac{\partial a_n}{\partial t}}{q_n-\Delta a_n}dt&=\int 1dt,\\ -\frac{\log(q_n-\Delta a_n)}{\Delta}&=t+C_1,\\ -\log(q_n-\Delta a_n)&=(t+C_1)\Delta.\end{aligned}\tag{4.35}$$

Therefore

$$a_n(t)=\frac{[-\exp(-\Delta t)+1]q_n}{\Delta}.\tag{4.36}$$

For non-zero initial conditions where p_n is non-trivial, Eq. 4.36 becomes

$$a_n(t) = \frac{\exp(-\Delta t)\{[-1+\exp(\Delta t)]q_n + \Delta p_n\}}{\Delta}. \tag{4.37}$$

Thus finally

$$u(r,t) = \sum_{n=1}^{\infty} \frac{\exp(-\Delta t)\{[-1+\exp(\Delta t)]q_n + \Delta p_n\}}{\Delta} J_0(\mu_n r), \tag{4.38}$$

with

$$q_n(t) = \frac{2}{[RJ_1(\aleph_n)]^2} \int_0^R Q(r,t) r J_0(\mu_n r) dr, \tag{4.39}$$

and

$$p_n(t) = \frac{2}{[RJ_1(\aleph_n)]^2} \int_0^R u(r,t^\dagger) r J_0(\mu_n r) dr, \tag{4.40}$$

for $t^\dagger < t$.

Equation 4.38 shows that when heat is no longer applied, the source term q_n goes

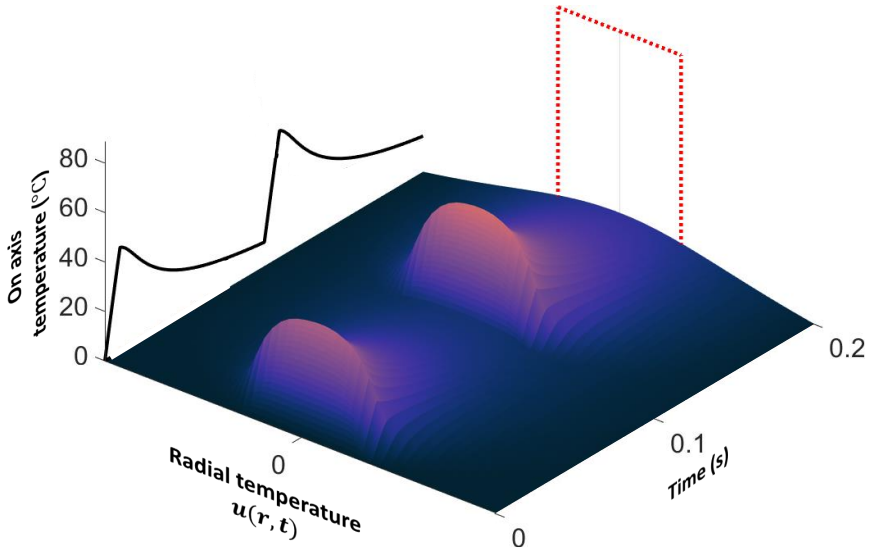


Fig. 4.2 The spatial and temporal temperature profile of a Tm:YLF rod with a central quasi-continuous uniform-intensity source, where each pulse lasts 0.01 s with a 0.09 s cooling period. The raised panels at the boundaries of the surface plots show line plots of the on axis temperature over time for the uniform-intensity source together with the structure of the heat source (red dotted).

to 0 and the solution reduces to the homogeneous heat equation (Eq. 4.18). Conversely, as time under heating advances the impact of the initial temperature distribution p_n falls away as the source term comes to dominate the equation. Consider a centrally located heat source $Q_c(r,t)$ of waist ω_0 with a uniform-intensity profile defined by

$$Q_c(r,t) = \left\{ \begin{array}{ll} \frac{\xi\nu}{\rho c_p}\frac{\hat{P}}{\pi\omega_0^2}, & \text{for } 0 \le r \le \omega_0 \\ 0, & \text{otherwise} \end{array} \right\}. \tag{4.41}$$

For uniform-intensity central heat sources, Eq. 4.39 has the analytic solution

$$q_n(t) = \frac{2}{[RJ_1(\aleph_n)]^2}\frac{\xi\nu}{\rho c_p}\frac{\hat{P}}{\pi\omega_0^2}\frac{\omega_0 J_1(\omega_0\mu_n)}{\mu_n}. \tag{4.42}$$

Figure 4.2 illustrates the complete spatial and temporal solution given by Eq. 4.38 for a quasi-continuous heat source with the form of $Q_c(r,t)$ illuminating a Tm:YLF rod. The parameters used in the calculation are given in Table. 4.1 [4.26]. In Fig. 4.2 note the exponential decay of the on axis temperature during the cooling period a result of the $\exp(-\Delta t)$ component of Eq. 4.18. Throughout this chapter a Tm:YLF rod is used for the purposes of illustration, but it could be replaced by any other material by modification of ϱ. Hav-

Table 4.1 Material constants used in the simulation for a Tm:YLF rod

Parameter	**Symbol**	**Unit**	**Value**
Heat source radius	ω_0	m	470×10^{-6}
Rod radius	R	m	1.5×10^{-3}
Rod length	l	m	5×10^{-3}
Absorption coefficient	ξ	m^{-1}	143
Thermal conductivity	k_T	$W.m^{-1}.K^{-1}$	7.2
Fractional heat load	ν		0.33
Density	ρ	$kg.m^{-1}$	3990
Specific heat capacity	c_p	$J.kg^{-1}.K^{-1}$	790
Heat source power	$\hat{P}$	W	200
Refractive index per unit temperature	$\frac{\partial n'}{\partial u}$	K^{-1}	-66×10^{-7}
Linear expansion coefficient	$\breve{\gamma}$	K^{-1}	13×10^{-6}
Young's modulus	Y	GPa	75
Poisson's ratio	$\breve{\nu}$		0.33
Fracture limit		Mpa	40

ing characterised the temperature profile in the optic, the thermal phase aberrations (Sec. 4.1.2) and thermal stress (Sec. 4.1.3) introduced by this heating can be explored.

4.1.2 Thermal phase aberrations

The thermally-induced phase $\phi(r,t)$ that is introduced to a radially-symmetric optic is

$$\phi(r,t) = \phi_0 + kl\frac{\partial n'}{\partial u}\delta u(r,t). \tag{4.43}$$

Here ϕ_0 is a constant phase shift which may be ignored, $k = 2\pi/\lambda$, l is the depth of the optic in z and $\frac{\partial n'}{\partial u}$ is the change in refractive index per unit temperature. If the perimeter of the optic is held at a constant temperature of 0°C (Eq 4.16), then the temperature difference $\delta u(r,t)$ reduces to $u(r,t)$. Hence

$$\phi(r,t) = kl\frac{\partial n'}{\partial u}u(r,t). \tag{4.44}$$

It is clear from Eq. 4.44 that the phase introduced to the optic is wholly dependent on the temperature distribution $u(r,t)$. By inserting Eqs. 4.38, 4.39 and 4.40 back into Eq. 4.44 it is possible to fully determine the phase present in an optic when heated by a general heat source for an arbitrary period of time. However, such a description lacks an intuitive physical meaning. To address this, the phase $\phi(r,t)$ is characterised in the basis of Zernike polynomials[4.27]. The Zernike polynomials $Z_{\tilde{n},m}(r,\theta)$ are a well known set of polynomials defined by

$$Z_{\tilde{n},\tilde{m}}(r,\theta) = \left\{ \begin{array}{ll} U_{\tilde{n},\tilde{m}}(r)\cos(\tilde{m}\theta), & \text{for} Z_{\tilde{n},\tilde{m}}(r,\theta) \\ U_{\tilde{n},\tilde{m}}(r)\sin(\tilde{m}\theta), & \text{for} Z_{\tilde{n},-\tilde{m}}(r,\theta) \end{array} \right\}, \tag{4.45}$$

where $Z_{\tilde{n},\tilde{m}}$ and $Z_{\tilde{n},-\tilde{m}}$ are called the even and odd polynomials respectively. Additionally, it is required $\tilde{m} \leq \tilde{n}$ and $\tilde{n} - |\tilde{m}| \in$ even number integers. The Zernike polynomials form an orthogonal basis set over the unit disk $r \in [0,1]$, $\theta \in [0, 2\pi]$. $U_{\tilde{n},\tilde{m}}(r)$ is called the radial function and is given by

$$U_{\tilde{n},\tilde{m}}(r) = \sum_{s=0}^{\frac{\tilde{n}-\tilde{m}}{2}} \frac{(-1)^s(\tilde{n}-s)!}{s!\left(\frac{\tilde{n}+\tilde{m}}{2}-s\right)!\left(\frac{\tilde{n}-\tilde{m}}{2}-s\right)!} r^{\tilde{n}-2s}. \tag{4.46}$$

For radially-symmetric problems Eq. 4.45 reduces to

$$Z_{\tilde{n},0}(r,\theta) = U_{\tilde{n},0}(r), \tag{4.47}$$

with

$$U_{\tilde{n},0}(r) = \sum_{s=0}^{\frac{\tilde{n}}{2}} \frac{(-1)^s(\tilde{n}-s)!}{s!\left(\frac{\tilde{n}}{2}-s\right)!\left(\frac{\tilde{n}}{2}-s\right)!} r^{\tilde{n}-2s}. \tag{4.48}$$

The Zernike polynomials are often used to characterise a phase $\phi(r,t)$ because the low order polynomials correspond to intuitive optical transformations, such as lenses, thus providing insight into the physical nature of $\phi(r,t)$. The orthogonality of the functions is used to decompose the phase given by Eq. 4.44 as

$$\phi(r,t) = \sum_{\tilde{n}}^{\infty} A_{\tilde{n},0} U_{\tilde{n},0}(r,\theta), \tag{4.49}$$

where

$$A_{\tilde{n},0} = 2(\tilde{n}+1) \int_0^1 kl \frac{\partial n'}{\partial u} u(Rr,t) r U_{\tilde{n},0}(r,\theta) dr. \tag{4.50}$$

With $A_{\tilde{n},0}$ being the coefficient of the $\tilde{n}^{\text{th}}$ Zernike polynomial. Substituting Eq. 4.38 into Eq. 4.50 gives

$$A_{\tilde{n},0} = 2(\tilde{n}+1) kl \frac{\partial n'}{\partial u} \sum_{n=1}^{\infty} \left\{ \left[\frac{-q_n \exp(-\Delta t) + q_n + \Delta p_n \exp(-\Delta t)}{\Delta} \right] \left[-\frac{\tilde{n}}{2} \frac{J_{\tilde{n}+1}(\aleph_n)}{\aleph_n} \right] \right\}. \tag{4.51}$$

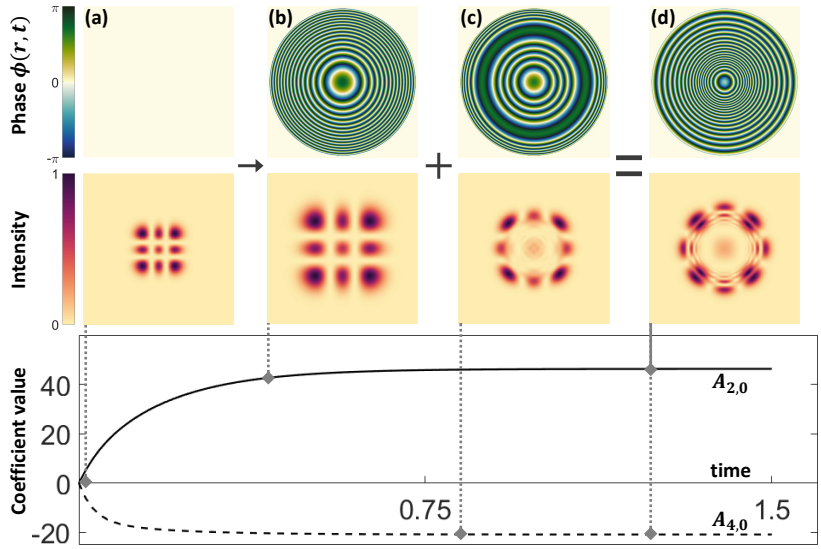


Fig. 4.3 The values of the $A_{\tilde{2},0}$ and $A_{\tilde{4},0}$ Zernike coefficients over time. The insets show the intensity (at the focal plane of a lens) and the aberrating phase $\phi(r,t)$ for: (a) The unaberrated HG mode; (b) The $A_{\tilde{2},0}$ aberration on the HG mode; (c) The $A_{\tilde{4},0}$ aberration on the HG mode, and (d) The cumulative effect of all $A_{\tilde{n},0}$ coefficients.

The effective focal length of the system described by Eq. 4.51 can be extracted using the $A_{\tilde{2},0}$ coefficient as

$$\frac{1}{\tilde{f}} = -\frac{2\lambda A_{\tilde{2},0}}{\pi R^2}. \tag{4.52}$$

Here R is the radius over which the polynomials are operating. Since Eq. 4.52 is derived from a complete expression for the phase $\phi(r,t)$ it provides a flexible approach to characterising the focal length. Consider a Tm:YLF rod heated by a centrally-positioned heat source of uniform-intensity. Figure 4.3 plots the values for the dominant $A_{\tilde{2},0}$ and $A_{\tilde{4},0}$ coefficients over time. The insets show the effect of each aberration individually as well as their combined effect on an HG beam of index $m = n = 2$ at the focal plane of a lens. Figure 4.3 reveals two important aspects of thermal aberrations. First, as the rod approaches a steady state temperature profile, the coefficient values become constant. Second and crucially, higher-order aberrations which may have small coefficients can nevertheless have a significant impact on beam quality, especially for non-radially-symmetric modes. By maintaining generality in the description of the temperature profile $u(r,t)$ in a medium and coupling this to a phase $\phi(r,t)$ expressed in the basis of Radial Zernike polynomials, a physically interpretable description of thermal aberrations can be realised for many media and modes, under a range of heating conditions.

4.1.3 Stress resulting from a central heat source

Consider a radially-symmetric optic of radius R through which a radially-symmetric high-intensity beam is passing. Assume that the length of the element is significantly greater than its radius, so that the axial stress may be neglected [4.28;4.29]. The radial σ_r and tangential σ_θ stresses can be formulated as

$$\begin{aligned}
\sigma_r &= \frac{\check{\gamma}Y}{1-\check{\nu}}\Big[\frac{1}{R^2}\int_0^R u(r,t)r\,dr - \frac{1}{r^2}\int_0^r u(\acute{r},t)\acute{r}\,d\acute{r}\Big], \\
\sigma_\theta &= \frac{\check{\gamma}Y}{1-\check{\nu}}\Big[\frac{1}{R^2}\int_0^R u(r,t)r\,dr + \frac{1}{r^2}\int_0^r u(\acute{r},t)\acute{r}\,d\acute{r} - u(r,t)\Big].
\end{aligned} \tag{4.53}$$

Here $\acute{r}$ is dummy variable for the radial position, $\check{\gamma}$ is the linear expansion coefficient, Y is Young's modulus and $\check{\nu}$ is Poisson's ratio. In the case of thin disks instead of rods, the formulation remains valid, with a change in prefactor $\frac{\check{\gamma}Y}{1-\check{\nu}} \rightarrow \check{\gamma}Y$. These equations predict

the fracture of an optical element when formulated as the stress intensity[4.26]

$$\sigma(r,t) = |\sigma_\theta - \sigma_r|. \tag{4.54}$$

Substituting Eq. 4.38 into Eq. 4.53 gives

$$\int_0^R u(r) r dr = \int_0^R \sum_{n=1}^{\infty} \left\{ \frac{[-\exp(-\Delta t)+1] q_n}{\Delta} J_0(\mu_n r) + \exp(-\Delta t) p_n J_0(\mu_n r) \right\} r dr. \tag{4.55}$$

Assuming the sum and the integral are interchangeable

$$\int_0^R u(r) r dr = \sum_{n=1}^{\infty} \left\{ \frac{[-\exp(-\Delta t)+1] q_n}{\Delta} \int_0^R J_0(\mu_n r) r dr + \exp(-\Delta t) p_n \int_0^R J_0(\mu_n r) \right\} r dr. \tag{4.56}$$

Using the integral property of Bessel functions,

$$\int_0^a x J_0(x) dx = a J_1(a). \tag{4.57}$$

Using variable substitution, Let

$$\begin{aligned} \mu_n r &= x, \\ dr &= \frac{dx}{\mu_n}. \end{aligned} \tag{4.58}$$

For

$$\begin{aligned} r &= R, \\ x &= \mu_n R, \\ &= \aleph_n, \\ \int_0^R u(r) r dr &= \sum_{n=1}^{\infty} \left\{ \frac{[-\exp(-\Delta t)+1] q_n}{\Delta} \int_0^R J_0(\mu_n r) r dr + \exp(-\Delta t) p_n \int_0^R J_0(\mu_n r) \right\} r dr, \end{aligned} \tag{4.59}$$

becomes

$$\int_0^R u(r) r dr = \sum_{n=1}^{\infty} \left\{ \frac{[-\exp(-\Delta t)+1] q_n}{\Delta} \int_0^{\aleph_n} J_0(x) \frac{x}{\mu_n} \frac{dx}{\mu_n} + \exp(-\Delta t) p_n \int_0^{\aleph_n} J_0(x) \frac{x}{\mu_n} \frac{dx}{\mu_n} \right\}. \tag{4.60}$$

Using equation 4.57

$$\int_0^R u(r)r\,dr = \sum_{n=1}^{\infty}\left\{\frac{[-\exp(-\Delta t)+1]q_n}{\Delta}\left[\frac{1}{\mu_n^2}\aleph_n J_1(\aleph_n)\right]+\exp(-\Delta t)p_n\left[\frac{1}{\mu_n^2}\aleph_n J_1(\aleph_n)\right]\right\},$$
$$\int_0^R u(r)r\,dr = \sum_{n=1}^{\infty}\left\{\left[\frac{R^2}{\aleph_n}J_1(\aleph_n)\right]\left[\frac{-\exp(-\Delta t)q_n+q_n}{\Delta}+\exp(-\Delta t)p_n\right]\right\}. \tag{4.61}$$

Performing an identical operation with a dummy variable $\acute{r}$, it is found

$$\int_0^r u(\acute{r})\acute{r}\,d\acute{r} = \sum_{n=1}^{\infty}\left\{\left[\frac{R}{\aleph_n}rJ_1(\mu_n r)\right]\left[\frac{-\exp(-\Delta t)q_n+q_n}{\Delta}+\exp(-\Delta t)p_n\right]\right\}. \tag{4.62}$$

For the temperature function $u(r,t)$ where the source $Q(r,t)=0$. Equations 4.61 and 4.62 reduce to

$$\int_0^R u(r)r\,dr = \sum_{n=1}^{\infty}\left[\frac{R^2}{\aleph_n}J_1(\aleph_n)\exp(-\Delta t)p_n\right], \tag{4.63}$$

and

$$\int_0^r u(\acute{r})\acute{r}\,d\acute{r} = \sum_{n=1}^{\infty}\left[\frac{R}{\aleph_n}rJ_1(\mu_n r)\exp(-\Delta t)p_n\right]. \tag{4.64}$$

Thus for $Q\neq 0$ the stress is

$$\sigma(t) = \left|\frac{\check{\gamma}Y}{1-\check{\nu}}\left\{\frac{2}{r}\sum_{n=1}^{\infty}\left[\frac{-q_n\exp(-\Delta t)+q_n+\Delta p_n(n)\exp(-\Delta t)}{\Delta}\right]\frac{R}{\aleph_n}J_1(\mu_n r)-u(r)\right\}\right|. \tag{4.65}$$

For $Q=0$

$$\sigma(t) = \left|\frac{\check{\gamma}Y}{1-\check{\nu}}\left\{\frac{2}{r}\sum_{n=1}^{\infty}\left[p_n(n)\exp(-\Delta t)\right]\frac{R}{\aleph_n}J_1(\mu_n r)-u(r)\right\}\right|. \tag{4.66}$$

As with the description of the thermal phase aberrations (Sec. 4.1.2), by making use of the general temperature characterisation $u(r,t)$ it is possible to formulate a description of the stress which can be realised for many media under diverse heating conditions.

4.2 An annular heat source

This section explores how an annularly-structured heat source is capable of reducing both the mechanical stress and thermal aberrations induced in a heated optic. Recall the source term $q_n(t)$ from Eq. 4.39. By structuring the radial component of the heat source $Q(r,t)$ to have its maximum value at the point where the Bessel function $J_0(\mu_n r)$ has its minimum value, the total value of the integral can be minimised. Physically, this means that by replacing a central heat source with an annular heat source, the intensity $I(r,t)$ can be maintained whilst reducing the magnitude of the $q_n(r,t)$ factor. Hence, the effects which are proportional to this factor are diminished, corresponding to a reduction in the global thermal gradient across the optic, reducing both the mechanical stress and thermal aberrations. An annular heat source $Q_{\text{an}}(r,t)$ with outer boundary ω is defined as

$$Q_{\text{an}}(r,t) = \begin{cases} \frac{\xi\nu}{\rho c_p}\frac{\hat{P}}{\pi\omega_0^2}, & \text{for } \sqrt{\omega^2-\omega_0^2} \le r \le \omega \\ 0, & \text{otherwise} \end{cases}. \tag{4.67}$$

This definition ensures

$$\int_0^{2\pi}\int_0^R Q_{\text{c}}(r,t)\,dr\,d\theta = \int_0^{2\pi}\int_0^R Q(r,t)_{\text{an}}\,dr\,d\theta. \tag{4.68}$$

By satisfying Eq. 4.68 the annular heat source delivers the same total energy as the central heat source whilst also maintaining the same intensity. For Eq. 4.67, $q_n(t)$ is

$$q_n(t) = \frac{2}{[RJ_1(\aleph_n)]^2}\frac{\xi\nu}{\rho c_p}\frac{\hat{P}}{\pi\omega_0^2}\left[\frac{-\sqrt{\omega^2-\omega_0^2}J_1\left(\mu_n\sqrt{\omega^2-\omega_0^2}\right)+\omega J_1\left(\omega\mu_n\right)}{\mu_n}\right]. \tag{4.69}$$

4.2.1 Annular sources and stress

Consider the role of q_n (Eq. 4.39) in the stress $\sigma(r,t)$ described in Eq. 4.65. This expression is the product of a magnitude in the source and initial terms q_n, p_n, and a spatial geometry in the Bessel function J_1. Consequently, minimising the q_n contribution by changing to an annular source reduces the stress on the optical element. Figure 4.4 compares the stress experienced by a rod when heated with central and annular sources. As the rod heats the stress increases. If heated continuously by a central source $Q_{\text{c}}(r,t)$ of uniform-intensity the stress quickly exceeds the 40 MPa fracture limit, damaging the rod. This would necessitate the use of either a quasi-continuous or lower energy heat source. By

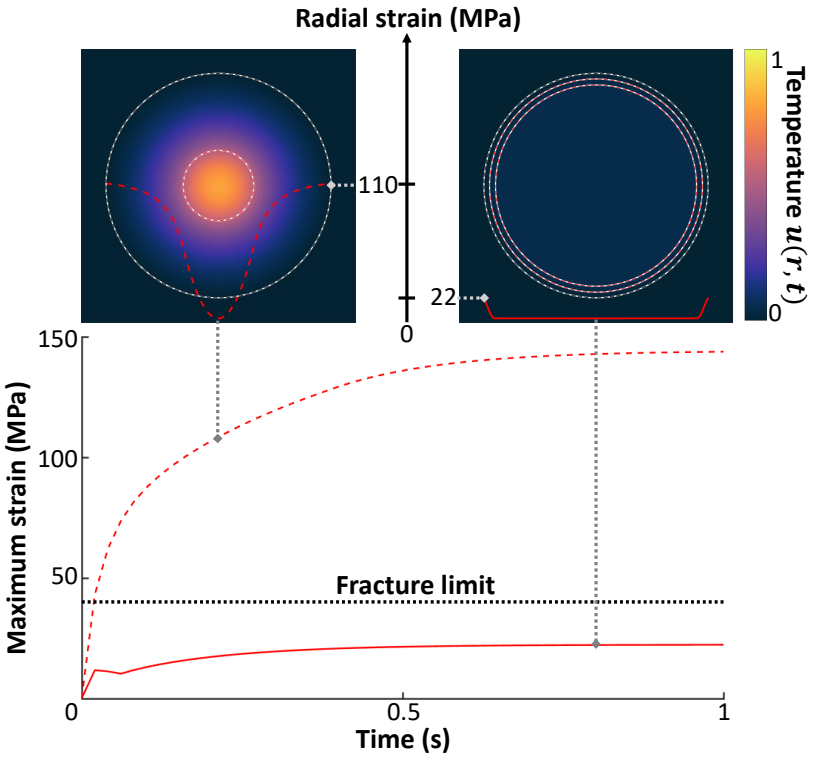


Fig. 4.4 The stress experienced by a rod when heated by a central (red dashed) and annular (solid red) source. The insets show: the temperature profile of the rod at 0.25 s and 0.75 s; the concentric circles indicate the boundary of the rod and the location of the heat source; and the line plots show the radial stress profile.

comparison, an annular heat source $Q_{\text{an}}(r,t)$ of the same intensity having $\omega = 0.95 \times R$ is able to keep the stress below the fracture limit, even with continuous heating. This is a result which could not be achieved using corrective or adaptive optical systems, which only operate on phase.

4.2.2 The local action

As with the stress formulation (Sec. 4.1.3), the thermal aberrations described by Eq. 4.51 take the form of a factor $q_n(t)$ and a Bessel function. Hence, by reducing $q_n(t)$, the magnitude of the temperature profile and, by extension, the coefficients of the Zernike polynomials and the associated thermal aberrations can be reduced. This is the case depicted in Fig. 4.5 for a central source of uniform-intensity $Q_{\text{c}}(r,t)$, an annular source $Q_{\text{an}}(r,t)$ with $\omega = 0.5 \times R$ and an annular source $Q_{\text{an}}(r,t)$ with $\omega = 0.8 \times R$. As the heat source changes from the central case examined in section 4.1 to an annular case, the temperature profile across the surface not only reduces in overall magnitude, but also

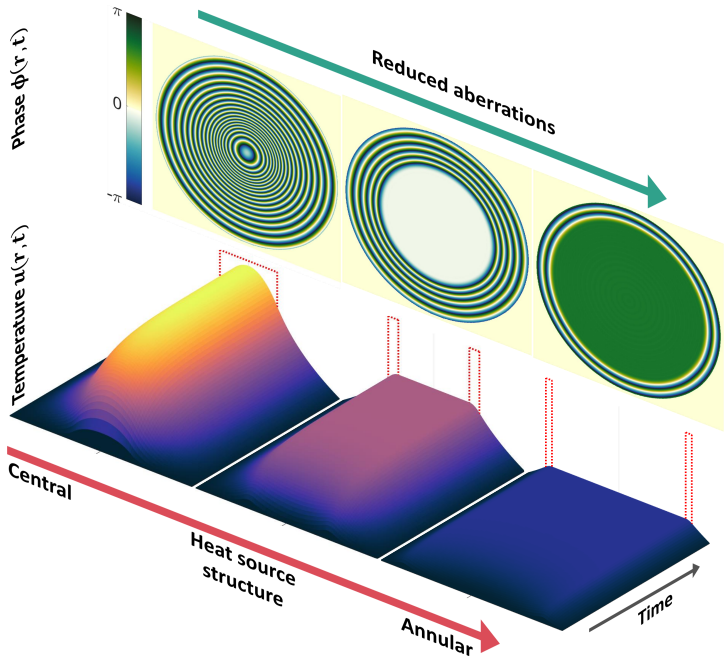


Fig. 4.5 The temperature $u(r,t)$ and phase $\phi(r,t)$ profiles for a rod in an annular heating regime. As the source approaches an annular ring at the radius of the rod, an area of constant phase develops in the centre of the rod, reducing aberrations.

in global gradient, thus reducing the total aberration. This can be seen clearly in the emergence of a circular region of constant phase addition bounded by the annular heat

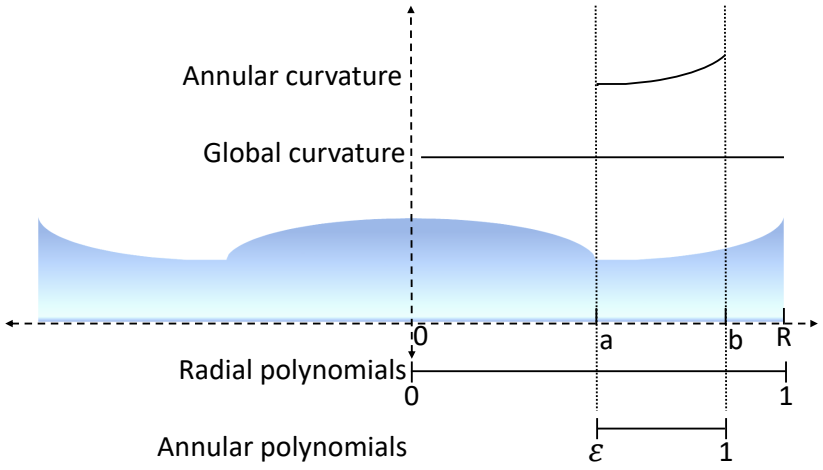


Fig. 4.6 A convergent lens embedded in the centre of a divergent lens. The global curvature over the radius for which the Radial Zernike polynomials are defined is flat. The annular region $[\epsilon, 1]$ over which the Annular Zernike polynomials are defined retains its local curvature.

source. At this point, a critical distinction must be made between the global phase of the optic and the phase which exists only within the local annular region illuminated by the probe beam. A simple case of this distinction is shown in Fig. 4.6 in which a convergent lens is embedded in the centre of a divergent lens. The global radius of curvature for such a surface could be flat, $A_{2,0} = 0$, meaning the $A_{2,0}$ coefficient would no longer intuitively capture the physical behaviour of the optic. A solution can be found in the Annular Zernike polynomials and their coefficients $A_{\hat{n},0}$. The Annular polynomials are closely related to the Radial polynomials and are defined over the unit annulus as

$$\phi(r,t) = \sum_{\hat{n}}^{\infty} A_{\hat{n},0} U_{\hat{n},0}(r,\theta), \tag{4.70}$$

where

$$A_{\hat{n},0} = 2(\hat{n}+1)\left(\frac{1}{1-\epsilon^2}\right)\int_{\epsilon}^{1} kl\frac{\partial n'}{\partial u}u(Rr,t)rU_{\hat{n},0}(r,\theta)dr, \tag{4.71}$$

with

$$U_{\hat{n},0}(r,\theta) = U_{\tilde{n},0}\left[\left(\sqrt{\frac{r^2-\epsilon^2}{1-\epsilon^2}}\right),\theta\right]. \tag{4.72}$$

Again, substitution of the temperature profile $u(r,t)$ (Eq. 4.38) gives

$$\begin{aligned} A_{\hat{n},0} = 2(\hat{n}+1)\left(\frac{1}{1-\epsilon^2}\right)kl\frac{\partial n'}{\partial u}\sum_{n=1}^{\infty}\left\{\left[\frac{-q_n\exp(-\Delta t)+q_n+\Delta p_n\exp(-\Delta t)}{\Delta}\right]\right. \\ \left.\left[\int_{\epsilon}^{1} J_0(\mu_n br)U_{\hat{n},0}(r,\theta)rdr\right]\right\}. \end{aligned} \tag{4.73}$$

ϵ is referred to as the occlusion ratio defined by

$$\epsilon = \frac{a}{b}. \tag{4.74}$$

Here a and b are the inner and outer boundaries of the annulus in a non-normalised coordinate system. In the limit $a \to 0$ the Annular polynomials reduce to the Radial polynomials over the unit disk $[0,b]$. The Annular polynomials allow for the physically significant description of the local action of an annular source.

Figure 4.7 displays the local action of an annular heat source as the heat source is moved towards the radius R. To visualise this effect, Laguerre-Gaussian beams which have been matched to the radial position of the heat source are used. The top row of the figure displays the intensities of the input beams. The middle row displays the aberrating phase derived from Eq. 4.73. The bottom row displays the aberrated input beams at the focal

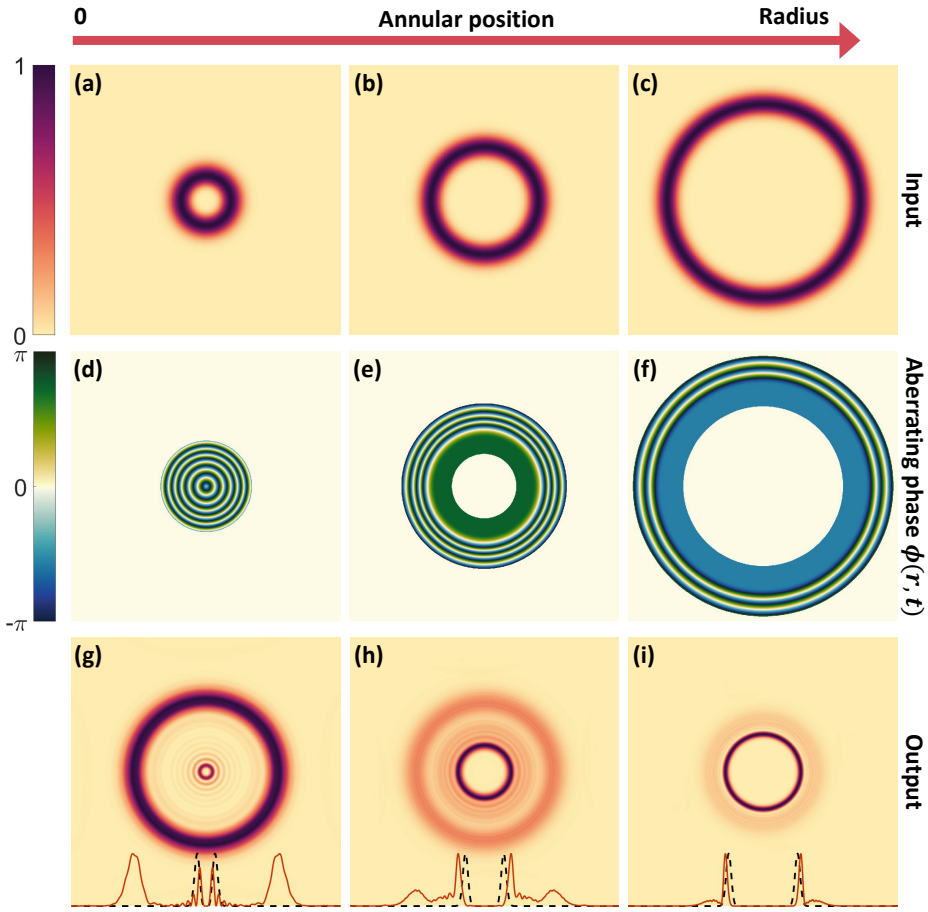


Fig. 4.7 (a),(b) and (c), input LG beams spatially matched to annular heat sources with an outer boundary at $\omega = 0.3\times$, $0.5\times$, and $0.83 \times R$ of a rod. (d),(e) and (f), the phase profiles associated with the heat sources as described by the Annular Zernike polynomials. (g),(h) and (i), the intensities of the aberatted input beams at the focal plane of a lens, the inset line plots show the unaberrated and aberrated profiles as black dashed and orange solid lines respectively. Note that the output beams have been independently normalised to aid in the visualisation.

plane of a lens. The figure is calculated using both the same rod and total incident energy as Sec. 4.1.2.

Figure 4.7 illustrates two key findings when considering annular sources. First, panels (b), (e) and (h) show that when using an annular source, careful consideration must be given as to whether the region of interest is within the zone of constant phase which forms when using the Radial polynomials (Fig. 4.5) or if it is contained within the annular source itself, in which case the beam may still be highly aberrated. Second, panels (f) and (i) show

that even when considering an annular region of interest, aberrations are reduced as the heat source approaches an annular ring at the radius. In Fig. 4.7 this is illustrated by the overlap between the profiles of the aberrated and unaberrated beams. When the annular region is near the centre, the input beam is significantly enlarged both in total diameter and waist, while also exhibiting concentric rings. As the annular region moves outwards, the concentric rings diminish and a bright correctly-sized ring emerges. This is because the Annular polynomials (Eq. 4.73) share the same magnitude and spatial structure as the Radial polynomials (Eq. 4.51). Thus, by reducing the contribution of the $q_n(t)$ terms with a structured heat source, the effect of the aberrations is reduced. As with the Radial polynomials description from Sec. 4.1.2 it is possible to extract an effective focal length from the phase characterisation. The effective focal length is related to the coefficient of the $A_{\hat{2},0}$ annular polynomial by

$$\frac{1}{\hat{f}} = -\frac{6\lambda A_{\hat{2},0}}{\pi b^2(\epsilon^2-1)^2}. \tag{4.75}$$

Hence use of the Annular Zernike polynomials always allows the phase $\phi(r,t)$ to be described in a physically intuitive manner for annular cases.

4.2.3 The global action

By combining the observations made so far, it is possible to examine cases in which the area of the optic under heating is not the same as the area through which the probe beam is propagating. Figure 4.8 shows the effect of passing both a super-position of HG and LG beams through a rod heated by an annular source. The annular source has an outer boundary at $\omega = 0.86 \times R$. The waists of the beams were chosen such that they fell within the area of constant phase created by the annular source. At the focal plane of a lens the beams are resized, but are otherwise without aberration. This result demonstrates that by changing to an annular heat source the aberrations induced in a medium can be effectively mitigated.

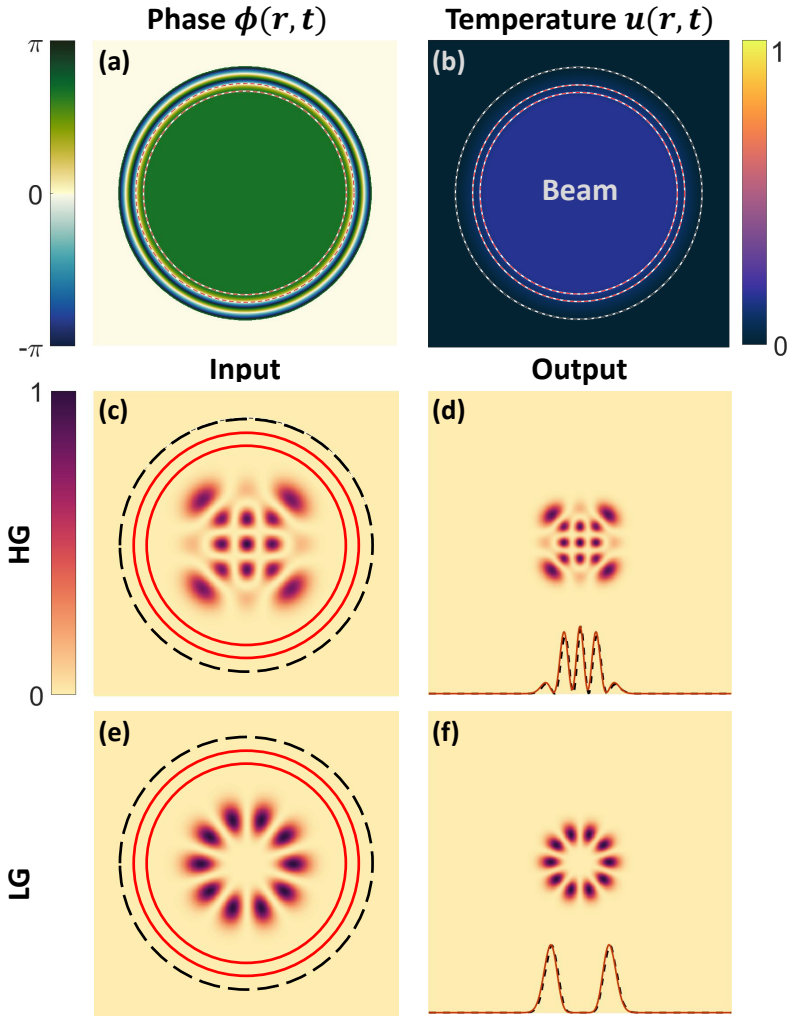


Fig. 4.8 (a) and (b), the aberrating phase $\phi(r,t)$ and corresponding temperature $u(r,t)$ for a heat source with $\omega = 0.86 \times R$. The outermost black dashed circle indicates the radius of the rod. The annular heat source is indicated by the two innermost red circles. (c) and (e), the super-positions of HG and LG beams respectively. (d) and (f) the intensities of the beams at the focal plane of a lens. The inset line plots show the unaberrated and aberrated profiles as black dashed and orange solid lines respectively.

4.3 Experimental setup

To verify the approach described mathematically above, the experimental setup depicted in Fig. 4.9 was constructed. A TI 3000 DMD was used to physically simulate a heated optical element. The system is analogous to an old film projector. By displaying an ordered series of holograms where each hologram captures the temperature profile of the optic, beams with a phase $\Omega(x,y)$ and amplitude profile $A(x,y)$ were created as though they had been produced by a high-energy source. A camera then measured these beams at the

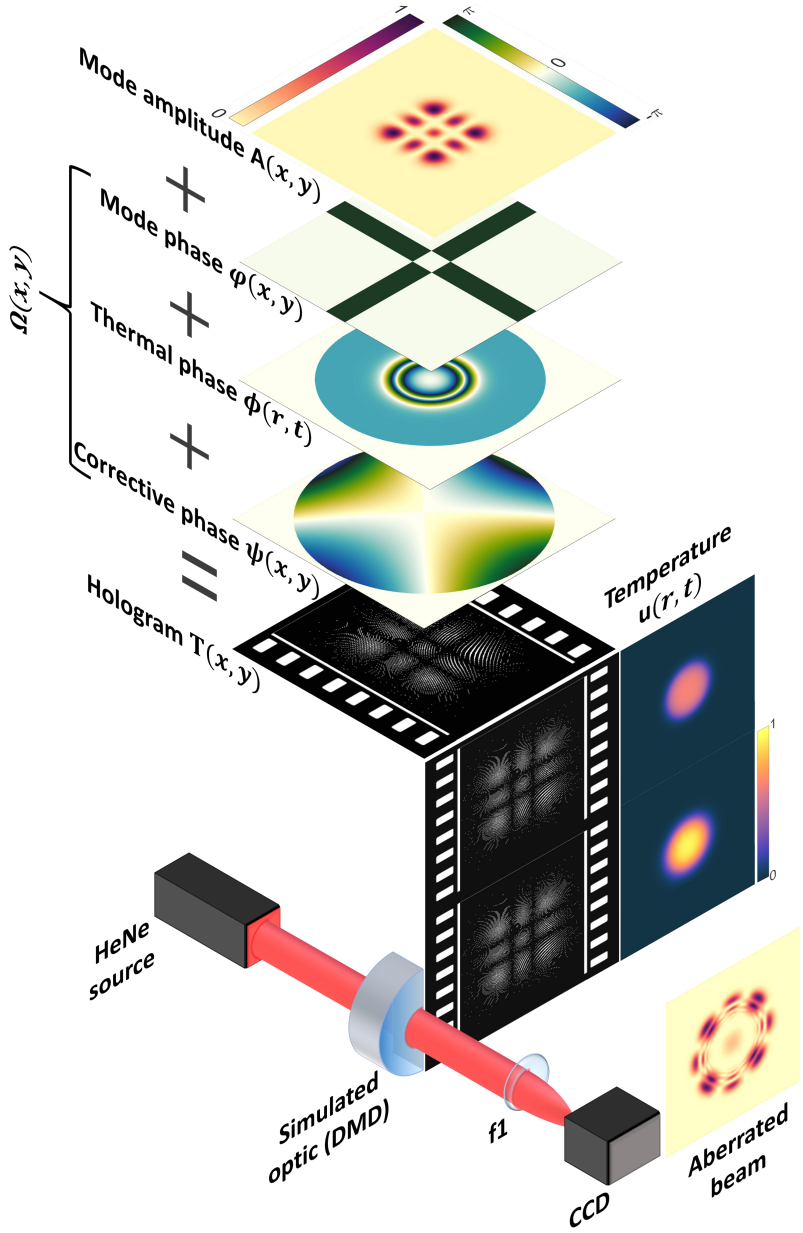


Fig. 4.9 The experimental setup shown conceptually. The DMD was used as though it was an old film projector, i.e. dynamically simulating the heated optic by displaying an ordered set of holograms corresponding to the temperature profile of the optic. Each hologram encodes an amplitude $A(x,y)$ and a phase, where the total phase $\Omega(x,y)$ is made up of three components: the phase inherent to the desired mode $\varphi(x,y)$; the phase of the thermal aberration $\phi(r,t)$, and the corrective phase accounting for the deformations to the DMD $\psi(x,y)$. A well expanded and collimated beam from a HeNe source was incident on the DMD. The beams created by the holograms were recorded at the focal plane of a lens by a camera.

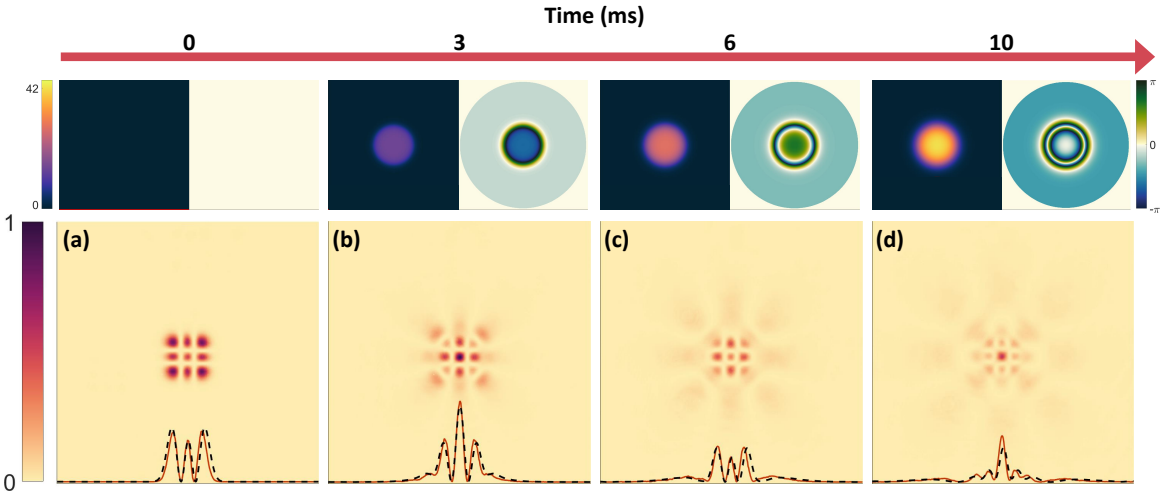


Fig. 4.10 The self action of a central heat source on an HG beam over time. The upper insets show the temperature $u(r,t)$ of the modelled rod and the aberrating phase $\phi(r,t)$ of the hologram. The main panels show the measured beam at four points in time, (a) at $t = 0$, (b) at $t = 3$, (c) at $t = 6$, and (d) at $t = 10$ ms respectively. The line plots show the profiles of the simulated beam and the measured beams as black dashed and orange solid lines respectively.

focal plane of a lens $f1$, where the phase would effect the intensity. Thus by changing the holograms, a setup of this type can be easily configured to produce beams which provided a physical simulacrum to a system experiencing thermal aberrations. Each hologram encoded an amplitude $A(x,y)$ and a phase, where the total phase $\Omega(x,y)$ was made up of three components: the phase inherent to the desired mode $\varphi(x,y)$; the phase of the thermal aberration $\phi(r,t)$; and the corrective phase accounting for the deformations to the DMD $\psi(x,y)$. The holograms were created using the approach covered in Sec. 1.1.2, while the DMD was implemented according to the guidelines presented in Chp. 2.

4.4 Results for a central source

Here the effect of heating a Tm:YLF rod with a centrally-positioned heat source $Q_c(r,t)$ of uniform-intensity is modelled. An HG beam of index $m = n = 2$ and waist 3.5×10^{-4} m having the appropriate thermally-induced aberration $\phi(r,t)$ was created and measured by the experimental setup in Fig. 4.9. The thermal aberrations were calculated using the first 100 even Radial Zernike polynomials. For this case, the degradation of the beam over time was monitored. The rod was heated for 10 ms to mimic a physically meaningful system in which the thermal load would not result in damage to the rod [4.26]. Figure 4.10 shows the measured beam and corresponding phase and temperature profiles at four selected

points in time. At $t = 0$ the modelled rod has a uniform initial temperature distribution and so applies no phase to the beam. Consequently, the measured beam is unaberrated. As the rod heats it takes on a non-uniform temperature distribution, introducing thermal aberrations dominated by a defocus and a primary spherical aberration. These aberrations enlarge the total area of the beam and completely degrade its structure. The results presented in Fig. 4.10 were selected from a continuous set of measurements spanning the 10 ms heating time.

4.5 Results for an annular source

4.5.1 The local action

The local action of an annular heat source was observed using an LG beam spatially matched to a source which had the same parameters as those given in Sec. 4.4. The LG beam had a waist of 2.5×10^{-4} m and was matched to the annular source by adjusting its azimuthal index ℓ. The aberrating phase $\phi(r, t)$ imparted to the beam was calculated using the first 100 even Annular Zernike polynomials. Figure 4.11 shows the measured beam and corresponding aberrating phase $\phi(r, t)$ and temperature $u(r, t)$ distributions for an annular source with its outer edge at four equally-spaced positions. The measurement at $\omega = 0.31 \times R$ corresponds to the minimum size of an annular source due to its finite width as given in Table. 4.1. Here, the expansion of the heat source towards the radius was limited by the finite waist of the corresponding LG beam. Beyond $\omega = 0.81 \times R$, the outer edges of the LG beam were no longer contained within the radius of the rod. The temperature insets in Fig. 4.11 show that as the annular heat source moved towards the radius of the modelled rod, an area of uniform temperature distribution formed within the area encompassed by the annulus. However, aberration is still present within the heated annular region. When the heat source was near the centre of the rod, a defocus and a primary spherical aberration were dominant. These resulted in both an enlargement of the beam as a whole, and a broadening of its ring structure. This is seen by the large size discrepancy between the profile of the measured beam and the profile of an unaberrated beam shown in panel (a) of Fig. 4.11. As the annular source moved outwards, more complex aberrations created concentric rings of decreasing intensity around a central high-intensity ring. Most importantly, with the annular ring near the radius of the modelled rod, the aberrations were reduced as a consequence of the reduced temperature gradient in the rod. The result was a reduction in the prevalence of the concentric rings, allowing the inner-most ring to approach the correct size and intensity for an unaberrated beam. The reduction in

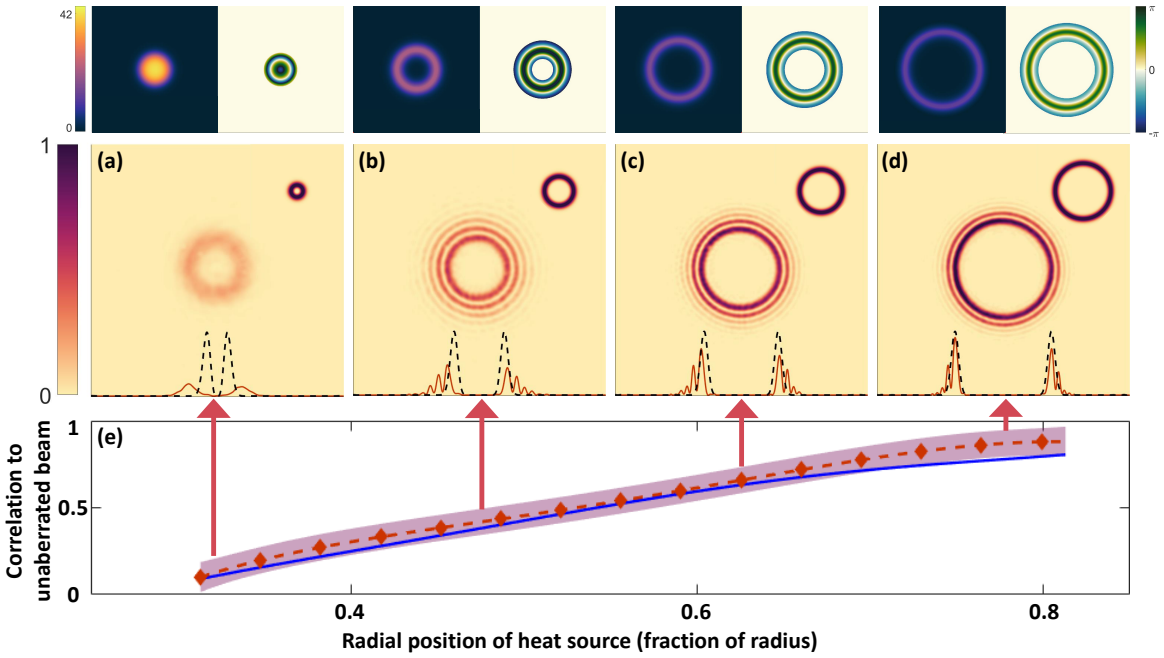


Fig. 4.11 The self action of an annular heat source on an LG beam. The upper insets show the temperature of the rod $u(r,t)$ and aberrating phase $\phi(r,t)$ of the hologram. Panels (a) through (d) show the measured beams for an annular source with its outer edge at $\omega = 0.31\times$, $\omega = 0.47\times$, $\omega = 0.64\times$ and $\omega = 0.81 \times R$ respectively. The insets in these panels show the input beams. The line plots show the profiles of an unaberrated beam and the measured beams as black dashed and orange solid lines respectively. Panel (e) shows the correlation between the measured beam and the simulation of an unaberrated beam as a function of heat source position. The red dashed line indicates the line of best fit for the experimental data with the shaded region indicating the 95% confidence interval. The blue solid line is the theoretical prediction.

the strength of the aberrations was quantified by calculating the correlation between the measured beam and an unaberrated beam. Figure 4.11 panel (e) shows this quantity as a function of the position of the outer edge of the heat source. As the heat source moved outwards, the correlation increased from less than 20% to in excess of 80%. This result confirms that even when considering a beam which is spatially coincident with a heated annular region, the thermally-induced aberrations are reduced as the heated region approaches the radius.

4.5.2 The global action

To test the global action, beams were passed through the centre of the rod while an annular heat source moved outwards from the centre to the radius. To quantify the reduction in

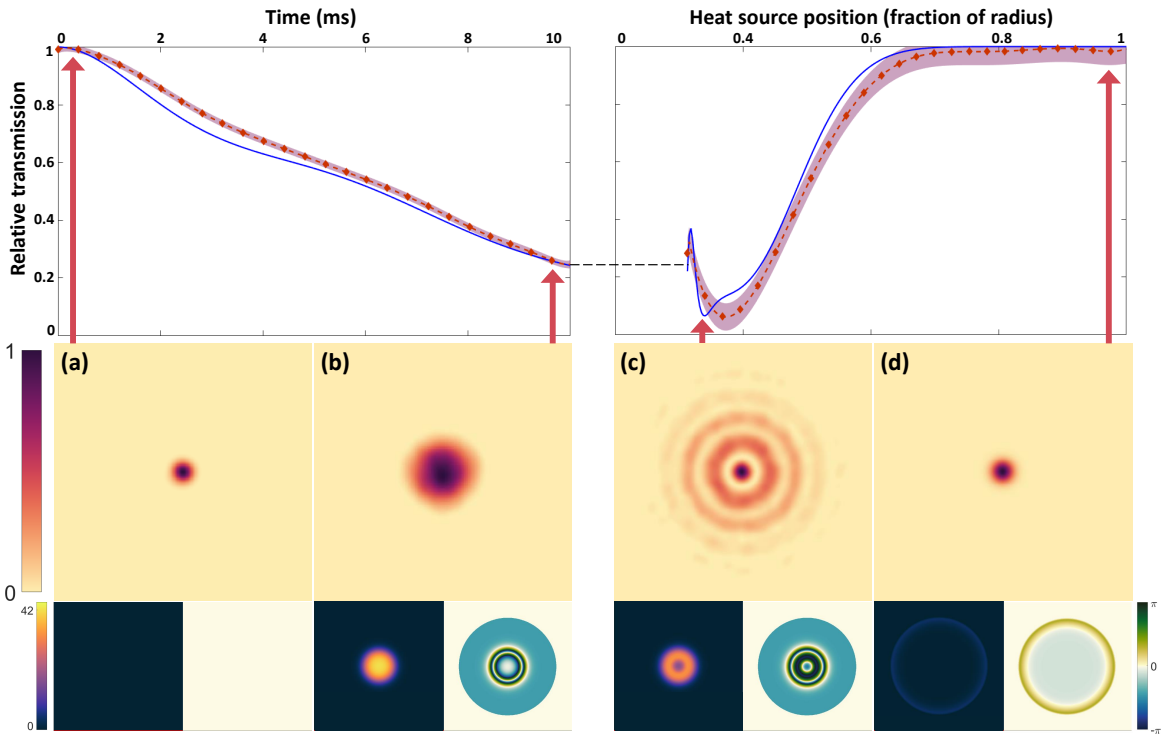


Fig. 4.12 The intensity through an aperture for a Gaussian beam passing through the modelled rod: over time on the left, and as the annular source moves outward on the right. The red dashed line indicates the line of best fit for the experimental data with the shaded region indicating the 95% confidence interval. The blue solid line is the theoretical prediction. The panels (a) through (d) show the measured beams at the positions indicated by the arrows with the corresponding temperature $u(r,t)$ and aberrating phase $\phi(r,t)$ profiles shown below. Note that each measured beam has been independently normalised to aid in visualisation.

thermal aberrations for a realistic physical system, the loss in intensity of an aberrated Gaussian beam of waist 3.5×10^{-4} m passing through an aperture at the focal plane was measured. The aperture was sized at $1/e^2$ the width of an unaberrated beam. The total intensity transmitted through this aperture was then measured, effectively performing a D86 measurement [4.30;4.31;4.32]. Two measurements were taken. First, to provide a baseline, the same parameters as in Sec. 4.4 were used. As heating occurred, the Gaussian beam passing through the centre of the modelled rod became aberrated and was partially occluded by the aperture, with the corresponding loss in intensity recorded. Second, the same system was fixed at a time of $t = 10$ ms and the increase in intensity measured as an annular heat source moved outwards towards the radius. The left-hand side of Fig. 4.12 shows that under realistic circumstances, a Gaussian beam passing through a centrally heated Tm:YLF rod may experience as much as a 75% reduction in aperture transmission

at the focal plane. This is due to the thermally-induced defocus aberration, the effect of which is clear when comparing the sizes of the beams in panels (a) and (b). This degradation is significant, especially in industrial and defence applications, as explained in the introduction. The right-hand side of Fig 4.12 shows how as the annular source moved outwards, the aperture transmission increased. The plot depicts the increase in transmission against the position of the outer edge of the heat source as a fraction of the radius. An annular source initially resulted in a reduction in the transmission. This occurred when the annular source was sufficiently near the centre of the rod for the Gaussian beam to overlap with it, resulting in the formation of concentric rings which can be seen in panel (c). These concentric rings moved energy radially outwards resulting in an overall decrease in transmitted intensity. As the annular heat source was moved further outwards, the Gaussian beam was contained entirely within the region of constant phase. Once within this region the beam was unaberrated, thus the relative transmission increased to a value of ≈ 1. This region of constant phase bounded by

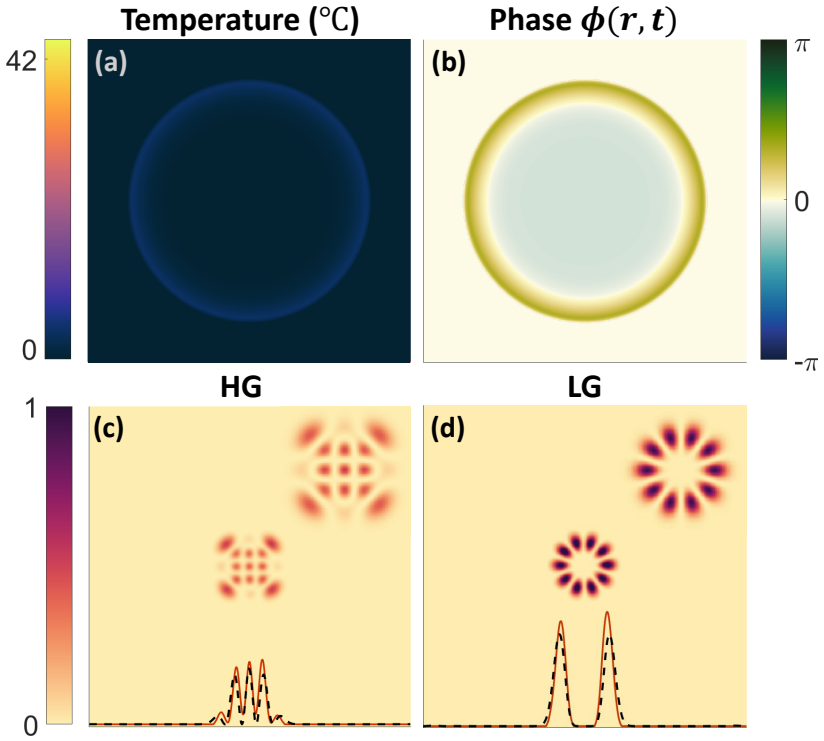


Fig. 4.13 The global action of an annular source on superpositions of HG (c) and LG (d) beams. (a) the temperature $u(r,t)$ of the rod for an annular heat source at its radius. (b) the aberrating phase $\phi(r,t)$ of the hologram. The insets in (c) and (d) show the input beams. The line plots show the profiles of unaberrated beams and the measured beams as black dashed and orange solid lines respectively.

the heat source reduces aberrations for all beam types, not only Gaussians. Figure 4.13 shows the temperature $u(r,t)$ of the rod for an annular source at the radius with the corresponding aberrating phase $\phi(r,t)$ calculated by the Radial Zernike polynomials. Additionally, the figure shows the effect of this phase on superpositions of HG and LG modes. The high degree of overlap between the profiles of the measured results and the theoretical prediction for an unaberrated beam indicates that even modes which are highly structured can pass undisturbed through the centre of an annular heat source.

4.6 Discussion

When interpreting the thermally-induced phase $\phi(r,t)$ of a system, characterisations using easily conceptualised quantities, e.g. effective focal length, are more useful than purely mathematical descriptions, even when both are technically valid. For instance, in the case of an annular heat source, the phase $\phi(r,t)$ is defined everywhere on the surface of an optic as a consequence of the temperature $u(r,t)$ being defined everywhere. Hence, the Radial polynomials are always a valid mathematical description of the phase. However, it is the aberration experienced by a beam, not the global phase distribution, which is of interest. In other words, while the Radial polynomials are mathematically valid, the Annular polynomials provide a more physical description. Further, using the Zernike basis allows the reduction in the strength of the aberrations as the source changes to an annulus to be quantified. The variance of the aberrating phase ζ captures the total magnitude of the aberrations. The variance ζ for the Radial polynomials is calculated,

$$\tilde{\zeta} = \sum_{\tilde{n}}^{\infty} \frac{\left(A_{\tilde{n},0}\right)^2}{\tilde{n}+1}. \tag{4.76}$$

For the Annular polynomials the variance is

$$\hat{\zeta} = \sum_{\hat{n}}^{\infty} \left[\frac{(1-\epsilon^2)\left(A_{\hat{n},0}\right)^2}{\hat{n}+1} \right] - (1-\epsilon^2)^2. \tag{4.77}$$

Figure 4.14(a) and 4.14(d) plot the reduction in the total magnitude of the aberration as the outer boundary of the heat source approaches the radius of the rod for the Radial and Annular polynomials respectively. The panels 4.14(b) and (c) show the phase as described by the Radial polynomials corresponding to the points on the graph indicated by the arrows. The panels 4.14(e) and (f) show the same for the Annular polynomials. As the heat source moves outwards the total aberration strength decays asymptotically in both

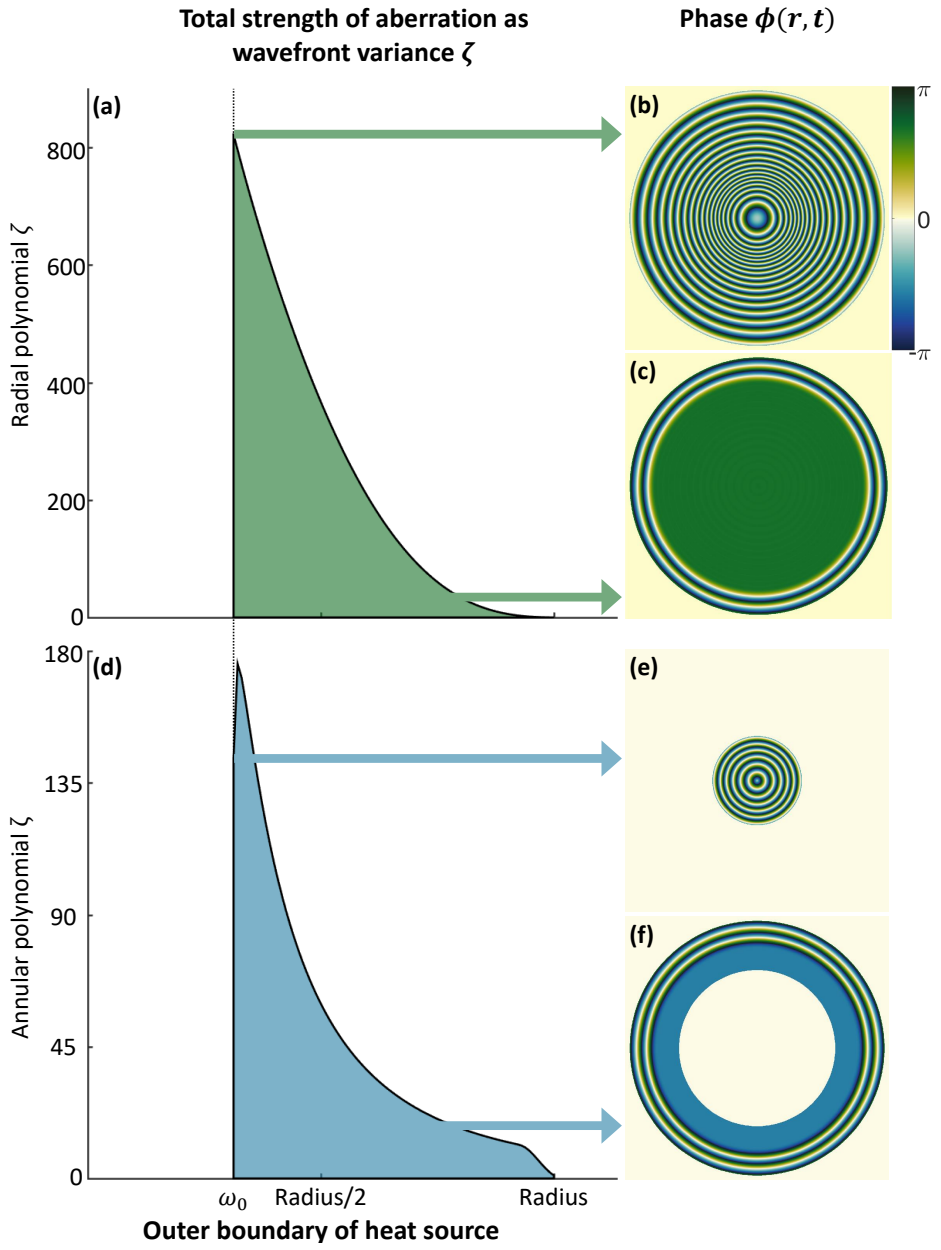


Fig. 4.14 The relationship between total aberration strength calculated as wavefront variance ζ and the outer boundary of the heat source for the Radial (a) and Annular (d) Zernike polynomials respectively. The phase panels (b), (c), (e) and (f) show the phase aberration in each basis at the points indicated by the arrows. ω_0 represents the minimum outer boundary for a heat source of width ω_0.

bases. The specific values of the radial and annular variances cannot be directly compared, since the polynomials to which they are attached differ. This is clearly illustrated in the phase panels of Fig. 4.14 where the Radial polynomials are shown to always be defined

over the entire surface, while the Annular polynomials are confined to a ring. Hence a smaller magnitude for an annular coefficient in comparison to a corresponding radial one for the same source does not automatically correspond to a less aberrated beam. Figure 4.14 illustrates that, it is not the description of the phase $\phi(r,t)$ in an annular basis which reduces aberrations, but the minimisation of the source term q_n by moving the heat source radially outwards.

4.6.1 Effects on brightness

The analysis presented thus far has worked with an abstract optical heat source $Q(r,t)$. In the context of end-pumped solid-state lasers, the optical heat source takes the form of the pump beam for the laser. Section. 4.2.1 makes clear that by transitioning to an annular pump, input energies could be increased thanks to the reduction in the thermally-induced stress. Further, while it has been observed that annular pumping reduces thermal stress[4.33] as well as the thermal aberrations in the centre of an optic[4.34;4.35] it is not widely understood that the aberrations within the annular region are also reduced. The characteristics of annular pumps suggest that lasers which natively produce annular beams[4.36;4.37] have the possibility to operate at very high pump energies whilst not experiencing significant aberrations. Additionally, because the aberrating phase which is present within the annular region can be calculated explicitly using Eq. 4.73, all of the existing techniques using phase-only adaptive or corrective optics could be applied, yielding practically aberration-free high-energy beams. However, these beams are not in and of themselves sufficient to improve laser brightness because of the reduction in M^2 associated with using annular beams. It is here where the approach presented in Chp. 3 can be applied. The ability to losslessly transform an annular beam into a Gaussian beam means that the initial power density P of the beam can be maximised using an annular pump beam and lasing mode before it is transformed to a Gaussian, reducing its M^2. For a lasing system which employs both a structured pump and lossless reshaping the brightness enhancement η can be formulated as

$$\eta = (M_0^2)^2 \frac{P_1}{P_0}. \tag{4.78}$$

Here M_0^2 is the M^2 of the annular beam, P_1 and P_0 are the power densities of the system for an annular and central pump respectively. If both systems produce a Gaussian beam

of the same area and solid angle divergence then Eq. 4.78 reduces to

$$\eta = (M_0^2)^2 \frac{\hat{P}_1}{\hat{P}_0}, \tag{4.79}$$

where $\hat{P}_1$ and $\hat{P}_0$ are the maximum pump powers which can be used without damaging the gain medium. Consider a Tm:YLF rod, for a central pump and 10 ms of heating the maximum energy which can be added is $\hat{P}_0 = 290$ W. For an annular pump with $\omega = 0.83 \times R$ as used in Sec. 4.2.2 this number is $\hat{P}_1 = 550$ W. Further, to match the annular pump with $\omega = 0.83 \times R$ used in Sec. 4.2.2 an LG beam with $\ell = 73$ was used. The M^2 of this LG beam can be derived from the equation given in Table. 1.1. Hence, the total brightness enhancement for a system using both a structured pump and lossless reshaping could be

$$\begin{aligned} \eta &= [2(0) + |73| + 1]^2 \frac{550}{290}, \\ \eta &> 10^4. \end{aligned} \tag{4.80}$$

This represents a four order of magnitude increase in brightness and validates the principle aim of this work. That is to say, by employing the tools of structured light, the brightness of laser systems can be increased in a meaningful way.

4.7 Summary of chapter 4

This chapter characterised the temperature profile for a radially-symmetric optic using the Eigen-function expansion. From this characterisation expressions for the thermally-induced stress and phase aberrations were formulated. The generality of these expressions was exploited to demonstrate how a heat source having an annular structure reduces both thermal aberrations and thermal stress in all cases. A thorough analysis of the phase experienced by Hermite-Gaussian and Laguerre-Gaussian probe beams using both the Radial and Annular Zernike polynomial bases was given. An experimental physical simulator of these phenomena, built around a DMD was demonstrated. This system allowed for the experimental exploration of the theory, in this case for a Tm:YLF rod, though the approach and solutions are flexible enough to apply to many other cases. The fidelity of the probe beams was measured. In the case of an LG beam, the use of an annular source improved the beam fidelity from less than 20% to in excess of 80%, whilst in the case of a focused Gaussian beam or the superpositions of HG and LG beams, the thermal phase aberrations were removed completely. These results corroborate the findings of the theory that is, changing to an annular heat source generally reduces thermal phase

aberrations and stress for radially-symmetric optical systems. Finally, a discussion on the physical interpretation of the theory in terms of physical quantities was provided. This discussion also explored the effect of a structured heat source on brightness, where it was found that if the heat source is a pump beam and the findings of Chp. 3 are implemented, the brightness can be enhanced by four orders of magnitude. This result confirms the principle objective of the dissertation as a whole.

References

4.1 D. A. Rockwell, "A review of phase-conjugate solid-state lasers," *IEEE Journal of Quantum Electronics*, vol. 24, no. 6, pp. 1124–1140, 1988.

4.2 P. Becker, L. Bohatỳ, H. Rhee, H. Eichler, J. Hanuza, and A. Kaminskii, "Observation of many-phonon stimulated Raman scattering and related cascaded nonlinear-laser effects in monoclinic $LaBO_2MoO_4$ single crystals," *Laser Physics Letters*, vol. 5, no. 2, p. 114, 2007.

4.3 T. Y. Fan, D. J. Ripin, R. L. Aggarwal, J. R. Ochoa, B. Chann, M. Tilleman, and J. Spitzberg, "Cryogenic Yb^{3+}-doped solid-state lasers," *IEEE Journal of Selected Topics in Quantum Electronics*, vol. 13, no. 3, pp. 448–459, 2007.

4.4 M. Eichhorn, "Quasi-three-level solid-state lasers in the near and mid infrared based on trivalent rare earth ions," *Applied Physics B*, vol. 93, no. 2-3, p. 269, 2008.

4.5 M. Sparks, "Optical distortion by heated windows in high-power laser systems," *Journal of Applied Physics*, vol. 42, no. 12, pp. 5029–5046, 1971.

4.6 P. Hello and J.-Y. Vinet, "Analytical models of thermal aberrations in massive mirrors heated by high power laser beams," *Journal de Physique*, vol. 51, no. 12, pp. 1267–1282, 1990.

4.7 J. Peñano, P. Sprangle, A. Ting, R. Fischer, B. Hafizi, and P. Serafim, "Optical quality of high-power laser beams in lenses," *Journal of the Optical Society of America B*, vol. 26, no. 3, pp. 503–510, 2009.

4.8 J. D. Mansell, J. Hennawi, E. K. Gustafson, M. M. Fejer, R. L. Byer, D. Clubley, S. Yoshida, and D. H. Reitze, "Evaluating the effect of transmissive optic thermal lensing on laser beam quality with a Shack-Hartmann wave-front sensor," *Applied Optics*, vol. 40, no. 3, pp. 366–374, 2001.

4.9 C. Pfistner, R. Weber, H. Weber, S. Merazzi, and R. Gruber, "Thermal beam distortions in end-pumped Nd:YAG, Nd:GSGG, and Nd:YLF rods," *IEEE Journal of Quantum Electronics*, vol. 30, no. 7, pp. 1605–1615, 1994.

4.10 Y.-F. Chen, C. Kao, T. Huang, C. Wang, and S. Wang, "Influence of thermal effect on output power optimization in fiber-coupled laser-diode end-pumped lasers," *IEEE Journal of Selected Topics in Quantum Electronics*, vol. 3, no. 1, pp. 29–34, 1997.

4.11 M. Schmid, T. Graf, and H. Weber, "Analytical model of the temperature distribution and the thermally induced birefringence in laser rods with cylindrically symmetric heating," *Journal of the Optical Society of America B*, vol. 17, no. 8, pp. 1398–1404, 2000.

4.12 W. Clarkson, "Thermal effects and their mitigation in end-pumped solid-state lasers," *Journal of Physics D: Applied Physics*, vol. 34, no. 16, p. 2381, 2001.

4.13 U. O. Farrukh, A. M. Buoncristiani, and C. E. Byvik, "An analysis of the temperature distribution in finite solid-state laser rods," *IEEE Journal of Quantum Electronics*, vol. 24, no. 11, pp. 2253–2263, 1988.

4.14 A. Forbes and L. R. Botha, "Physical optics modeling of intracavity thermal distortions in solid state laser resonators," in *Novel Optical Systems Design and Optimization V*, vol. 4768. International Society for Optics and Photonics, 2002, pp. 153–163.

4.15 D. Burnham, "Simple measurement of thermal lensing effects in laser rods," *Applied Optics*, vol. 9, no. 7, pp. 1727–1728, 1970.

4.16 J. Murray, "Pulsed gain and thermal lensing of Nd:LiYF4," *IEEE Journal of Quantum Electronics*, vol. 19, no. 4, pp. 488–491, 1983.

4.17 B. Neuenschwander, R. Weber, and H. P. Weber, "Determination of the thermal lens in solid-state lasers with stable cavities," *IEEE Journal of Quantum Electronics*, vol. 31, no. 6, pp. 1082–1087, 1995.

4.18 P. Hardman, W. Clarkson, G. Friel, M. Pollnau, and D. Hanna, "Energy-transfer up-conversion and thermal lensing in high-power end-pumped Nd:YLF laser crystals," *IEEE Journal of Quantum Electronics*, vol. 35, no. 4, pp. 647–655, 1999.

4.19 M. MacDonald, T. Graf, J. Balmer, and H. Weber, "Reducing thermal lensing in diode-pumped laser rods," *Optics Communications*, vol. 178, no. 4-6, pp. 383–393, 2000.

4.20 J. Blows, P. Dekker, P. Wang, J. Dawes, and T. Omatsu, "Thermal lensing measurements and thermal conductivity of Yb:YAB," *Applied Physics B*, vol. 76, no. 3, pp. 289–292, 2003.

4.21 J. Bourderionnet, A. Brignon, J.-P. Huignard, and R. Frey, "Influence of aberrations on fundamental mode of high power rod solid-state lasers," *Optics Communications*, vol. 204, no. 1-6, pp. 299–310, 2002.

4.22 S. Chénais, F. Druon, S. Forget, F. Balembois, and P. Georges, "On thermal effects in solid-state lasers: The case of ytterbium-doped materials," *Progress in Quantum Electronics*, vol. 30, no. 4, pp. 89–153, 2006.

4.23 H. Rubinsztein-Dunlop, A. Forbes, M. V. Berry, M. R. Dennis, D. L. Andrews, M. Mansuripur, C. Denz, C. Alpmann, P. Banzer, T. Bauer, E. Karimi, L. Marrucci, M. Padgett, M. Ritsch-Marte, N. M. Litchinitser, N. P. Bigelow, C. Rosales-Guzmán, A. Belmonte, J. P. Torres, T. W. Neely, M. Baker, R. Gordon, A. B. Stilgoe, J. Romero, A. G. White, R. Fickler, A. E. Willner, G. Xie, B. McMorran, and A. M. Weiner, "Roadmap on structured light," *Journal of Optics*, vol. 19, no. 1, p. 013001, 2017. [Online]. Available: http://stacks.iop.org/2040-8986/19/i=1/a=013001

4.24 G. Goubau and F. Schwering, "On the guided propagation of electromagnetic wave beams," *IRE Transactions on Antennas and Propagation*, vol. 9, no. 3, pp. 248–256, 1961.

4.25 O. Svelto and D. C. Hanna, *Principles of lasers*. Springer, 2010, vol. 1.

4.26 E. Bernhardi, A. Forbes, C. Bollig, and M. D. Esser, "Estimation of thermal fracture limits in quasi-continuous-wave end-pumped lasers through a time-dependent analytical model," *Optics Express*, vol. 16, no. 15, pp. 11 115–11 123, 2008.

4.27 R. J. Noll, "Zernike polynomials and atmospheric turbulence," *Journal of the Optical Society of America*, vol. 66, no. 3, pp. 207–211, 1976.

4.28 S. Timoshenko and J. Goodier, *Theory of Elasticity 3rd edition*. McGrow—Hill, 1967.

4.29 B. A. Boley and J. H. Weiner, *Theory of thermal stresses*. Courier Corporation, 2012.

4.30 D. Wright, "Beamwidths of a diffracted laser using four proposed methods," *Optical and Quantum Electronics*, vol. 24, no. 9, pp. S1129–S1135, 1992.

4.31 D. Wright, P. Greve, J. Fleischer, and L. Austin, *Optical and Quantum Electronics*, vol. 24, no. 9, pp. S993–S1000, 1992.

4.32 A. Siegman, "Standard of the measurement of beam widths, beam divergence and propagation factors," *Proposal for a working draft ISO TC 172 SC9/WG1)*, 1990.

4.33 T. Dietrich, M. Rumpel, T. Graf, and M. A. Ahmed, "Investigations on ring-shaped pumping distributions for the generation of beams with radial polarization in an Yb:YAG thin-disk laser," *Optics Express*, vol. 23, no. 20, pp. 26 651–26 659, 2015.

4.34 D. Lin and W. Clarkson, "Reduced thermal lensing in an end-pumped Nd:YVO_4 laser using a ring-shaped pump beam," in *CLEO: Science and Innovations*. Optical Society of America, 2016, pp. SM3M–5.

4.35 D. Kim, S. Noh, S. Ahn, and J. Kim, "Influence of a ring-shaped pump beam on temperature distribution and thermal lensing in end-pumped solid state lasers," *Optics Express*, vol. 25, no. 13, pp. 14 668–14 675, 2017.

4.36 Z. Fang, K. Xia, Y. Yao, and J. Li, "Radially polarized and passively Q-switched Nd:YAG laser under annular-shaped pumping," *IEEE Journal of Selected Topics in Quantum Electronics*, vol. 21, no. 1, pp. 337–342, 2014.

4.37 ——, "Radially polarized LG_{01}-mode Nd:YAG laser with annular pumping," *Applied Physics B*, vol. 117, no. 1, pp. 219–224, 2014.

Chapter 5

Conclusion

This work aimed to demonstrate that the theoretical and experimental tools of structured light can be used to increase laser brightness. This objective was explored in three topics.

First, the relationship between the structure of a beam, its M^2 and its brightness was examined. By making use of lossless phase-only reshaping implemented with LCoS SLMs, a general method for converting one mode of structured light to another was presented. Experimental results which showed the conversion of a Gaussian beam to a non-propagation invariant beam were presented, showing the efficacy of the technique. The technique was then reversed, converting a structured beam back into a Gaussian beam. The experimental results from this reverse process confirmed that a beam with a high initial M_0^2 could be losslessly converted back to a Gaussian ($M^2 = 1$), resulting in a brightness enhancement of $\eta = \left(M_0^2\right)^2$. For the cases investigated, the enhancement was about 30 fold.

Second, the relationship between structured light, deleterious thermal effects and brightness was considered. The temperature profile of a radially-symmetric optic was characterised using the Eigen-function expansion solution which was then used to derive expressions for the thermally-induced phase aberrations and thermally-induced stress. The effect of the thermal phase aberrations on HG and LG probe beams was examined. It was shown that an annularly-structured heat source resulted in a reduction in both the thermal phase aberrations and thermal stress. In the context of solid state lasers where the heat source is the pump beam, the reduction in thermal stress allows more energy to be added to the lasing system. Crucially, by implementing the findings described above, that lossless transformations allow brightness enhancement (Chp. 3), the increase in energy can be exploited to increase the power density without reducing the beam quality factor,

yielding a four order of magnitude enhancement in brightness.

Third, by making use of a DMD, a fully configurable low power experimental simulator for high-energy laser sources was demonstrated. To ensure the proper implementation of the DMD its diffractive optical properties were examined (Chp. 2) and characterised. The ambiguity around whether a DMD is a blazed grating or not was resolved. The DMD was more accurately recharacterised as a modified binary amplitude grating. This examination showed that the diffractive efficiency could be enhanced by 20% by using an incident angle of $\pi/15$ rad . Additionally, a number of techniques were demonstrated to ensure the generation of beams with the desired amplitude and phase profiles. These findings were implemented in Chp. 4 to experimentally demonstrate the relationship between structured light and thermal phase aberrations. This result confirms that the experimental tools of structured light can be used to explore laser brightness and significantly simplify the development of high brightness sources.

Thus, it is concluded that structured light can be used to enhance laser brightness directly, as well as accelerate the development of high brightness lasers.

Experimental verification of the work presented here based on the construction of an annularly pumped, losslessly-reshaped laser operating at high powers, is intended for future work. Further, the work presented here could be extended to several different topics. For instance, it has been shown experimentally that two phase only elements of the type described in Chp. 3 can be used within a laser cavity to manipulate the transverse structure of the lasing modes. This allows the mode to have different spatial profiles at different ends of the lasing cavity. Hence, a lasing system could operate with an annular mode at the gain end of the cavity to exploit the advantages of annular pumping while still producing a Gaussian output. Additionally, it is known that laser systems which produce vector beams suffer thermally-induced polarisation aberrations where the temperature gradients within the optical media create inhomogeneous birefringence. By extending the analysis presented in Chp. 4 it may be possible to structure a beam or pump in such a way that it reduces these birefringent aberrations furthering the development of high energy vector beams directly from laser sources.